NUMERICAL MODELLING OF CONVECTIVE INSTABILITY IN A STRATIFIED SHEAR LAYER AND WAVE-LIKE PROPERTIES OF SOLAR SUPERGRANULATION

A DISSERTATION
SUBMITTED TO THE PROGRAM IN SCIENTIFIC COMPUTING AND
COMPUTATIONAL MATHEMATICS
AND THE COMMITTEE ON GRADUATE STUDIES
OF STANFORD UNIVERSITY
IN PARTIAL FULFILLMENT OF THE REQUIREMENTS
FOR THE DEGREE OF
DOCTOR OF PHILOSOPHY

Cristina Green
June 2008

I certify that I have read this dissertation and that, in my opinion, it is fully adequate in scope and quality as a dissertation for the degree of Doctor of Philosophy.

(Alexander Kosovichev) Principal Co-Advisor

I certify that I have read this dissertation and that, in my opinion, it is fully adequate in scope and quality as a dissertation for the degree of Doctor of Philosophy.

(Michael Saunders) Principal Co-Advisor

I certify that I have read this dissertation and that, in my opinion, it is fully adequate in scope and quality as a dissertation for the degree of Doctor of Philosophy.

(Peter Sturrock)

Approved for the University Committee on Graduate Studies.

Abstract

Gizon, Duvall and Schou (2003) have observed that solar supergranulation demonstrates wave-like behaviour, with a non-advective phase speed of ~ 65 m/s. Using numerical models, we tested the proposed explanation that supergranular waves are caused by the steep shear gradient at the solar surface.

A linearized nonviscous compressible hydrodynamic model produces supergranular waves; however, they have slower phase speeds than the observed 65 m/s. Further linear models including viscosity and/or toroidal magnetic fields produce modes at the observed phase speed, for an appropriate choice of parameters. Switching to a nonlinear model increases the phase speed, for the same choice of parameters.

The alternative proposed explanation that the supergranular waves are caused by the Coriolis force is evaluated, using both a linear model and data from nonlinear modelling by Miesch *et al.*, but no evidence of wave-like behaviour was found.

Acknowledgements

I would like to thank my two advisors, Sasha Kosovichev and Michael Saunders. Sasha introduced me to the fascinating field of solar physics and was an invaluable source of advice and encouragement. Michael stepped in at the last minute after my original co-advisor unexpectedly passed away and did an amazing amount of work on very short notice. And I would like to thank the members of my committee, Peter Sturrock, Jon Claerbout and Biondo Biondi, for their time and suggestions. Also, thanks to Mark Miesch and Axel Brandenburg who provided data and advice for the rotation and nonlinear models respectively.

Finally, I would like to dedicate this work to my original co-advisor, Gene Golub, who sadly did not get to see it completed.

Contents

List of Tables

List of Figures

Chapter 1

Background and Motivation

In the outer $\sim 200,000$ km of the Sun, energy from the radiative core is transported to the surface through convection. This convective zone has a variety of interesting dynamics that have yet to be completely explained. Cellular structures of many scales can be seen on the solar surface, ranging from granulation (~ 1000 km) to giant cells ($\sim 10^8$ km). This work focuses on supergranulation, consisting of cells with diameters on the order of 10,000 km.

Supergranulation was first observed by Leighton *et al.* (1962) in photographic Doppler spectroheliograms. They found a uniformly distributed cellular pattern with typical cell diameters of 1.6×10^4 km and mean spacings of $\sim 3 \times 10^4$ km between cell centres. They have lifetimes on the order of one day. Figure 1.1 shows a dopplergram of supergranulation.

While it may appear that there is no supergranulation near the centre of the solar disc, this is not the case. Rather, supergranulation consist of a predominantly horizontal flow, while the Doppler effect can only measure the component of velocities moving toward and away from the observer. Supergranulation can still be investigated in this region, by using the smaller-scale granules as tracers and applying local correlation tracking to determine the larger-scale supergranular flows. The measured horizontal velocity is usually in the range 300–500 m/s, flowing outward from the centre of the cells. Shine *et al.* (2000) found a maximum velocity of ~ 1 km/s.

As suggested by the Dopplergrams, the vertical velocity is much smaller. Küveler (1983) used a photoelectric measurement to determine central upflows of ~ 50 m/s and downflows of ~ 100 m/s at the boundaries. The downflows occur in unconnected areas distributed along the cell boundaries. This difference from granulation, which demonstrates the behaviour of typical convective cells, is not entirely understood. The downdrafts often occur at the vertices of several supergranules, and they may arise from structure deeper in the convection zone. The downdrafts also concentrate magnetic flux, leading the supergranules to be outlined with areas of increased magnetic field.

Gizon, Duvall and Schou (2003) studied supergranulation using a 60-day sequence of Doppler velocity images. The main component of solar rotation was removed, and then

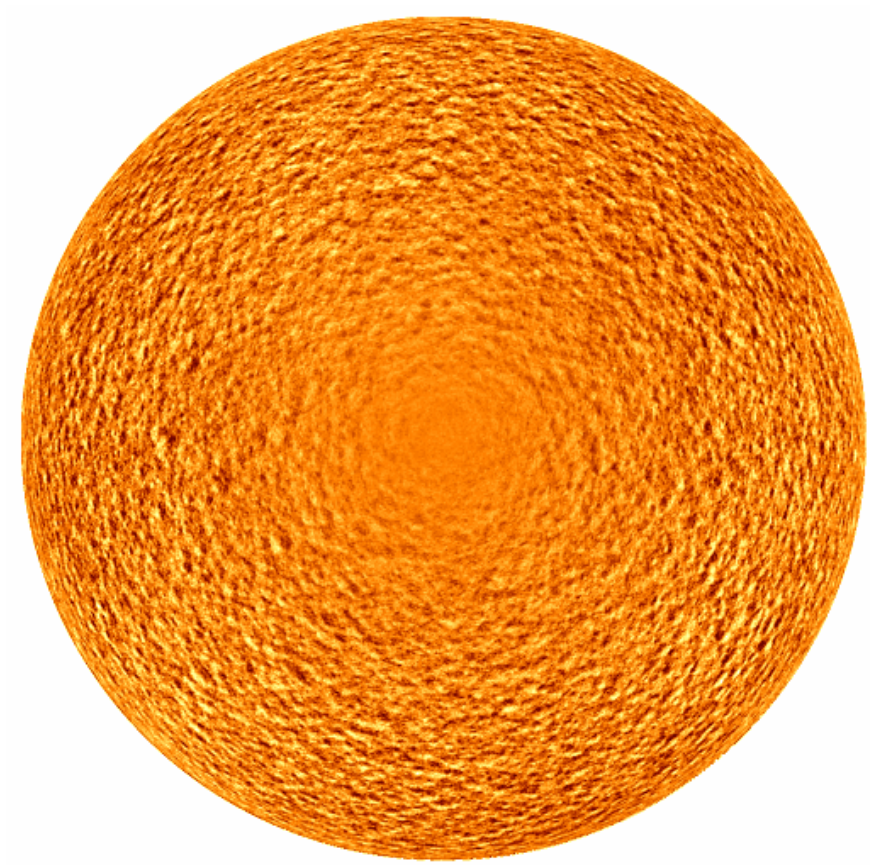

Figure 1.1: MDI 30-Minute Averaged Dopplergram showing supergranulation pattern.

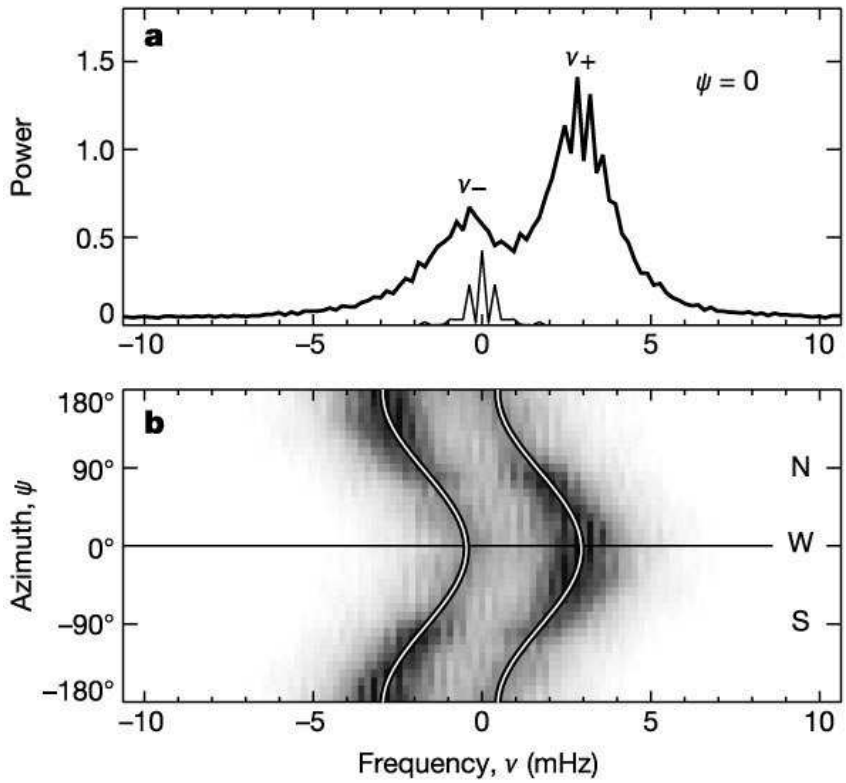

Figure 1.2: Power spectrum at a constant wavenumber $kR = 120$, where R is the solar radius, from Gizon *et al.* (2003).

time-distance helioseismology was applied to determine maps of the horizontal divergence of the flows. Supergranules appear as cellular patterns of horizontal outflows in these maps.

Applying a Fourier-transform to the divergence signal, they obtained power spectra as a function of frequency ν and horizontal wavevector $\mathbf{k} = (k_x, k_y)$, where k_x and k_y are in the east-west and south-north directions respectively. $\mathbf{k}$ can also be expressed in cylindrical coordinates, specified by a magnitude k and a direction ψ. A constant magnitude k, typical of supergranulation, is chosen. Then, for each azimuth ψ, there are two broad peaks in the power spectrum, at frequencies ν_- and ν_+. The power spectrum is shown in Figure 1.2. Because there is no Galilean transformation that causes the peaks to coalesce, this implies that supergranulation undergoes oscillations.

Gizon, Duvall and Schou find that, once the background flow has been removed, each spatial component oscillates at a characteristic frequency ν_0. The relationship between ν_0 and the wavenumber k is shown in Figure 1.3. This relationship does not depend on azimuth or latitude, and thus, the data is consistent with travelling waves having a dispersion relation of $\nu = \nu_0(k)$. The non-advective phase speed of these waves is $u_w = 2\pi\nu_0/k \approx 65$ m/s.

We aim to explain the cause of these supergranular waves. By means of numerical modelling, we test the hypothesis that the wave-like behaviour is caused by the steep shear

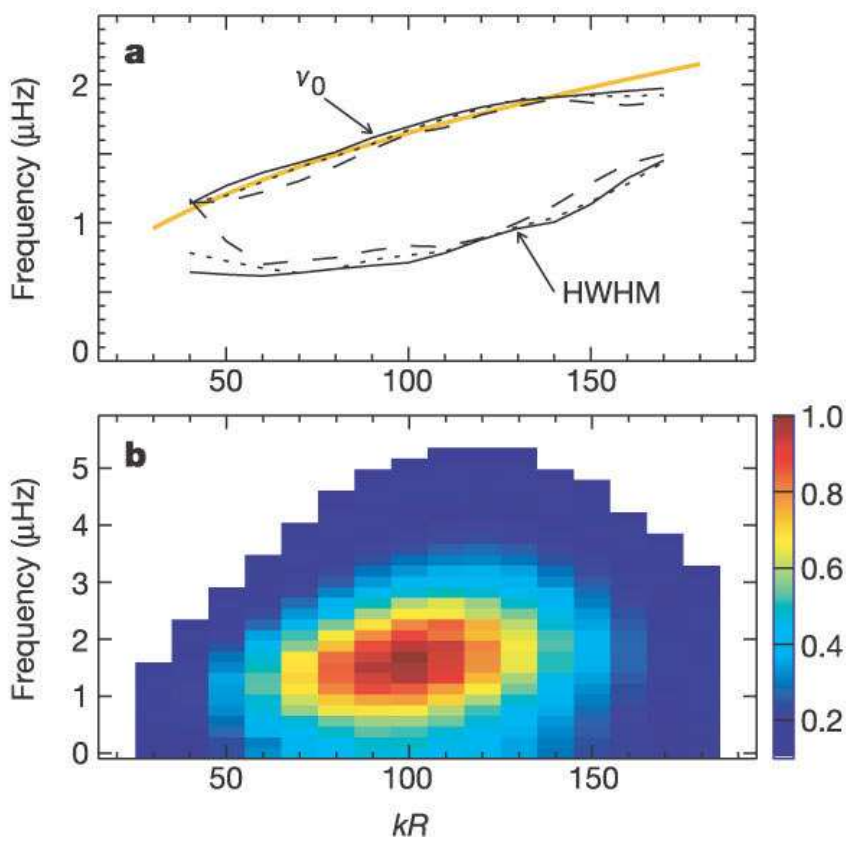

Figure 1.3: Average dynamical properties in a co-moving frame, from Gizon *et al.* (2003). **a** shows the oscillation frequency ν_0 versus kR at latitudes $\lambda = 0°$ (solid), $\lambda = \pm 25°$ (dotted) and $\lambda = \pm 50°$ (dashed). **b** shows the power spectrum corrected for rotation and meridional circulation and averaged over azimuth and latitude.

gradient at the surface of the Sun. This gradient causes unstable convective modes to become running waves: we suggest that it is these convective modes that we observe as supergranulation.

Chapter 2

Linear Model

2.1 Introduction

Completely modelling solar convection is very complicated. Luckily, we are trying to answer a specific question, not doing a simulation. Because of this, we start with the simplest applicable model, using linearized nonviscous compressible hydrodynamics. We treat our computational region as a rectangular slab, and neglect the effects of rotation. To this simple model we add only one thing: a shear gradient, our suggested explanation for the observed wavelike behaviour. Furthermore, as we wish to reproduce an observed wave, we assume a waveform for the solution to our model. This both simplifies our model and simplifies the analysis of the results.

2.2 Model

The linearized model we use was derived by Adam (1977). It describes convection, in the presence of a vertical shear, for the situation in which a convectively unstable layer is bounded above and below by regions of convective stability. This physical situation is shown in Figure 2.1. Adam considers an idealized physical situation, ignoring thermal diffusivity and viscosity and imposing a negative entropy gradient, as well as requiring the unstable layer to be bounded by stable layers. This assumptions are reasonable on the scale of supergranulation.

The model is described by coupled, first-order differential equations from the linearized equations of continuity, motion and adiabatic compressiblity, which are

$$\frac{d\rho_0}{dt} + \rho_0 \nabla \cdot \mathbf{u} + u_{1z}\frac{d\rho_0}{dz} = 0, \tag{2.1}$$

$$\rho_0 \frac{du_{1x}}{dt} + \rho_0 u_{1z}\frac{dU_0}{dz} = -\frac{\partial p_1}{\partial x}, \tag{2.2}$$

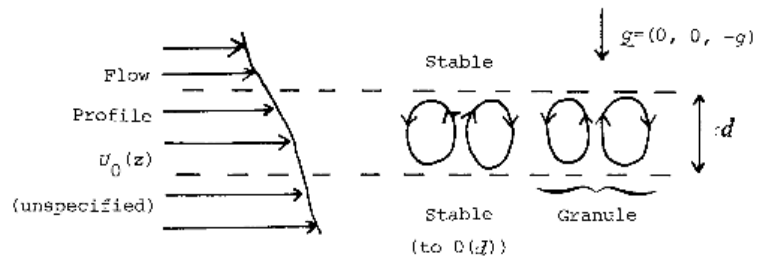

Figure 2.1: Physical situation, from Adam (1977).

$$\rho_0 \frac{du_{1y}}{dt} = -\frac{\partial p_1}{\partial y}, \tag{2.3}$$

$$\rho_0 \frac{du_{1z}}{dt} = -\frac{\partial p_1}{\partial z} - \rho_1 g, \tag{2.4}$$

$$\frac{dp_1}{dt} + u_{1z}\frac{dp_0}{dz} = c_0^2 \left(\frac{d\rho_1}{dt} + u_{1z}\frac{d\rho_0}{dz} \right), \tag{2.5}$$

$$\frac{d}{dt} \equiv \frac{\partial}{\partial t} + U_0 \frac{\partial}{\partial x}. \tag{2.6}$$

The relation between the Eulerian velocity perturbation $\mathbf{u_1}$ and the Lagrangian displacement $\mathbf{q_1}$ yields

$$\left[\frac{\partial}{\partial z} - \left(\frac{d}{dt} \right)^{-1} \frac{dU_0}{dz} \frac{\partial}{\partial x} \right] u_{1z} = \frac{d}{dt} \left(\frac{\partial q_{1z}}{\partial z} \right).$$

Using these, along with the equation of hydrostatic equilibrium

$$\frac{dp_0}{dz} = -\rho_0 g,$$

we can eliminate ρ_1, u_{1x}, u_{1y}, u_{1z}, q_{1x}, q_{1y} and obtain the following equations in p_1 and q_{1z}:

$$\left(\frac{\partial}{\partial z} + \frac{g}{c_0^2} \right) p_1 + \rho_0 \left(\frac{d^2}{dt^2} + n_0^2 \right) q_{1z} = 0, \tag{2.7}$$

$$\frac{d^2}{dt^2} \left(\frac{\partial}{\partial z} - \frac{g}{c_0^2} \right) q_{1z} - \rho_0^{-1} \left(\frac{\partial^2}{\partial x^2} + \frac{\partial^2}{\partial y^2} - \frac{1}{c_0^2} \frac{d^2}{dt^2} \right) p_1 = 0, \tag{2.8}$$

where

$$\frac{d}{dt} = \frac{\partial}{\partial t} + U_0(z) \frac{\partial}{\partial x}$$

and

$$n_0^2 = -\frac{g^2}{c_0^2} - \frac{g}{\rho_0} \frac{d\rho_0}{dz}.$$

The system has a horizontal flow velocity of $(U_0(z), 0, 0)$, pressure perturbation p_1 and vertical displacement of a fluid particle q_{1z}. The basic density, local sound speed and gravitational acceleration are ρ_0, c_0 and g respectively.

Adam performed a mathematical analysis of these equations and formulated general stability criteria for small disturbances in shear flow. He showed that the phase speed of the travelling modes of convection is between the maximum and minimum velocities of the shear flow. In the solar case, according to the helioseismology data this corresponds to a speed of between 0 and 65 m/s. However, Adam's theory does not provide the actual values. We model this effect numerically to determine its characteristics for the shear parameters inferred by helioseismology.

2.3 Numerical Method

Let $p_1(x,y,z,t) = p(z)e^{\imath(kx-\omega t)}$ and $q_{1z}(x,y,z,t) = q(z)e^{\imath(kx-\omega t)}$, assuming waves travel in the x-direction. Then, $\frac{d^2}{dt^2}p_1 = (-\omega^2 + 2U_0(z)k\omega - U_0(z)^2k^2)p(z)e^{\imath(kx-\omega t)}$, and similarly for $\frac{d^2}{dt^2}q_1$. The system of PDEs reduces to

$$\left(\frac{d}{dz} + \frac{g}{c_0^2}\right)p + \rho_0\left(-\omega^2 + 2U_0k\omega - U_0^2k^2 + n_0^2\right)q = 0, \tag{2.9}$$

$$\left(-\omega^2 + 2U_0k\omega - U_0^2k^2\right)\left(\frac{d}{dz} - \frac{g}{c_0^2}\right)q$$
$$-\rho_0^{-1}\left(-k^2 + \frac{1}{c_0^2}\left(\omega^2 - 2U_0k\omega + U_0^2k^2\right)\right)p = 0. \tag{2.10}$$

The parameters ρ_0, c_0, g, and U_0 may depend on depth, and thus are functions of z. We wish to find eigenfrequencies ω in terms of the wavenumber k. We solve this problem numerically by using a finite-difference method.

We assume that the layer being considered is sufficiently shallow to take $z = r$. We choose a layer $r \in [r_0, R]$ for some base radius r_0. We then set boundary conditions $p(r_0) = 0 = p(R)$.

Choosing $N+1$ gridpoints, we consider values of p at the gridpoints and values of q at the half gridpoints:

$$p_j \approx p(r_j) \quad \text{for} \quad 0 \le j \le N,$$

$$q_{j-\frac{1}{2}} \approx q(r_{j-\frac{1}{2}}) \quad \text{for} \quad 1 \le j \le N.$$

Thus, the boundary conditions become $p_0 = 0 = p_N$, and no boundary conditions are needed for q_j.

We approximate the derivatives with finite differences:

$$p'(z_{j-\frac{1}{2}}) \approx \frac{p_j - p_{j-1}}{r_j - r_{j-1}}, \qquad q'(z_j) \approx \frac{q_{j+\frac{1}{2}} - q_{j-\frac{1}{2}}}{r_{j+\frac{1}{2}} - r_{j-\frac{1}{2}}}.$$

As p is only defined at integer j, and q at half-integers, we approximate values between

these points by averaging the values at the two nearest gridpoints:

$$p(z_{j-\frac{1}{2}}) \approx \frac{p_j + p_{j-1}}{2}, \qquad q(z_j) \approx \frac{q_{j+\frac{1}{2}} + q_{j-\frac{1}{2}}}{2}.$$

We can now write (2.9) and (2.10) in terms of the values at the gridpoints and the above approximations:

$$\begin{aligned} p_j - p_{j-1} + \left.\frac{g}{c_0^2}\right|_{j-\frac{1}{2}} \frac{r_j - r_{j-1}}{2}\left(p_j - p_{j-1}\right) + \\ \left(r_j - r_{j-1}\right)\left[\rho_0\left(-\omega^2 + 2U_0 k\omega - U_0^2 k^2 + n_0^2\right)\right]\Big|_{j-\frac{1}{2}} q_{j-\frac{1}{2}} = 0, \end{aligned} \tag{2.11}$$

$$\begin{aligned} \left(-\omega^2 + 2U_0 k\omega - U_0^2 k^2\right)\Big|_j \left[q_{j+\frac{1}{2}} - q_{j-\frac{1}{2}} - \left.\frac{g}{c_0^2}\right|_j \frac{r_{j+\frac{1}{2}} - r_{j-\frac{1}{2}}}{2}\left(q_{j+\frac{1}{2}} - q_{j-\frac{1}{2}}\right)\right] \\ - \left(r_{j-\frac{1}{2}} - r_{j-\frac{1}{2}}\right)\left[\rho_0^{-1}\left(-k^2 + \frac{1}{c_0^2}\left(\omega^2 - 2U_0 k\omega + U_0^2 k^2\right)\right)\right]\Bigg|_j p_j = 0. \end{aligned} \tag{2.12}$$

Defining vectors of p and q values:

$$\vec{p} = \begin{bmatrix} p_1 \\ p2 \\ \vdots \\ p_{N-1} \end{bmatrix}, \qquad \vec{q} = \begin{bmatrix} q_{\frac{1}{2}} \\ q_{\frac{3}{2}} \\ \vdots \\ q_{N-\frac{1}{2}} \end{bmatrix},$$

we can put the equations in vector form:

$$A\vec{p} + B\vec{q} = 0,$$

$$C\vec{q} + D\vec{p} = 0.$$

Let $\Phi = \begin{bmatrix} \vec{p} \\ \vec{q} \end{bmatrix}$. Then

$$\begin{bmatrix} A & B \\ D & C \end{bmatrix} \vec{\Phi} = 0.$$

We collect powers of ω. $A = A_0$, $B = \omega^2 B_2 + \omega B_1 + B_0$, $C = \omega^2 C_2 + \omega C_1 + C_0$, $D = \omega^2 D_2 + \omega D_1 + D_0$ to obtain the vector equation

$$\omega^2 \begin{bmatrix} 0 & B_2 \\ D_2 & C_2 \end{bmatrix} \vec{\Phi} + \omega \begin{bmatrix} 0 & B_1 \\ D_1 & C_1 \end{bmatrix} \vec{\Phi} + \begin{bmatrix} A_0 & B_0 \\ D_0 & C_0 \end{bmatrix} \vec{\Phi} = 0.$$

This can then be solved with a standard polynomial eigenvalue algorithm.

2.4 Test Cases

In order to verify that the model works correctly, we consider simple test cases in which an analytical solution can be found. Obviously we expect this analytical solution to match the numerical solution.

2.4.1 Constant Coefficients

The simplest case is that in which all the coefficients (ρ_0, c_0, g, U_0) are constant in depth. We begin with the initial linearized hydrodynamic equations (2.1) – (2.6), reducing them to two dimensions and evaluating the time derivatives, to obtain a system in terms of the wavenumber k and frequency ω. As the coefficients are constant, the $\frac{d\rho_0}{dz}$ and $\frac{dU_0}{dz}$ terms are obviously zero. We then obtain the following system:

$$\begin{aligned}
(-\imath\omega + \imath k U_0)\,\rho(z) + \rho_0\left[\imath k u_x(z) + u_z'(z)\right] &= 0,\\
\rho_0\,(-\imath\omega + \imath k U_0)\,u_x(z) &= -\imath k p(z),\\
\rho_0\,(-\imath\omega + \imath k U_0)\,u_z(z) &= -p'(z) - g\rho(z),\\
(-\imath + \imath k U_0)\,p(z) - \rho_0 g u_z(z) &= c_0^2\,(-\imath\omega + \imath k U_0)\,\rho(z).
\end{aligned}$$

Eliminating ρ, u_x and u_z yields a single second-order differential equation in p:

$$p''(z) + \lambda^2(k,\omega)p(z) = 0,$$

where

$$\begin{aligned}
-c0^4\rho_0\,(-\imath\omega + \imath k U_0)^2\,\lambda^2(k,\omega) = \quad & \left(c_0^2\rho_0\,(-\imath\omega + \imath k U_0)^2 - \rho_0 g^2\right)\left((-\imath\omega + \imath k U_0)^2 + c_0^2 k^2\right),\\
& +\rho_0 g^2\,(-\imath\omega + \imath k U_0)^2\,.
\end{aligned}$$

The boundary conditions $p(r_0) = 0 = p(R)$ provide a condition on $\lambda(k,\omega)$, and thus a relationship between ω and k:

$$\lambda(k,\omega) = \frac{n\pi}{R - r_0} \quad \text{for} \quad n = 0, 1, 2, \ldots.$$

Letting $x = (-\imath\omega + \imath k U_0)^2$, this reduces to a quadratic equation,

$$x^2 + c_0^2\left(k^2 + \left(\frac{n\pi}{R - r_0}\right)^2\right)x - g^2k^2 = 0.$$

The quadratic formula and $\omega = \pm\sqrt{-x} + kU_0$ provide us with an analytical solution for ω in terms of k. We choose constant values for ρ_0, c_0 and g, and then the numerical model can be compared to this analytical solution. The numerical model is correct for this case.

2.4.2 Isothermal with Uniform Gravity

The numerical model having been confirmed for the simplest test case, we proceed to the case in which just temperature and gravity are constant, and in which there is no shear flow. In this case, the background state is

$$\begin{aligned} \rho_0 &= \rho_* e^{-\frac{z}{H}}, \\ p_0 &= p_* e^{-\frac{z}{H}}, \\ c_0^2 &= \gamma \frac{p_0}{\rho_0} = \gamma \frac{p_*}{\rho_*}. \end{aligned}$$

The equation of hydrostatic equilibrium

$$\frac{dp_0}{dz} = -g\rho_0$$

provides the scale height

$$H = \frac{p_*}{g\rho_*} = \frac{c_0^2}{\gamma g}$$

and the Brunt-Väisälä frequency

$$n_0^2 = \frac{\gamma - 1}{\gamma} \frac{g}{H}.$$

Using these coefficients, and new scaled variables

$$y_1 = \frac{1}{\sqrt{\rho_* \rho_0}} p_1, \qquad y_2 = \sqrt{\frac{\rho_0}{\rho_*}} q_1.$$

Equations (2.7) and (2.8) can be rewritten as

$$\left[\frac{d}{dz} - \frac{1}{2H} + \frac{g}{c_0^2}\right] y_1 + \left[n_0^2 - \omega^2\right] y_2 = 0, \tag{2.13}$$

$$-\omega^2 \left[\frac{d}{dz} + \frac{1}{2H} - \frac{g}{c_0^2}\right] y_2 + \left[k^2 - \frac{\omega^2}{c_0^2}\right] y_1 = 0. \tag{2.14}$$

Combining this system into a single second-order equation yields

$$y_1''(z) + k_z^2 y_1(z) = 0,$$

where

$$k_z^2 = -\left(\frac{1}{2H} - \frac{g}{c_0^2}\right)^2 - \left(n_0^2 - \omega^2\right)\left(\frac{1}{c_0^2} - \frac{k^2}{\omega^2}\right).$$

The boundary condition, $p(r_0) = 0 = p(R)$ or $y_1(r_0) = 0 = y_1(R)$, provides a condition on k_z:

$$k_z = \frac{n\pi}{R - r_0} \quad \text{for} \quad n = 0, 1, 2, \ldots.$$

This reduces to a quadratic equation in ω^2:

$$\frac{1}{c_0^2}\omega^4 + \left[-\left(\frac{1}{2H} - \frac{g}{c_0^2}\right)^2 - \frac{n_0^2}{c_0^2} - k^2 - \frac{n^2\pi^2}{(R-r_0)^2}\right]\omega^2 + n_0^2 k^2 = 0.$$

The quadratic formula provides us with an analytical solution for ω in terms of k. We choose constant values for g, γ, c_0^2, ρ_* and p_*, and then the numerical model can be compared to this analytical solution. The numerical model is correct for this case.

2.4.3 Polytrope

A polytropic model is a fairly good approximation to the Sun, in which the solar convection zone is approximately adiabatically stratified. Thus, take

$$\frac{d\ln p}{dr} = \Gamma_1 \frac{d\ln\rho}{dr},$$

where Γ_1 is constant. The gravitational acceleration g is assumed to be constant. The sound speed is given by

$$c_0^2 = \frac{g}{\mu_p}(R-r),$$

where $\mu_p = 1/(\Gamma_1 - 1)$ is the effective polytropic index. For this case, the dispersion relation for high-frequency p-modes is

$$\omega^2 = \frac{2}{\mu_p}\frac{g}{R}(n+\alpha)L,$$

where α is some phase constant. The derivation of the dispersion relation can be found in Christensen-Dalsgaard's Lecture Notes on Stellar Oscillations.

The conditions of the model are sufficient to calculate the necessarily coefficients, within a constant factor. If values are chosen for the constants, the numerical model can be compared to the dispersion relation. The phase constant is not known, and thus can be calibrated to match the numerical solution. The numerical model is correct for this case.

2.5 Quantities from Helioseismology

In order to obtain useful results, we want to use coefficients as similar as possible to the actual values in the Sun. Since we are modelling behaviour inside the Sun, where physical quantities can not be measured directly, we use coefficients obtained from helioseismology.

Helioseismology uses measurements of surface oscillations to set up an inverse problem, calculating physical quantities, such as density, inside the Sun. The solution to such inverse problems depends on having appropriate "kernels": weighting functions providing a sensitivity of each mode to a given region of the Sun. Peter Giles's thesis provides a good introduction to this technique.

The parameters used here are computed from observations using the Michelson Droppler Imager (MDI) instrument on board the Solar and Heliospheric Observatory (SOHO) spacecraft, launched on December 2, 1995.

2.5.1 Variable Scaling

The coefficients from helioseismology are in cgs units; thus, some quantities are very large, while others are quite small. This is a problem in our numerical model, as the numerical error for the larger quantities could end up being amplified, or could dominate the actual values for the smaller quantities. Thus, we scale the variables, attempting to get them all to within a few orders of magnitude of each other. For our results to be physically meaningful, the scaling of different variables must be consistent, so we choose a scaling factor for length, time and mass, and this defines the factors for all our quantities.

2.6 Results

We begin by using values obtained by helioseismology for ρ_0, c_0, g and n_0^2, and no shear flow. Without shear flow, the choice of n_0^2 has the greatest impact on the resulting spectrum. The Brunt-Väisälä frequency from helioseismology is shown in Figure 2.2. We choose the upper boundary of our layer low enough to avoid modes becoming "trapped" in the sharp increase of n_0^2 near the surface. Thus, we obtain the spectrum of solar oscillations, shown in Figure 2.3. As well known from the theory of stellar oscillations, it consists of the usual f- and p-modes (surface gravity and acoustic waves), shown by solid curves. These modes are purely oscillatory; their eigenfrequencies are real numbers. We also obtain convective modes, shown by dashed curves. These are purely growing and decaying modes with imaginary eigenfrequencies. The typical range of the wavenumber, kR, for supergranulation is $50-150$.

Adding the shear flow causes the eigenfrequencies and eigenfunctions of the convective modes to become complex. Figure 2.5 shows the real part of the frequencies of the convective modes calculated for the solar velocity profile (shown in Figure 2.4). The imaginary part of the frequencies of the convective modes remains essentially unchanged from the case without shear velocity. The corresponding horizontal phase speed, ω/k, relative to the rotation of the Sun's surface, is shown in Figure 2.6 for the first ten convective modes. The first mode has the lowest phase speed. The phase speeds converge as the mode number increases.

The calculated phase speed does not exceed 26 m/s, which is significantly smaller than the maximum estimated speed of 65 m/s in the shear. Since the actual radial profile of the subsurface shear velocity has not been determined reliably, we calculated a series of models for linear profiles, varying the velocity gradient. The results shown in Figure 2.7 indicate that the phase speed of the running waves of convection increases with the velocity gradient; however, it does increase quickly enough for the unreliability of the shear velocity profile to explain the discrepancy from the observed velocity of the supergranulation pattern.

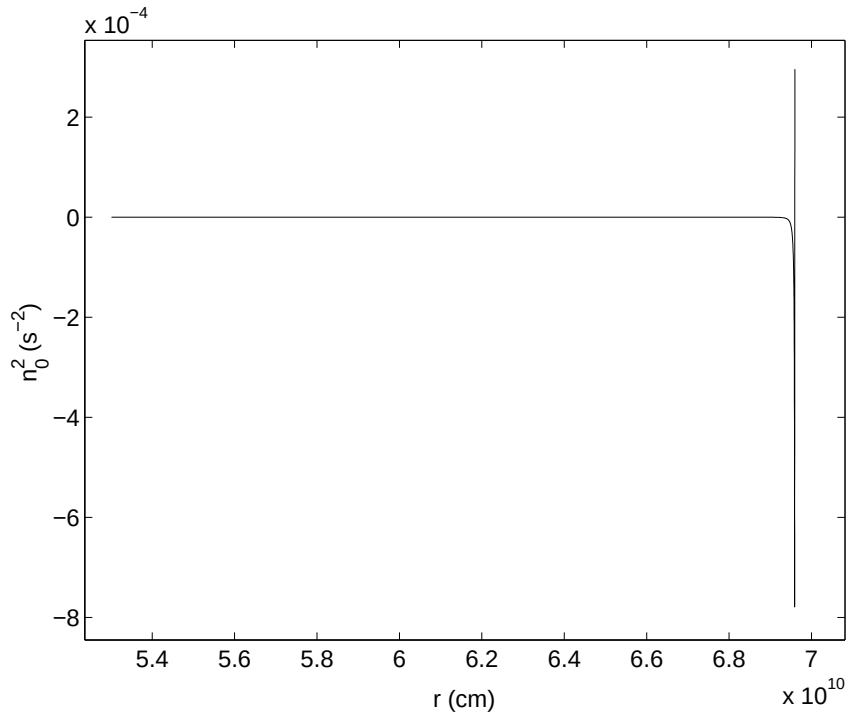

Figure 2.2: Brunt-Väisälä frequency as a function of radius, from helioseismology.

The eigenfunctions associated with the frequencies of the convective modes are shown in Figure 2.8. The oscillations of the pressure perturbation occur at the top of the convective layer, above the depth at which the shear velocity matches the observed phase speed of 65 m/s. The pressure perturbations in the layer for the static case, in Figure 2.9, form vertically aligned cells. In the presence of a shear gradient, these cells deform, as seen in Figure 2.10: this indicates that the phase speeds we have obtained are due to running waves, and not just advection.

The previous results were all calculated using coefficients obtained from helioseismology. We now consider the case in which we continue to use a shear velocity profile from helioseismology, but all other coefficients are from a polytropic model. The most notable difference with the model is in the Brunt-Väisälä frequency, shown in Figure 2.11. In the polytrope, n_0^2 has a much smaller drop near the surface than in the solar model.

The real part of the frequencies of the first three convective modes is shown in Figure 2.12. A polytrope is a better approximation for high k; thus, the crossing of the second and third modes at low k is not a great concern. Figure 2.13 showed the corresponding phase speeds, relative to the rotation of the Sun's surface. These are substantially higher than those obtained with helioseismology data, coming close to the observed speeds. This difference can be explained by considering the corresponding eigenfunctions, in Figure 2.14. In this case, the oscillations extend much deeper into the layer, reaching depths with higher

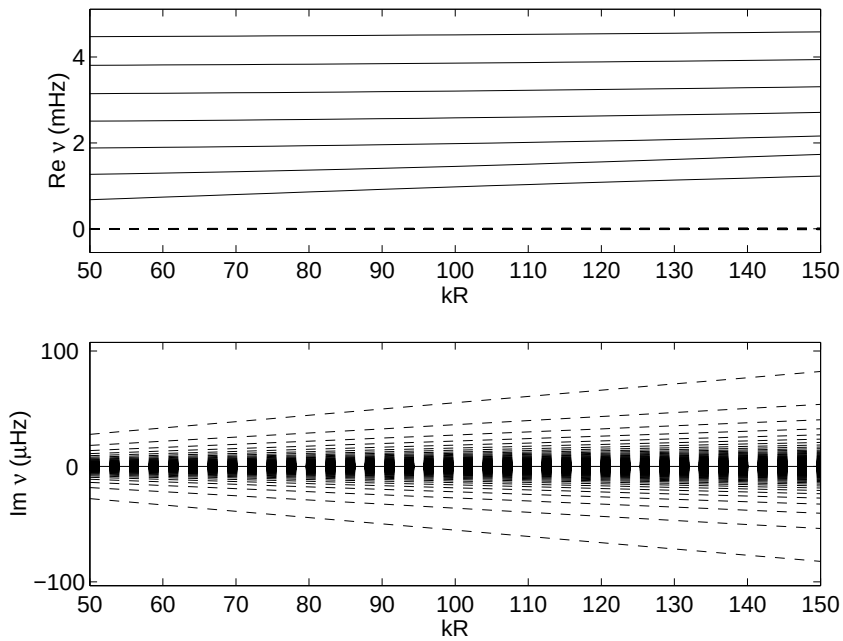

Figure 2.3: Real and imaginary parts of the solar oscillation spectrum calculated without the shear flow, as a function of the horizontal wave number, k. $\nu = \omega/2\pi$ is the cyclic frequency, and R is the solar radius. The spectrum consists of pure oscillatory f- and p-modes (solid curves) and pure exponential convective modes (dashed curves).

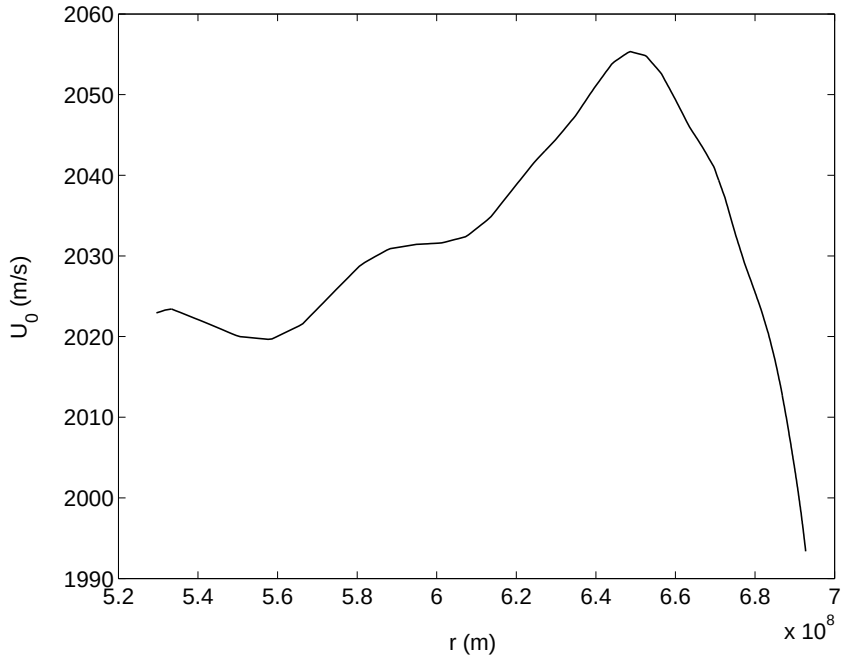

Figure 2.4: The radial velocity as a function of radius in the equatorial region of the subsurface shear layer, obtained from helioseismology.

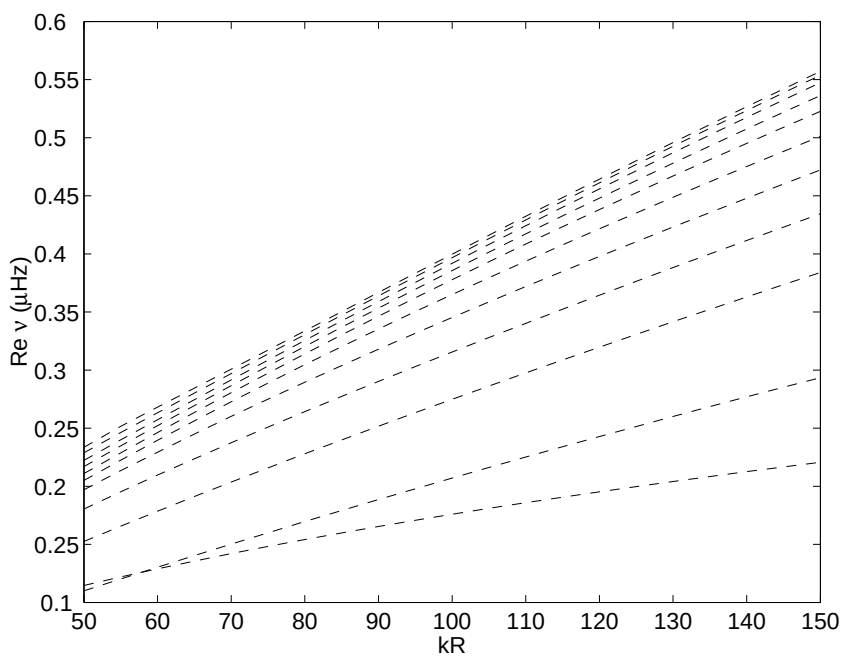

Figure 2.5: The real part of frequencies of the convective modes in the presence of the subsurface shear flow as a function of kR.

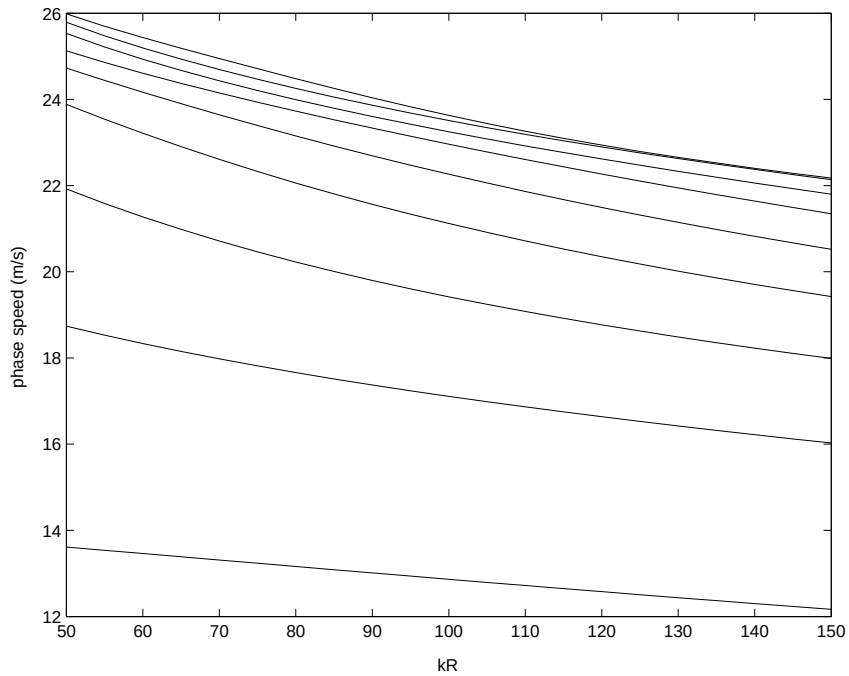

Figure 2.6: The phase speed of the convective modes in the presence of the subsurface shear flow as a function of kR.

shear velocities.

Because of the possibility that the Brunt-Väisälä frequency obtained from helioseismology combined with the limitations of our model may be artificially constraining the convective modes near the surface, we now consider modifications to our model, taking into account the effects of the rotation, viscosity and magnetic field.

2.7 Conclusions

In the presence of a shear gradient, unstable convective modes turn into running waves. Previous analytic analysis by Adam provides bounds on the phase speed of these waves. In order to obtain a more precise approximation of this speed, we implement a linear numerical model.

Linear modelling demonstrates that a shear gradient can change stationary convective modes into running waves. These waves travel faster than the surface velocity, thus qualitively reproducing the observed wavelike behaviour of supergranulation. However, the model phase speed is of the same order, but significantly smaller than the obsevations.

The eigenfunctions associated with these modes show cells near the top of the layer, consistent with supergranulation. As the order of the mode increases, more cells occur in depth, indicating that the mode order corresponds to a vertical wavenumber. These cells are

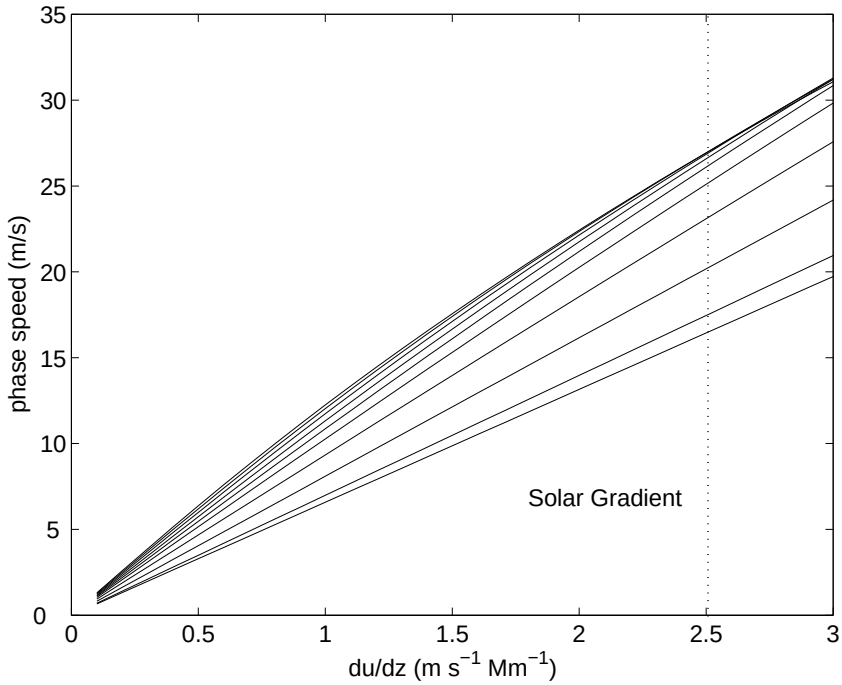

Figure 2.7: The phase speed of the convective modes, for $kR = 50$ as a function of the subsurface velocity gradient. The vertical dotted line indicates the current estimate from helioseismology data.

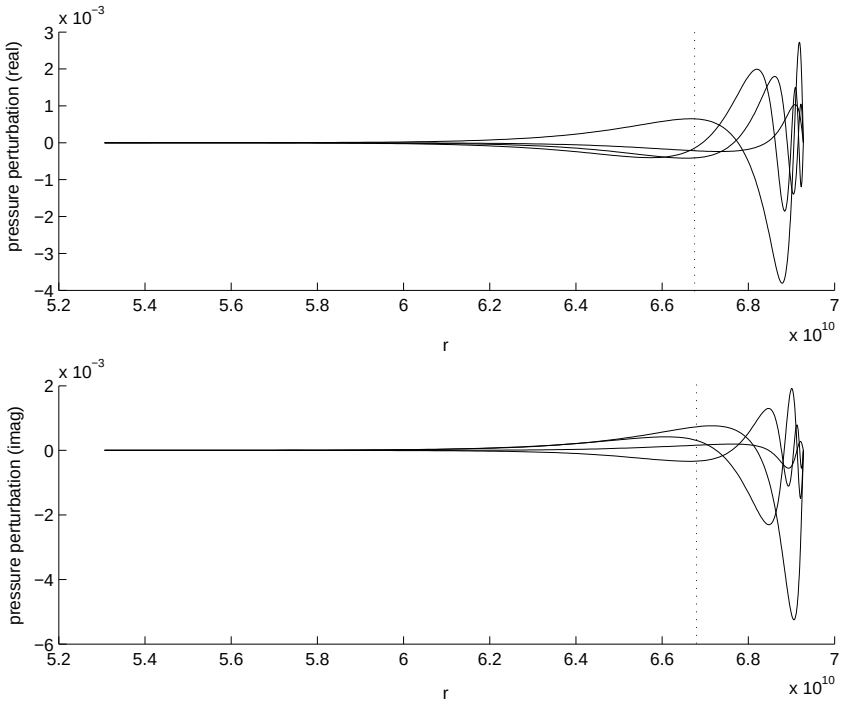

Figure 2.8: Pressure perturbation functions corresponding to the first four convective modes. The vertical dotted line indicates the depth at which U_0 equals the observed velocity of the supergranulation pattern.

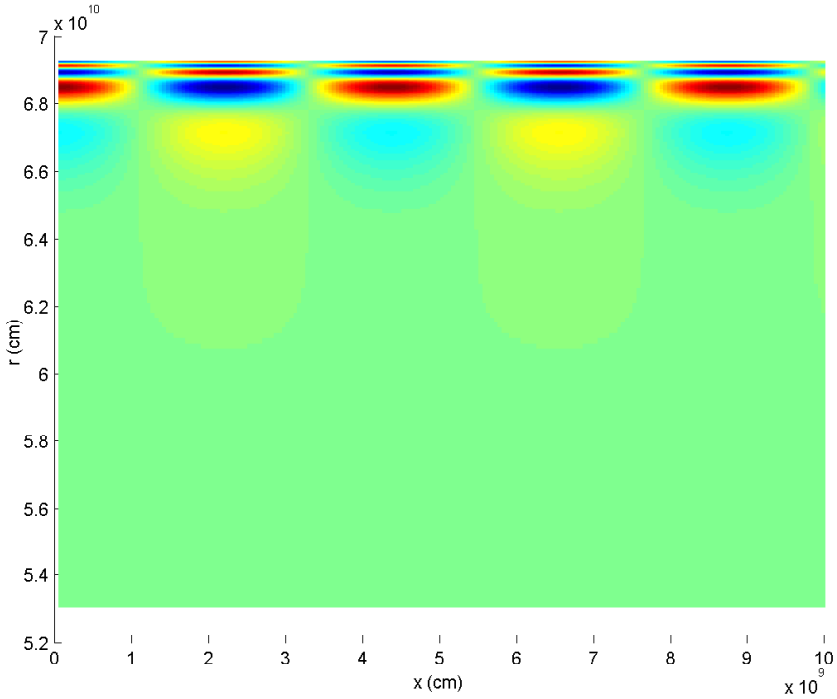

Figure 2.9: Pressure perturbation for the fifth convective mode without shear flow.

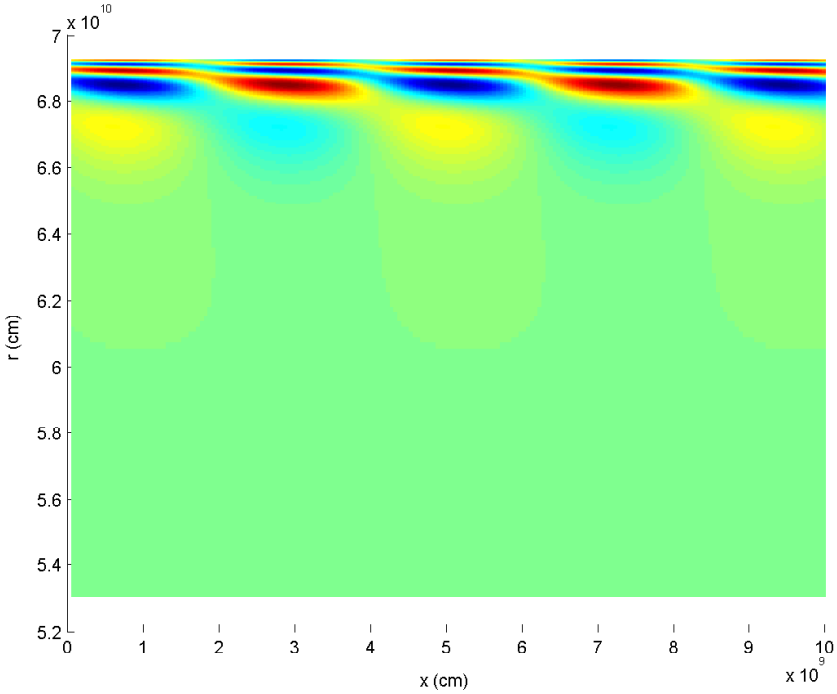

Figure 2.10: Pressure perturbation for the fifth convective mode with shear velocity obtained from helioseismology.

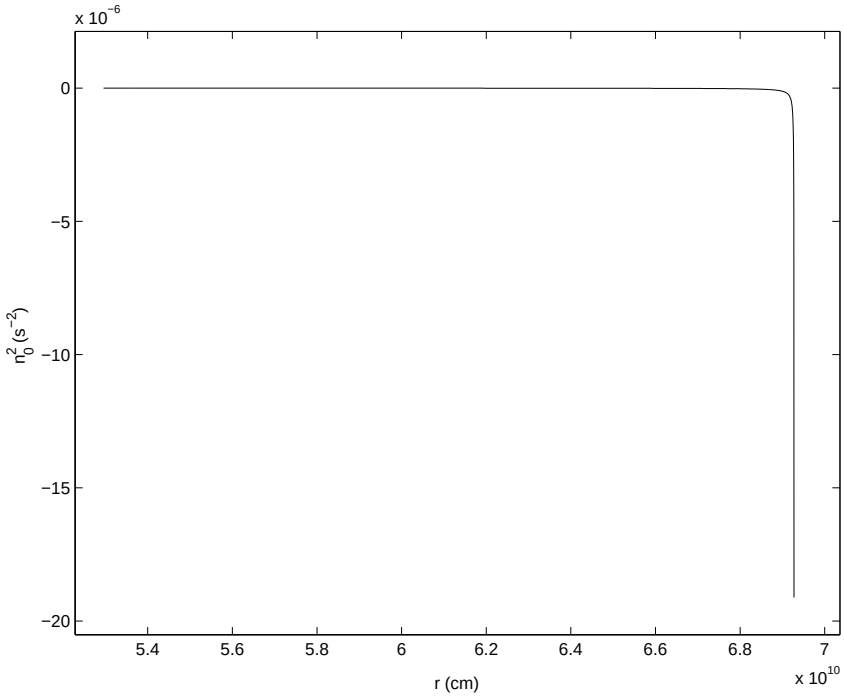

Figure 2.11: Brunt-Väisälä frequency for a polytropic model.

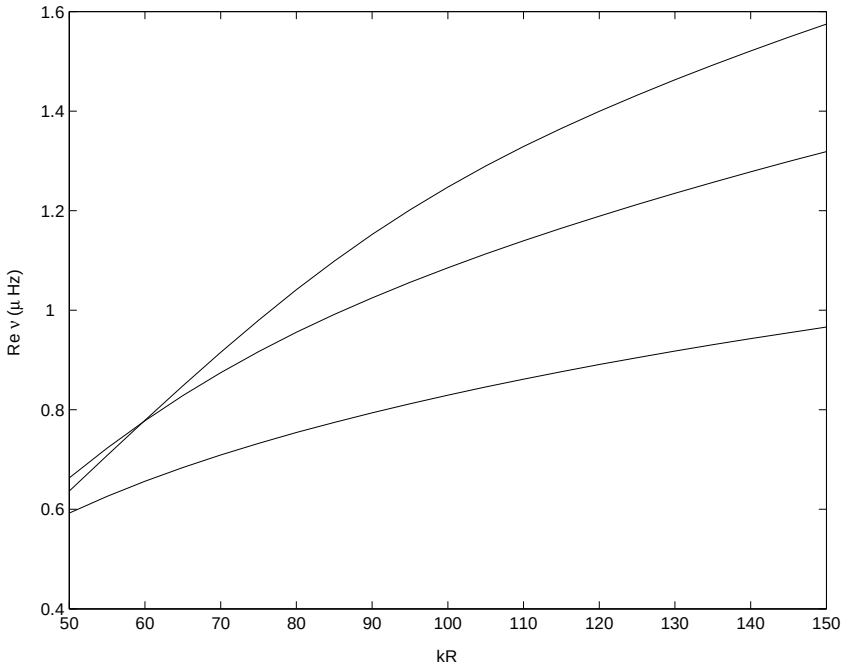

Figure 2.12: The real part of frequencies of the convective modes for a polytropic model in the presence of the subsurface shear flow as a function of kR.

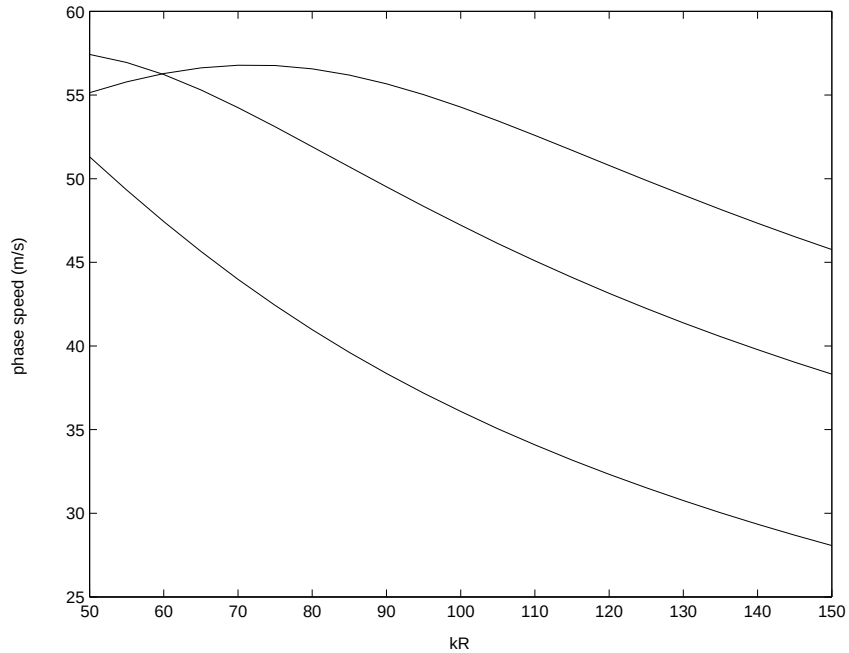

Figure 2.13: The phase speed of the convective modes for a polytropic model in the presence of the subsurface shear flow as a function of kR.

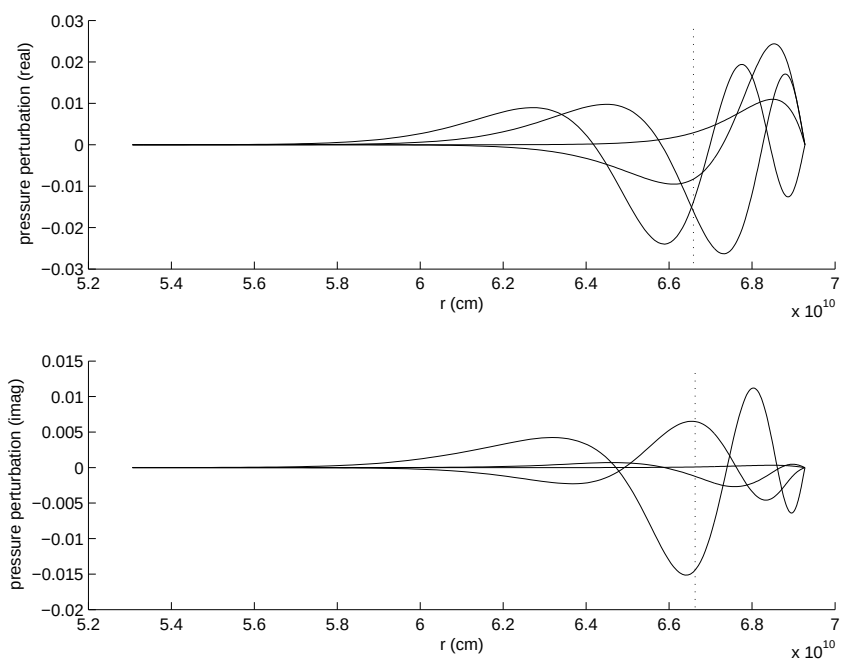

Figure 2.14: Pressure perturbation functions corresponding to the first three convective modes for a polytropic model. The vertical dotted line indicates the depth at which U_0 equals the observed velocity of the supergranulation pattern.

concentrated at the top of the layer. In comparison, the cells obtained using a polytrope in place of the solar model extend much deeper into the layer. The greatest difference between the solar model and the polytrope is in the behaviour of the Brunt-Väisälä frequency at the surface. As we had to choose the upper boundary carefully to avoid obtaining modes on the scale of granulation, it is possible that the Brunt-Väisälä frequency obtained from helioseismology could be constraining the modes near the surface, which would produce lower phase speeds. This behaviour could be an artifact of our model, as the neglected contributions of viscosity and magnetic field may counteract this effect. Futhermore, as a linear model was considered, there may be nonlinear effects contributing to the observed phase speed. These possibilities are considered in the following chapters by means of further modelling.

2.8 Alternative Linear Model

As we wish to consider a number of variations on our model, it would be a lot more efficient to solve directly our original linearized equations of continuity, motion and adiabatic compressibility (2.1) – (2.6). Now, instead of eliminating variables, we consider ρ_1, u_{x1}, u_{z1} and p_1 to have wave behaviour: $\rho_1 = \rho(z)e^{\imath(kx-\omega t)}$, $u_{x1} = u(z)e^{\imath(kx-\omega t)}$, $u_{z1} = v(z)e^{\imath(kx-\omega t)}$, $p_1 = p(z)e^{\imath(kx-\omega t)}$. (We have dropped u_{1y} and (2.3), to reduce to a two-dimensional model.) Thus, our system reduces to

$$(-\imath\omega + \imath kU_0)\,\rho(z) + \rho_0\left[\imath ku(z) + v'(z)\right] + u(z)\frac{d\rho_0}{dz} = 0, \tag{2.15}$$

$$\rho_0\,(-\imath\omega + \imath kU_0)\,u(z) + \rho_0\frac{dU_0}{dz}v(z) = -\imath kp(z), \tag{2.16}$$

$$\rho_0\,(-\imath\omega + \imath kU_0)\,v(z) = -p'(z) - g\rho(z), \tag{2.17}$$

$$(-\imath\omega + \imath kU_0)\,p(z) - \rho_0 g v(z) = c_0^2\left[(-\imath\omega + \imath kU_0)\,\rho(z) + \frac{d\rho_0}{dz}v(z)\right]. \tag{2.18}$$

As with our original model, we find the eigenfrequencies ω in terms of the wavenumber k numerically using a finite-difference scheme on an offset grid. We now use the boundary condition $v(r_0) = 0 = v(R)$. Thus, choosing $N+1$ gridpoints, we consider values of v at the gridpoints and values of ρ, u and p at the half gridpoints:

$$\begin{aligned}
\rho_{j-\frac{1}{2}} &\approx \rho(r_{j-\frac{1}{2}}) && \text{for} \quad 1 \le j \le N,\\
u_{j-\frac{1}{2}} &\approx u(r_{j-\frac{1}{2}}) && \text{for} \quad 1 \le j \le N,\\
v_j &\approx v(r_j) && \text{for} \quad 0 \le j \le N,\\
p_{j-\frac{1}{2}} &\approx p(r_{j-\frac{1}{2}}) && \text{for} \quad 1 \le j \le N.
\end{aligned}$$

The boundary conditions become $v_0 = 0 = v_N$, and no boundary conditions are needed for ρ_j, u_j and p_j. As before, we approximate the derivatives with finite differences, and approximate values between gridpoints using interpolation, and substitute these approximations

into (2.15) – (2.18):

$$
\begin{aligned}
(-\imath\omega + \imath k U_0)\big|_{j-\frac{1}{2}}\,\rho_j &+ \rho_0\big|_{j-\frac{1}{2}}\left[\imath k u_j + \frac{v_j - v_{j-1}}{r_j - r_{j-1}}\right] \\
&+ \frac{v_j + v_{j-1}}{2}\,\frac{d\rho_0}{dz}\bigg|_{j-\frac{1}{2}} = 0, \qquad (2.19)\\
\rho_0\,(-\imath\omega + \imath k U_0)\big|_{j-\frac{1}{2}} &+ \rho_0 \frac{U_0}{dz}\bigg|_{j-\frac{1}{2}} \frac{v_j + v_{j-}}{2} = -\imath k p_j, \qquad (2.20)\\
\rho_0\,(-\imath\omega + \imath k U_0)\big|_j\, v_j &= -\frac{p_{j+1} - p_j}{r_{j+\frac{1}{2}} - r_{j-\frac{1}{2}}} - g\big|_j\,\frac{\rho_j + \rho_{j+1}}{2}, \qquad (2.21)\\
(-\imath\omega + \imath k U_0)\big|_{j-\frac{1}{2}}\,p_j &- \rho_0 g\big|_{j-\frac{1}{2}}\,\frac{v_j + v_{j-1}}{2} \\
&= c_0^2\left[(-\imath\omega + \imath k U_0)\,\rho_j + \frac{d\rho_0}{dz}\frac{v_j + v_{j-1}}{2}\right]\bigg|_{j-\frac{1}{2}}. \qquad (2.22)
\end{aligned}
$$

These equations can be written in vector form, and ω can be found with a standard matrix eigenvalue algorithm. The results of this model are identical to those of the original model, as we expect.

Chapter 3

Chebyshev Collocation

3.1 Introduction

We had initially planned on applying Chebyshev Collocation to our problem. As opposed to the finite differences we ended up using, collocation is based on the idea that an unknown function, $u(z)$ can be approximated by a sum of $N+1$ basis functions $\phi_n(z)$:

$$u(z) \approx u_N(z) = \sum_{n=0}^{N} a_n \phi_n(z).$$

The function $u(z)$ is the solution to some equation $Lu = f(z)$, where L is the operator of the differential equation. Substituting the approximation into this equation defines a residual function:

$$R(z; a_0, a_1, \ldots, a_N) = Lu_N - f.$$

The residual function is zero for the exact solution. Spectral and pseudospectral methods aim to minimize the residual function through different choices of coefficients a_n. Collocation uses the simplest strategy to choose these coefficients: it requires the residual function to be zero on a selected grid of points.

In the case of Chebyshev Collocation, these basis functions are Chebyshev Polynomials $\phi_n(z) = T_n(z)$, where $z = \cos(\theta)$ and then $T_n(z) \equiv \cos(n\theta)$.

For this case, collocation is applied at the Gauss-Lobatto points:

$$z_j = \cos(\frac{j\pi}{N}).$$

These are the extrema of the N-th Chebyshev polynomial. By requiring the residual function to be zero at these points, we are able to bound the truncation error of our solution.

Comparing the order of error of a collocation method to a finite difference method shows why we would choose a collocation method. A finite difference scheme has an error of $O(h^m)$,

where h is the grid spacing and m is the fixed order of the differencing scheme chosen. For a collocation method, increasing the order N causes a decrease in the interval h, similarly to increasing the number of grid points for a finite difference method. However, unlike in finite differences, there is no fixed order m. The interval size h is $O(1/N)$; thus, we have a total error of $O((1/N)^N)$ for a collocation method. This "exponential convergence" easily beats any finite difference scheme, no matter how high the order.

3.2 Boundary Conditions

Unlike using a Fourier series to approximate a solution with periodic boundary conditions, Chebyshev polynomials do not automatically satisfy the appropriate boundary conditions. However, explicit constraints can be added:

$$\sum_{n=0}^{N} a_n \phi_n(1) = \alpha.$$

Inserting this into the algebraic equations produced by our choice of minimization technique for $R(x; a_0, a_1, \ldots, a_N)$, causes $u(1) = \alpha$ to be satisfied by the approximate solution.

For collocation, we require the differential equation to be satisfied at each of the $N+1$ gridpoints. The equations for the boundary points can then be replaced with boundary constraints instead. We still have $N+1$ equations to find the $N+1$ unknown coefficients: the differential equation satisfied at the $N-1$ interior points, and two boundary constraints.

3.3 The Problem

In essence, we have a second-order differential equation with two boundary conditions, which we should be able to solve easier using Chebyshev collocation, as described previously. However, for simplicity, we are instead considering the equivalent first-order system in equations (2.9) and (2.10).

Although analytically equivalent to a second-order differential equation, a first-order system presents a difficulty when we attempt to solve it using Chebyshev collocation. The number of unknown coefficients and equations at interior points have now doubled, but we still have only two boundary conditions: basically, "half" a boundary condition at each boundary. Thus, we now have $2N+2$ unknowns, and only $2N$ equations.

One can imagine several ways of finding the required number of equations. We shall test some different options on the wave equation, which, unlike with our system, we can easily switch between a second-order equation and a first-order system, and, furthermore, can compare our results to the analytical solution.

3.4 Example: Wave Equation

As an example, we consider the differential equation

$$u'' = k^2 u \tag{3.1}$$

with boundary conditions $u(-1) = 0 = u(1)$. This can solved analytically for eigenvalues k:

$$k = \frac{n\pi}{2}.$$

We wish to compare the analytical solution to the results using Chebyshev collocation.

Equation (3.1) can also be written as a first-order system:

$$u' = kv, \tag{3.2}$$

$$v' = ku. \tag{3.3}$$

Or, in vector form,

$$w' = kAw, \tag{3.4}$$

where

$$w = \begin{bmatrix} u \\ v \end{bmatrix} \quad \text{and} \quad A = \begin{bmatrix} 0 & 1 \\ 1 & 0 \end{bmatrix}.$$

3.4.1 Second-Order Equation

Chebyshev collocation can be easily applied to our example in the form of a second-order differential equation. We approximate u with a series of $N+1$ Chebyshev polynomials:

$$u(x) \cong \sum_{n=0}^{N} a_n T_n(x).$$

We then require (3.1) to be satisfied at the Gauss-Lobatto points $x_j = cos(\frac{j\pi}{N})$:

$$\sum_{n=0}^{N} a_n T_n''(x_j) = k^2 \sum_{n=0}^{N} a_n T_n(x_j).$$

This can be we written in matrix form, $Ay = k^2 By$, where y is the vector of coefficients a_n. Each row in matrices A and B corresponds to one of the gridpoints x_j.

To satisfy the boundary conditions, the rows corresponding to x_0 and x_N can be replaced by the boundary conditions $u(\pm 1) = 0$; that is,

$$\sum_{n=0}^{N} a_n T_n(\pm 1) = 0.$$

In matrix form, this is

$$\begin{bmatrix} 0 & \dots & 0 \end{bmatrix} y = k^2 \begin{bmatrix} T_0(\pm 1) & \dots & T_N(\pm 1) \end{bmatrix} y,$$

which can easily be substituted into the appropriate rows of A and B. The resulting matrix eigenvalue problem can be solved with a standard general eigenvalue algorithm. The numerical results match the analytical solution.

3.4.2 First-Order System

As with the second-order equation, we approximate w with a series of $N+1$ Chebyshev polynomials:

$$w(x) \cong \sum_{n=0}^{N} \begin{bmatrix} a_n \\ b_n \end{bmatrix} T_n(x).$$

We now have a vector of coefficients for each element in the series, meaning we now have $2(N+1)$ unknowns, rather than the $N+1$ we had in the previous formulation.

We require (3.4) to be satisfied at the Gauss-Lobatto points $x_j = cos(\frac{j\pi}{N})$:

$$\sum_{n=0}^{N} \mathbf{c_n} T_n'(x_j) = kA \sum_{n=0}^{N} \mathbf{c_n} T_n(x_j),$$

where $\mathbf{c_n} = \begin{bmatrix} a_n \\ b_n \end{bmatrix}$. Again, we can replace two rows by the boundary condition $u(\pm 1) = 0$:

$$\sum_{n=0}^{N} a_n T_n(\pm 1) = 0.$$

However, in this case we have two matrix rows corresponding to each of x_0 and x_N, but we only have "half" a boundary condition on each boundary. If we require the differential equation to be satisfied at the interior Gauss-Lobatto points, and add the two "half" boundary conditions, this gives us $2N$ equations; however, we have $2N+2$ unknowns (a_n and b_n). We try a number of different strategies to add enough equations:

1. Require the differential equation to be satisfied at one of the boundary points.

2. Overspecify the boundary conditions. As $v'(x) = ku$, add the additional boundary condition $v'(\pm 1) = 0$.

3. Consider the two equations separately, rather than as a system. Then, require the equation in $u'(x)$ to be satisfied at the interior collocation points, and the equation in $v'(x)$ to be satisfied at all collocation points. The boundary conditions on u provide the remaining two equations.

4. Homogenize the boundary conditions. Rather that having both u and v represented as a series of Chebyshev polynomials, define u in terms of $\phi_{2n}(x) = T_{2n}(x) - 1$ and $\phi_{2n+1}(x) = T_{2n+1}(x) - x$ for $n = 1, 2, \ldots$. Using this basis function means that the boundary condition $u(\pm 1) = 0$ is automatically satisfied, and thus we can just consider the differential equation at all the Gauss-Lobatto points.

Table 3.1 contains the analytical solution to the wave equation, for the ten modes, and the numerical results from applying Chebyshev collocation to the second-order equation. We compare the results of the different strategies for collocation on the first-order system in Table 3.2.

Table 3.1: Analytical solution for wavenumber k, calculated for the first ten modes, and numerical solution for the second-order equation solved using Chebyshev collocation.

Mode Number	Analyical	Second-Order Chebyshev
1	$0 + 1.5708\imath$	$0 + 1.5708\imath$
2	$0 + 3.1416\imath$	$0 + 3.1416\imath$
3	$0 + 4.7124\imath$	$0 + 4.7124\imath$
4	$0 + 6.2832\imath$	$0 + 6.2832\imath$
5	$0 + 7.8540\imath$	$0 + 7.8540\imath$
6	$0 + 9.4248\imath$	$0 + 9.4248\imath$
7	$0 + 10.9956\imath$	$0 + 10.9956\imath$
8	$0 + 12.5664\imath$	$0 + 12.5664\imath$
9	$0 + 14.1372\imath$	$0 + 14.1365\imath$
10	$0 + 15.7080\imath$	$0 + 15.7158\imath$

Table 3.2: Solutions for wavenumber k solved numerically as a first-order system using Chebyshev collocation.

Method 1	Method 2	Method 3	Method 4
$0.0000 - 2.5458\imath$	$0.0000 - 2.5458\imath$	$0.0000 - 2.5458\imath$	$-0.0000 - 2.5458\imath$
$0.0000 + 2.5458\imath$	$0.0000 + 2.5458\imath$	$0.0000 + 2.5458\imath$	$-0.0000 + 2.5458\imath$
$2.8541 - 2.8805\imath$	$-2.8541 - 2.8805\imath$	$-2.8541 - 2.8805\imath$	$2.8541 - 2.8805\imath$
$2.8541 + 2.8805\imath$	$-2.8541 + 2.8805\imath$	$-2.8541 + 2.8805\imath$	$2.8541 + 2.8805\imath$
$-2.8541 - 2.8805\imath$	$2.8541 - 2.8805\imath$	$2.8541 - 2.8805\imath$	$-2.8541 - 2.8805\imath$
$-2.8541 + 2.8805\imath$	$2.8541 + 2.8805\imath$	$2.8541 + 2.8805\imath$	$-2.8541 + 2.8805\imath$
$5.8753 - 4.9308\imath$	$5.8870 - 4.9192\imath$	$-5.9011 - 4.9361\imath$	$-5.8752 - 4.9308\imath$
$5.8753 + 4.9308\imath$	$5.8870 + 4.9192\imath$	$-5.9011 + 4.9361\imath$	$-5.8752 + 4.9308\imath$
$-5.8753 - 4.9308\imath$	$-5.8870 - 4.9192\imath$	$5.9011 - 4.9361\imath$	$5.8752 - 4.9308\imath$
$-5.8753 + 4.9308\imath$	$-5.8870 + 4.9192\imath$	$5.9011 + 4.9361\imath$	$5.8752 + 4.9308\imath$

The solutions for the four different first-order system Chebyshev collocation strategies all basically agree. Unfortunately, however, they don't agree at all with the solution for the second-order equation Chebyshev collocation, nor with the analytical solution.

3.5 Conclusions

Using Chebyshev collocation on a second-order equation works quite well, and, for our example of the wave equation, there's no reason not to consider the equation in this form. The system we are interested in, however, is quite a bit more complicated. Changing it from a first-order system into a second-order equation would be very messy. Thus, finite differences are a more convenient way to solve our problem numerically.

Chapter 4

Viscosity

4.1 Introduction

In previous models, we had neglected the effect of viscosity. The viscosity of the solar plasma is small enough that we expected viscous dissipation only to be important on a much smaller scale that supergranulation. However, since we have reproduced some of the observed wave-like behaviour, and are now looking for factors that might add to its speed, it is worth modelling any effect of turbulent viscosity.

Viscosity terms are easily added to the four equations in our alternative linear model. Thus we end up with the second-order system

$$\frac{d\rho_1}{dt} + \rho_0 \left(\frac{\partial u_{1x}}{\partial x} + \frac{\partial u_{1z}}{\partial z} \right) + u_{1z} \frac{d\rho_0}{dz} = 0, \tag{4.1}$$

$$\rho_0 \frac{du_{1x}}{dt} + \rho_0 u_{1z} \frac{dU_0}{dz} = -\frac{\partial p_1}{\partial x} + \mu \left(\frac{\partial^2 u_{1x}}{\partial x^2} + \frac{\partial^2 u_{1x}}{\partial z^2} \right), \tag{4.2}$$

$$\rho_0 \frac{du_{1z}}{dt} = -\frac{\partial p_1}{\partial z} - \rho_1 g + \mu \left(\frac{\partial^2 u_{1z}}{\partial x^2} + \frac{\partial^2 u_{1z}}{\partial z^2} \right), \tag{4.3}$$

$$\frac{dp_1}{dt} + u_{1z} \frac{dp_0}{dz} = c_0^2 \left(\frac{d\rho_1}{dt} + u_{1z} \frac{d\rho_0}{dz} \right), \tag{4.4}$$

where μ is the coefficient of dynamic viscosity. Because we now have second-order terms, rather than the strictly first-order terms we had before, we now need more boundary conditions. Thus, in addition to $u_{1z} = 0$, we require that $\frac{\partial u_{1x}}{\partial z} = 0$ on the boundaries.

As before, we consider wave solutions, of the form $\rho_1 = \rho(z)e^{\imath(kx-\omega t)}$, $u_{1x} = u(x)e^{\imath(kx-\omega t)}$, $u_{1z} = v(z)e^{\imath(kx-\omega t)}$, and $p_1 = p(z)e^{\imath(kx-\omega t)}$. We obtain linear equations, depending on wavenumber k and frequency ω:

$$(-\imath\omega + \imath k U_0)\, \rho(z) + \rho_0 \left[\imath k u(z) + v'(z) \right] + \frac{d\rho_0}{dz} v(z) = 0, \tag{4.5}$$

$$\rho_0 \left(-\imath\omega + \imath k U_0 \right) u(z) + \rho_0 \frac{dU_0}{dz} v(z) = -\imath k p(z) + \mu \left[-k^2 u(z) + u''(z) \right], \tag{4.6}$$

$$\rho_0 \left(-\imath\omega + \imath k U_0\right) v(z) = -p'(z) - g\rho(z) + \mu \left[-k^2 v(z) + v''(z)\right], \tag{4.7}$$

$$\left(-\imath\omega + \imath k U_0\right) p(z) - \rho_0 g v(z) = c_0^2 \left[\left(-\imath\omega + \imath k U_0\right) \rho(z) + \frac{d\rho_0}{dz} v(z)\right]. \tag{4.8}$$

4.2 Numerical Method

We apply a finite-difference scheme to our system of second-order differential equations, and obtain a matrix eigenvalue problem in ω, which is then solved using library methods.

We discretize z such that $z_0 = r_0$, where r_0 is the chosen lower boundary, and $z_N = R$, where R is the solar radius. We then have interior points z_j for $j = 1, \ldots, N-1$. We define $v_j \approx v(z_j)$. Our first boundary condition, zero vertical velocity at the top and bottom of the layer, then becomes $v_0 = 0$ and $v_N = 0$.

Our second boundary condition, $u'(z_0) = 0$ and $u'(z_N) = 0$, can be satisfied by considering u to be on a mesh off-set from that for v, and defining $u_j \approx u(z_{j-\frac{1}{2}})$. Then, by defining a "ghost point" across the boundary, we obtain

$$u'(z_0) \approx \frac{u(z_{\frac{1}{2}}) - u(z_{-\frac{1}{2}})}{r_{\frac{1}{2}} - r_{-\frac{1}{2}}} = 0.$$

This produces a condition on $z_{-\frac{1}{2}}$, our ghost point: $u(z_{-\frac{1}{2}}) = u(z_{\frac{1}{2}})$. Or, for our discretized variables, $u_0 = u_1$. Similarly, from $u'(R) = 0$, we get $u_{N+1} = u_N$. Because we have no boundary conditions for ρ or p, we consider them on the same off-set grid as u.

We apply central differencing to obtain first derivatives on the two meshes:

$$v'(z_{j-\frac{1}{2}}) \approx \frac{v_j - v_{j-1}}{z_j - z_{j-1}}, \quad \text{and} \quad p'(z_j) \approx \frac{p_{j+1} - p_j}{z_{j+\frac{1}{2}} - z_{j-\frac{1}{2}}}.$$

We apply a second central difference to obtain our second-derivative terms:

$$v''(z_j) \approx \frac{1}{z_{j+\frac{1}{2}} - z_{j-\frac{1}{2}}} \left[\frac{v_{j+1} - v_j}{z_{j+1} - z_j} - \frac{v_j - v_{j-1}}{z_j - z_{j-1}}\right],$$

$$u''(z_{j-\frac{1}{2}}) \approx \frac{1}{z_j - z_{j-1}} \left[\frac{u_{j+1} - u_j}{z_{j+\frac{1}{2}} - z_{j-\frac{1}{2}}} - \frac{u_j - u_{j-1}}{z_{j-\frac{1}{2}} - z_{j-\frac{3}{2}}}\right].$$

The boundary conditions on u_0 and u_{N+1} only arise in these second-derivative terms. Thus, we write two special cases:

$$u''(z_{\frac{1}{2}}) \approx \frac{1}{z_1 - z_0} \left[\frac{1}{z_{\frac{3}{2}} - z_{\frac{1}{2}}} u_2 + \frac{-1}{z_{\frac{3}{2}} - r_{\frac{1}{2}}} u_1\right],$$

$$u''(z_{N-\frac{1}{2}}) \approx \frac{1}{z_N - z_{N-1}} \left[\frac{-1}{z_{N-\frac{1}{2}} - z_{N-\frac{3}{2}}} u_N + \frac{1}{z_{N-\frac{1}{2}} - z_{N-\frac{3}{2}}} u_{N-1}\right].$$

We substitute these into (4.5) – (4.8), and use interpolation to obtain values for the variables on the other offset mesh. Equation (4.7) must be satisfied at z_j for $j = 1, \ldots, N-1$. The remaining equations must be satisfied at $z_{j-\frac{1}{2}}$ for $j = 1, \ldots, N$. Thus we have a linear system:

$$\begin{aligned}&(-\imath\omega + \imath k U_0)\,\rho_j + \imath k \rho_0 u_j + \\ &\quad \left[\left(\frac{1}{2}\frac{d\rho_0}{dz} + \frac{\rho_0}{z_j - z_{j-1}}\right) v_j + \left(\frac{1}{2}\frac{d\rho_0}{dz} - \frac{\rho_0}{z_j - z_{j-1}}\right) v_{j-1}\right] = 0,\end{aligned} \tag{4.9}$$

$$\begin{aligned}&\frac{-\mu}{(z_j - z_{j-1})\left(z_{j+\frac{1}{2}} - z_{j-\frac{1}{2}}\right)} u_{j+1} + \frac{-\mu}{(z_j - z_{j-1})\left(z_{j-\frac{1}{2}} - z_{j-\frac{3}{2}}\right)} u_{j-1} + \\ &\quad \left(\rho_0\,(-\imath\omega + \imath k U_0) + \mu k^2 + \frac{\mu}{z_j - z_{j-1}}\left(\frac{1}{z_{j+\frac{1}{2}} - z_{j-\frac{1}{2}}} + \frac{1}{z_{j-\frac{1}{2}} - z_{j-\frac{3}{2}}}\right)\right) u_j + \\ &\quad \left[\frac{1}{2}\rho_0 \frac{dU_0}{dz} v_j + \frac{1}{2}\rho_0 \frac{dU_0}{dz} v_{j-1}\right] + \imath k p_j = 0,\end{aligned} \tag{4.10}$$

$$\begin{aligned}&\frac{-\mu}{\left(z_{j+\frac{1}{2}} - z_{j-\frac{1}{2}}\right)(z_j - z_{j-1})} v_{j-1} + \frac{-\mu}{\left(z_{j+\frac{1}{2}} - z_{j-\frac{1}{2}}\right)(z_{j+1} - z_j)} v_{j+1} + \\ &\quad \left(\rho_0\,(-\imath\omega + \imath k U_0) + \mu k^2 + \frac{\mu}{z_{j+\frac{1}{2}} - z_{j-\frac{1}{2}}}\left(\frac{1}{z_{j+1} - z_j} + \frac{1}{z_j - z_{j-1}}\right)\right) v_j + \\ &\quad \left[\frac{1}{2} g \rho_j + \frac{1}{2} g \rho_{j+1}\right] + \left[\frac{1}{z_{j+\frac{1}{2}} - z_{j-\frac{1}{2}}} p_{j+1} + \frac{-1}{z_{j+\frac{1}{2}} - z_{j-\frac{1}{2}}} p_j\right] = 0,\end{aligned} \tag{4.11}$$

$$\begin{aligned}&c_0^2\,(-\imath\omega + \imath k U_0)\,\rho_j - (-\imath\omega + \imath k U_0)\,p_j + \\ &\quad \left[\left(\frac{1}{2}\rho_0 g + \frac{1}{2}\frac{d\rho_0}{dz}\right) v_j + \left(\frac{1}{2}\rho_0 g + \frac{1}{2}\frac{d\rho_0}{dz}\right) v_{j-1}\right] = 0.\end{aligned} \tag{4.12}$$

As (4.11) must hold at $N-1$ points, and the others hold at N points, we can write these equations in matrix form. We define vectors

$$\vec{\rho} = \begin{bmatrix} \rho_1 \\ \vdots \\ \rho_N \end{bmatrix}, \quad \vec{u} = \begin{bmatrix} u_1 \\ \vdots \\ u_N \end{bmatrix}, \quad \vec{v} = \begin{bmatrix} v_1 \\ \vdots \\ v_{N-1} \end{bmatrix}, \quad \vec{p} = \begin{bmatrix} p_1 \\ \vdots \\ p_N \end{bmatrix}.$$

Then (4.9) – (4.12) become

$$A\vec{\rho} + B\vec{u} + C\vec{v} = 0, \tag{4.13}$$

$$D\vec{u} + E\vec{v} + F\vec{p} = 0, \tag{4.14}$$

$$G\vec{\rho} + H\vec{v} + I\vec{p} = 0, \tag{4.15}$$

$$J\vec{\rho} + K\vec{v} + L\vec{p} = 0. \tag{4.16}$$

The frequency ω appears linearly in matrices A, D, H, J, and L, where $A = \omega A_1 + A_0$, etc.

These matrix equations can be combined into block matrices, producing an eigenvalue problem:

$$\omega \begin{bmatrix} A_1 & 0 & 0 & 0 \\ 0 & D_1 & 0 & 0 \\ 0 & 0 & H_1 & 0 \\ J_1 & 0 & 0 & L_1 \end{bmatrix} \vec{\Phi} + \begin{bmatrix} A_0 & B & C & 0 \\ 0 & D_0 & E & F \\ G & 0 & H_0 & I \\ J_0 & 0 & K & L_0 \end{bmatrix} \vec{\Phi} = 0, \text{ with } \vec{\Phi} = \begin{bmatrix} \vec{\rho} \\ \vec{u} \\ \vec{v} \\ \vec{p} \end{bmatrix}.$$

This matrix eigenvalue problem is then solved using library eigenvalue solvers.

4.2.1 Scaling of Variables

As with our previous model, the physical quantities need to be scaled to avoid overflow, underflow and loss of accuracy. We keep the same scaling for density, pressure and velocity. We need to find a consistent scaling for our coefficient of dynamic viscosity. Obviously, the μ terms in our differential equations must have the same dimensions as the other terms. Thus, $\left[\mu \frac{\partial^2 u_{1z}}{\partial x^2}\right] = [\rho_1 g]$. If we denote the dimensions of length, time and mass as L, T, and M respectively, we obtain $[\mu] = \frac{M}{LT}$. The scaling for length, time and mass remains unchanged; thus, our computational value for μ will be 10^{-12} times the physical value.

4.3 Results

We begin by using our model to investigate the effects of viscosity, which is constant throughout the layer. This relationship is show in Figure 4.1, at horizontal wavenumber $kR = 50$.

For low viscosity, the phase speeds are the same as for the non-viscous case. For coefficient of dynamic viscosity μ above 10^4, the convective modes start to increase. The higher-order modes increase at lower μ. Modes peak at phase speeds of 60–70 m/s, and then disappear. Obviously, the higher-order modes peak at lower viscosities.

The sharp drop in phase speed at high viscosity signifies a change in the type of mode. When the viscosity is high enough, we no longer obtain convective modes. This difference can be seen in the eigenfunctions associated with the modes.

As we can see in Figure 4.2, the eigenfunctions for convective modes have big peaks near the surface, and quickly decay to zero deeper in the layer. The non-convective modes obtained at higher viscosity (Figure 4.3) are small near the surface and have big peaks deeper in the layer. However, for the convective modes, in this case, the oscillations extend much deeper into the layer than in the non-viscous case, reaching depths with higher shear velocities.

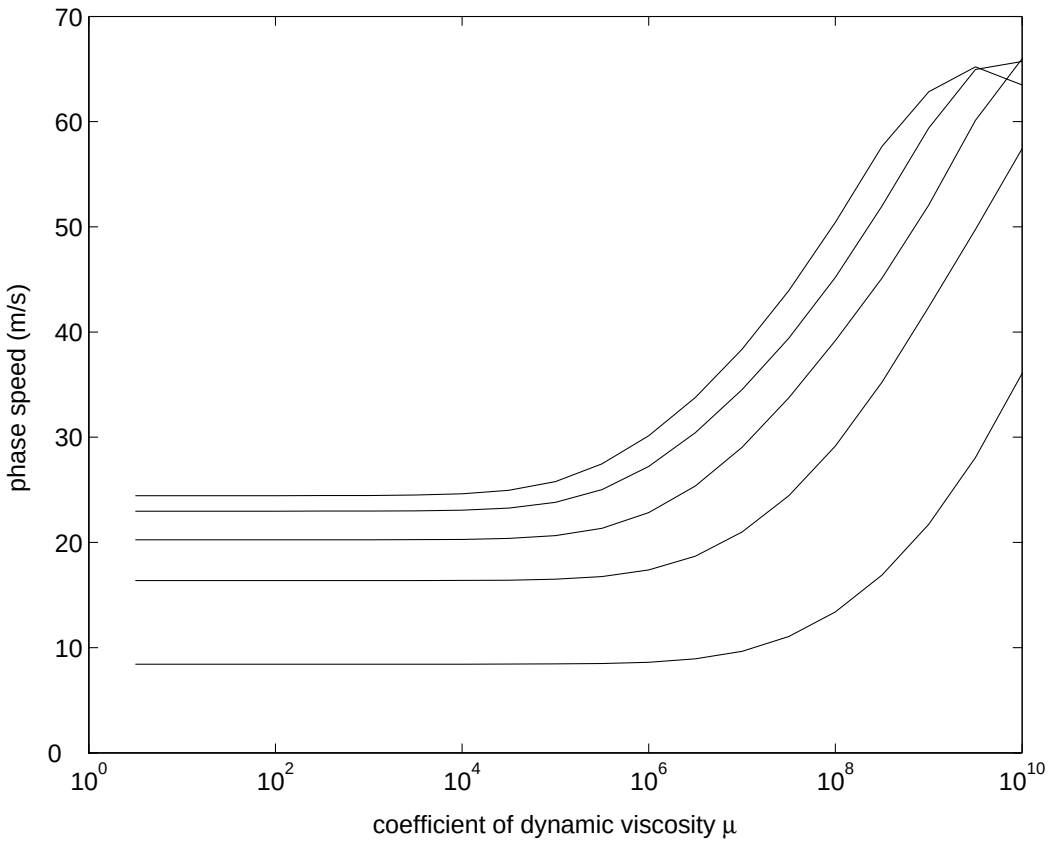

Figure 4.1: Phase speeds of the first five modes, as a function of constant viscosity.

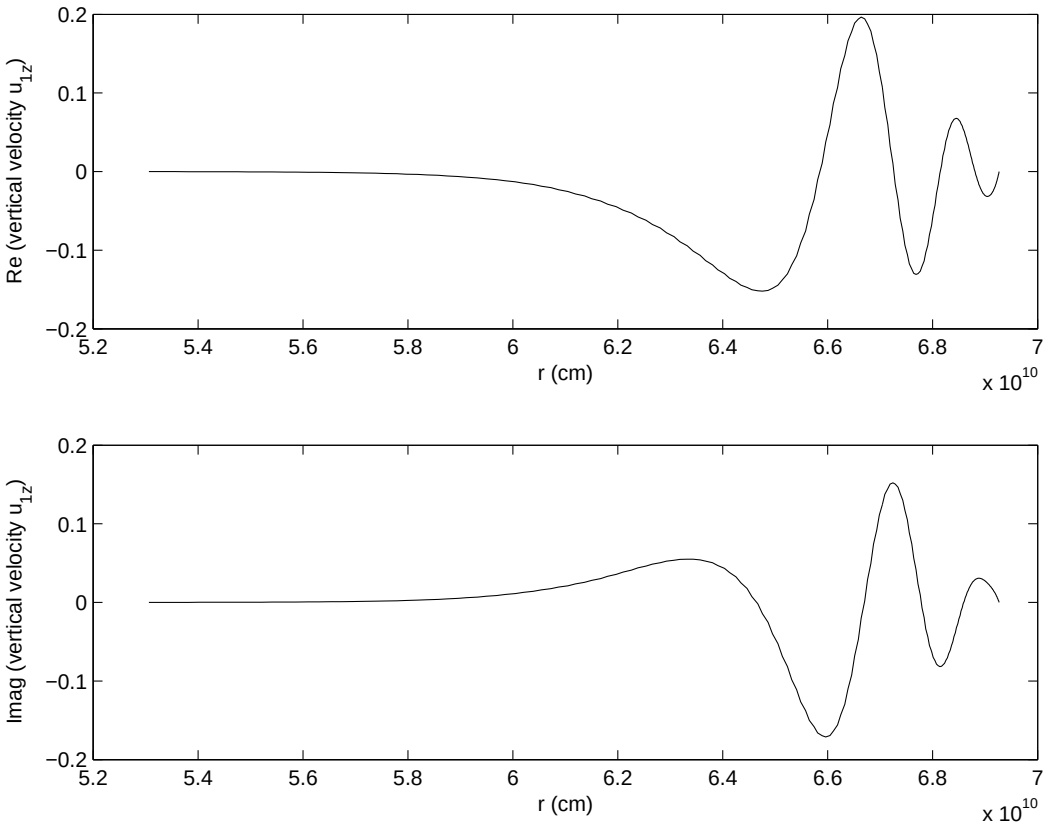

Figure 4.2: Eigenfunction for a convective mode.

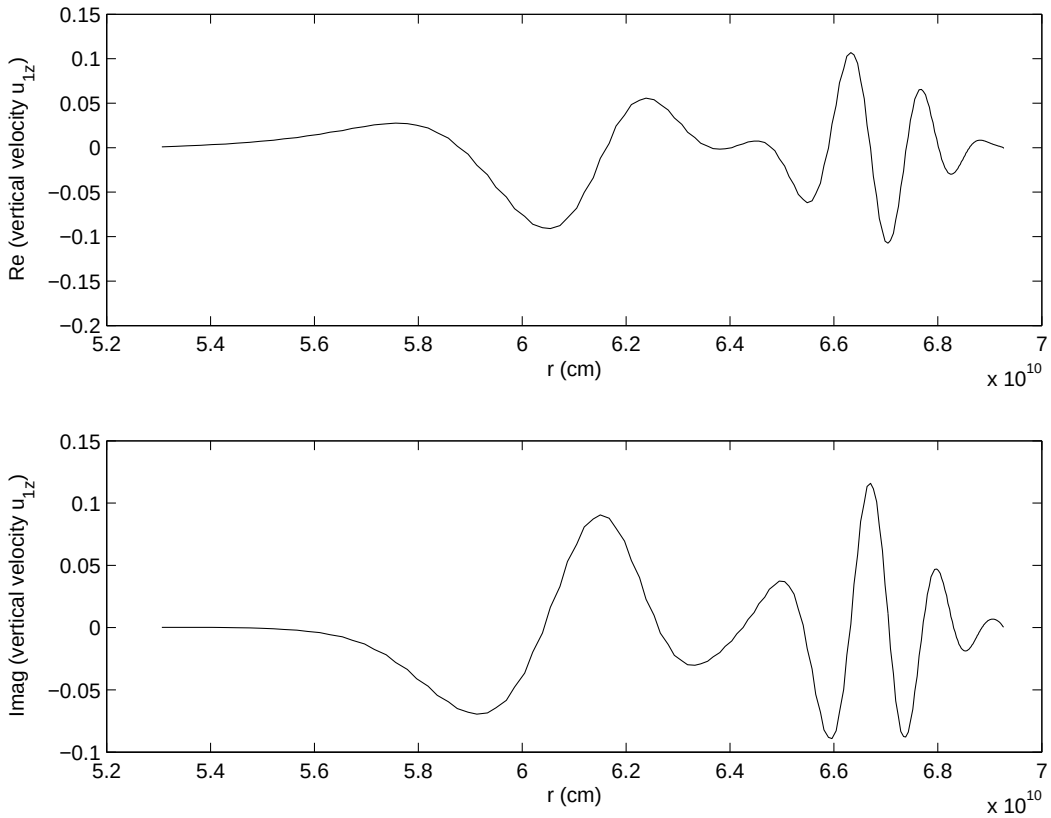

Figure 4.3: Eigenfunction for a non-convective mode obtained with high viscosity.

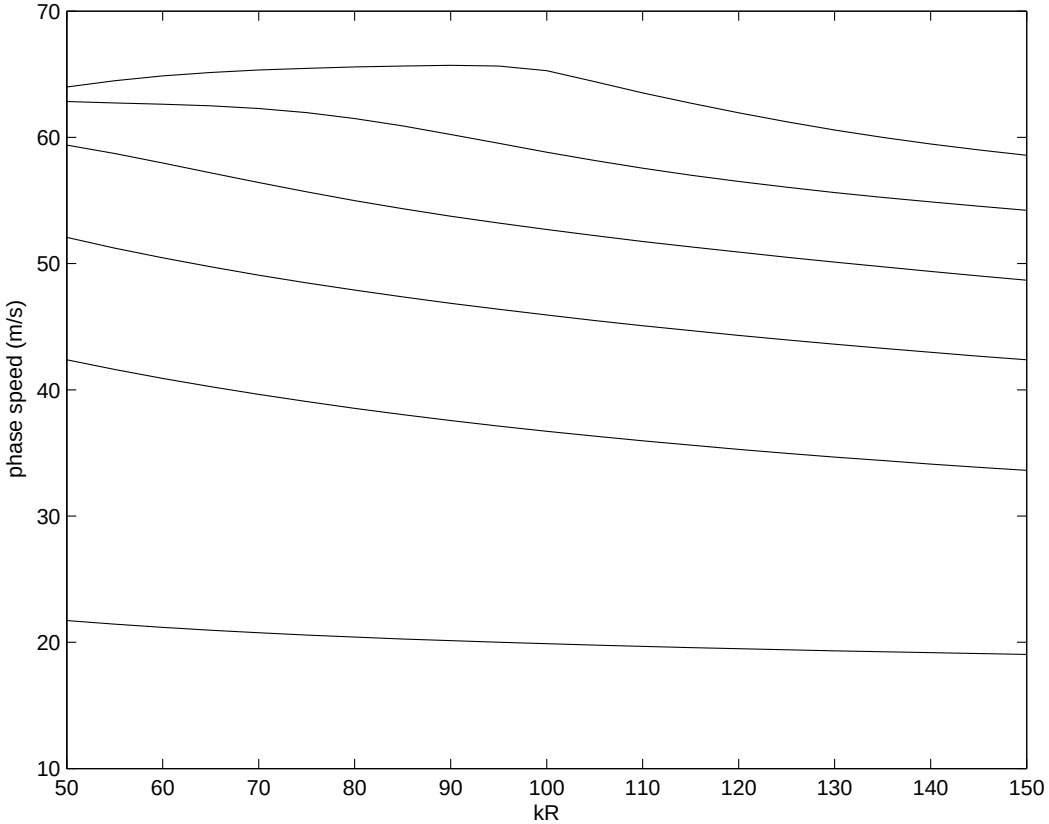

Figure 4.4: Phase speeds for convective modes with a constant coefficient of dynamic viscosity of 10^9 g cm^{-1} s^{-1}.

A coefficient of dynamic viscosity of 10^9 g cm^{-1} s^{-1} is in the range where convective modes are obtained, yet they have substantially higher wavespeeds than the non-viscous case. Figure 4.4 shows the phasespeeds for this viscosity, as a function of horizontal wavenumber. Phase speeds near the observed 65 m/s are obtained in this case. Figure 4.5 shows an estimate of turbulent viscosity, obtained from mixing length theory, as a function of depth. Its value obviously exceeds that necessary to reproduce the observed phase speed of the convective modes.

4.4 Conclusions

In our original linear model, the presence of a shear gradient caused the unstable convective modes to become running waves. These modes were constrained near the top of the convective layer, and thus travelled slower than the observed supergranular waves. The addition of turbulent viscosity produces travelling modes similar to those in the original model; however, the modes now extend deeper into the layer and have higher phase speeds

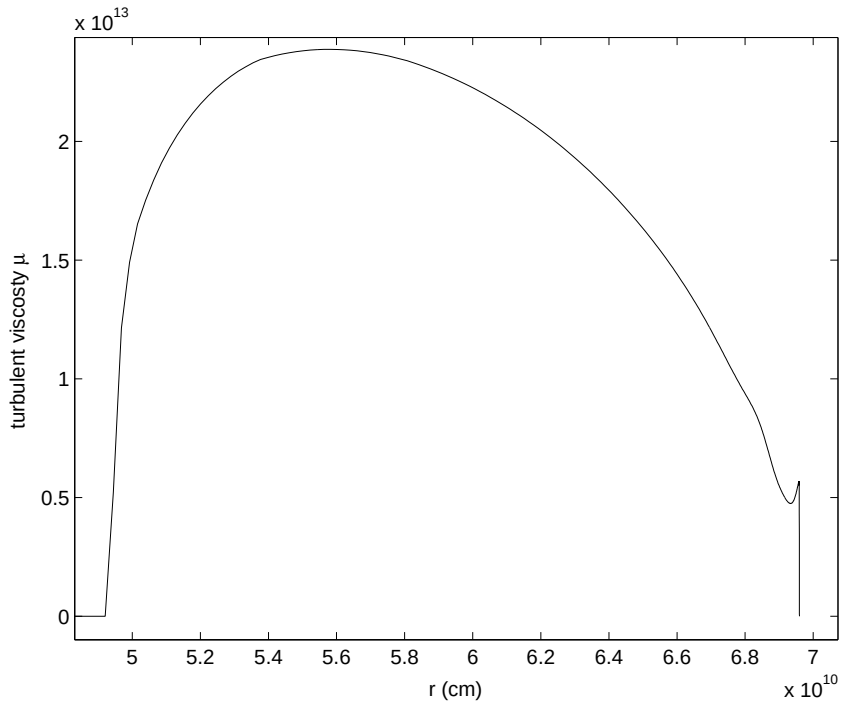

Figure 4.5: Estimate of the coefficient of dynamic viscosity μ as a function of radius, obtained from the mixing length theory of the solar convective zone.

for a sufficiently large value of the coefficient of turbulent viscosity. If the viscosity is too great, the unstable convective modes disappear.

The observed speed can be reproduced by a constant coefficient of dynamic viscosity of the order of 10^9 g cm^{-1} s^{-1}, throughout the convective zone. Estimations from the mixing length theory of the solar convective zone suggest that this value is reasonable in the Sun. Thus, while the addition of turbulent viscosity contributes substantially to the speed of the convective waves and can account for the observations, we should also consider other possible contributing factors.

Chapter 5

Magnetic Field

5.1 Introduction

Our previous models depend solely on hydrodynamics; however, in the Sun, magnetic field has a great effect. The magnetic field is the source of all solar activity, including sunspots and flares. Although we are interested in the behaviour of supergranulation in the quiet (non-active) Sun, magnetism is still present in this case, and its effect must be considered.

The solar magnetic field is very complicated. Even outside active regions, the magnetic flux is not evenly distributed, but rather, becomes concentrated at the boundaries of granular and supergranular cells. The magnetic flux is concentrated in the downdrafts, where the magnetic flux forms vertical columns, called flux tubes. The magnetic field at these concentrated spots is about 0.1 T, but much weaker for the majority of the solar surface.

Because of our interest in non-local behaviour, we consider a model in which the magnetic field varies only in depth, thus ignoring the complicated structures of the flux tubes and sunspots.

5.1.1 Governing Equations

The dynamics of magnetic fluids is described by the Magnetohydrodynamic (MHD) equations. The addition of magnetic field leaves the continuity equation unchanged:

$$\frac{\partial \rho}{\partial t} + \nabla \cdot (\rho \mathbf{v}) = 0. \tag{5.1}$$

A new external force term is added to the equations of motion: the Lorentz force, given by $\mathbf{j} \times \mathbf{B}$. This is the source of coupling between the fluid equations and the magnetic equations:

$$\rho \frac{\partial \mathbf{v}}{\partial t} + \rho(\mathbf{v} \cdot \nabla)\mathbf{v} = -\nabla p + \mathbf{j} \times \mathbf{B} + \rho \mathbf{g}. \tag{5.2}$$

The added magnetic field also has no effect on the energy equation:

$$\frac{\partial p}{\partial t} + \mathbf{v} \cdot \nabla p = -\gamma p \nabla \cdot \mathbf{v}. \tag{5.3}$$

Now, Maxwell's equations are required to account for the properties of magnetism. Ampere's Law is

$$\nabla \times \mathbf{B} = \mathbf{j} + \frac{1}{c^2}\frac{\partial \mathbf{E}}{\partial t}. \tag{5.4}$$

The last term in Ampere's Law is the displacement current.

The induction of magnetic fields by the spatial variation of electric fields is given by Faraday's Law:

$$\nabla \times \mathbf{E} = -\frac{\partial \mathbf{B}}{\partial t}. \tag{5.5}$$

If we consider the typical lengthscale of plasma variation to be L and timescale to be T, we can define a typical plasma velocity $V = \frac{L}{T}$. These can be used to approximate the terms in (5.5):

$$\nabla \times \mathbf{E} \approx \frac{E}{L} \text{ and } \frac{\partial \mathbf{B}}{\partial t} \approx \frac{B}{T}.$$

These terms must be equal; thus

$$E = \frac{L}{T}B = VB.$$

Now, considering the terms in (5.4), we see that the left-hand side of the equation is approximately $\frac{B}{L}$. The displacement current, however, is

$$\frac{1}{c^2}\frac{\partial \mathbf{E}}{\partial t} \approx \frac{1}{c^2}\frac{E}{T} = \frac{V}{c^2}\frac{B}{T} = \frac{B}{L}\frac{V}{c^2}\frac{L}{T} = \frac{B}{L}\frac{V^2}{c^2}.$$

In the MHD approximation, we consider typical plasma velocities $V^2 \ll c^2$, and thus can simplify Ampere's Law to

$$\mathbf{j} = \nabla \times \mathbf{B}. \tag{5.6}$$

Ohm's Law is the remaining electromagnetic equation:

$$\frac{1}{\sigma}\mathbf{j} = \mathbf{E} + \mathbf{v} \times \mathbf{B},$$

where σ is the electric conductivity. For the Sun, we assume infinite conductivity, and thus Ohm's Law reduces to

$$\mathbf{E} = -\mathbf{v} \times \mathbf{B}. \tag{5.7}$$

As we are interested in the effect of the magnetic field, we want magnetic equations that include only this one added term. Thus we combine (5.5) and (5.7) to get a single additional equation in $\mathbf{B}$, and substitute (5.6) into (5.2). We then end up with five MHD equations:

$$\frac{\partial \rho}{\partial t} + \nabla \cdot (\rho \mathbf{v}) = 0, \tag{5.8}$$

$$\rho\frac{\partial \mathbf{v}}{\partial t} + \rho(\mathbf{v}\cdot\nabla)\mathbf{v} = -\nabla p - \frac{1}{2}\nabla(\mathbf{B}\cdot\mathbf{B}) + \mathbf{B}\cdot\nabla\mathbf{B} + \rho\mathbf{g}, \tag{5.9}$$

$$\frac{\partial p}{\partial t} + \mathbf{v}\cdot\nabla p = -\gamma p\nabla\cdot\mathbf{v}, \tag{5.10}$$

$$\nabla\cdot\mathbf{B} = 0, \tag{5.11}$$

$$\frac{\partial \mathbf{B}}{\partial t} = (\mathbf{B}\cdot\nabla)\mathbf{v} - (\mathbf{v}\cdot\nabla)\mathbf{B} + \mathbf{v}(\nabla\cdot\mathbf{B}) - \mathbf{B}(\nabla\cdot\mathbf{v}). \tag{5.12}$$

These equations form the basis of our magnetic field model.

5.2 Linear Model

To obtain our linear model, we consider linear perturbations to density, velocity, pressure and magnetic field: $\rho(x,y,z,t) = \rho_0(z) + \rho_1(x,y,z,t)$, $\mathbf{v}(x,y,z,t) = \mathbf{v}_0(z) + \mathbf{v}_1(x,y,z,t)$, $p(x,y,z,t) = p_0(z) + p_1(x,y,z,t)$, and $\mathbf{B}(x,y,z,t) = \mathbf{B}_0(z) + \mathbf{B}_1(x,y,z,t)$.

We investigate the effect of shear flow and a horizontal magnetic field by taking unperturbed flows and fields of $\mathbf{v}_0 = (U_0(z), 0, 0)$ and $\mathbf{B}_0 = (B_0(z), 0, 0)$. The corresponding perturbations are $\mathbf{v}_1 = (v_{1x}, v_{1y}, v_{1z})$ and $\mathbf{B}_1 = (b_{1x}, b_{1y}, b_{1z})$.

By substituting into the MHD equations and keeping only the first-order terms in the perturbation variables, we obtain a set of linear equations:

$$\frac{d\rho_1}{dt} + \rho_0\nabla\cdot\mathbf{v}_1 + v_{1z}\frac{d\rho_0}{dz} = 0, \tag{5.13}$$

$$\rho_0\frac{dv_{1x}}{dt} + \rho_0\frac{dU_0}{dz}v_{1z} = -\frac{\partial p_1}{\partial x} + \frac{dB_0}{dz}b_{1z}, \tag{5.14}$$

$$\rho_0\frac{dv_{1y}}{dt} = -\frac{\partial p_1}{\partial y} + B_0\left(\frac{\partial b_{1y}}{\partial x} - \frac{\partial b_{1x}}{\partial y}\right), \tag{5.15}$$

$$\rho_0\frac{dv_{1z}}{dt} = -\frac{\partial p_1}{\partial z} + B_0\left(\frac{\partial b_{1z}}{\partial x} - \frac{\partial b_{1x}}{\partial z}\right) - \frac{dB_0}{dz}b_{1x} - \rho_1 g, \tag{5.16}$$

$$\frac{dp_1}{dt} + \frac{dB_0}{dz}v_{1z} = c_0^2\left(\frac{d\rho_1}{dt} + \frac{d\rho_0}{dz}v_{1z}\right), \tag{5.17}$$

$$\frac{db_{1x}}{dt} + \frac{dB_0}{dz}v_{1z} = B_0\frac{\partial v_{1x}}{\partial x} + \frac{dU_0}{dz}b_{1z} - B_0\nabla\cdot\mathbf{v}_1, \tag{5.18}$$

$$\frac{db_{1y}}{dt} = B_0\frac{\partial v_{1y}}{\partial x}, \tag{5.19}$$

$$\frac{db_{1z}}{dt} = B_0\frac{\partial v_{1z}}{\partial x}, \tag{5.20}$$

where $\frac{d}{dt} \equiv \frac{\partial}{\partial t} + U_0\frac{\partial}{\partial x}$. The unperturbed terms also yield the equation of magnetohydrostatic equilibrium:

$$\frac{dp_0}{dz} = -B_0\frac{dB_0}{dz} - \rho_0 g. \tag{5.21}$$

We consider a two-dimensional model, and thus drop v_{1y}, b_{1y} and (5.15) and (5.19). Then, as we are interested in travelling wave solutions, we assume the perturbation variables

take the form

$$\begin{pmatrix} \rho_1 & v_{1x} & v_{1z} & p_1 & b_{1x} & b_{1z} \end{pmatrix} = \begin{pmatrix} \rho(z) & u(z) & v(z) & p(z) & b_x(z) & b_z(z) \end{pmatrix} e^{\imath(kx-\omega t)}.$$

We obtain linear equations depending on wavenumber k and frequency ω:

$$(-\imath\omega + \imath kU_0)\rho(z) + \rho_0[\imath ku(z) + v'(z)] + \frac{d\rho_0}{dz}v(z) = 0, \quad (5.22)$$

$$\rho_0(-\imath\omega + \imath kU_0)u(z) + \rho_0\frac{dU_0}{dz}v(z) = -\imath kp(z) + \frac{dB_0}{dz}b_z(z), \quad (5.23)$$

$$\rho_0(-\imath\omega + \imath kU_0)v(z) = -p'(z) + B_0(\imath kb_z(z) - b_x'(z)) - \frac{dB_0}{dz}b_x(z) - g\rho(z), \quad (5.24)$$

$$(-\imath\omega + \imath kU_0)p(z) + \left(-B_0\frac{dB_0}{dz} - \rho_0 g\right)v(z) = c_0^2\left((-\imath\omega + \imath kU_0)\rho(z) + \frac{d\rho_0}{dz}v(z)\right), \quad (5.25)$$

$$(-\imath\omega + \imath kU_0)b_x(z) + \frac{dB_0}{dz}v(z) = B_0\imath ku(z) + \frac{dU_0}{dz}b_z(z) - B_0(\imath ku(z) + v'(z)), \quad (5.26)$$

$$(-\imath\omega + \imath kU_0)b_z(z) = \imath kB_0 v(z). \quad (5.27)$$

5.3 Previous Work

Hughes and Tobias have considered the problem of the instability of a plane-parallel shear flow with the additional influence of a magnetic field. They consider a simple model in which the flow is incompressible, the effect of gravity is ignored, and both viscosity and magnetic diffusion are neglected. They consider perturbations to the variables in the ideal MHD equations, and assume a functional form for these variables of $u(x, y, z, t) = u(z)\exp\imath(\alpha x + \beta y - \alpha ct)$, etc.

Squire's theorem, for the purely hydrodynamic problem (i.e. with $B = 0$) involves reducing the general three-dimensional linear stability problem to an equivalent two-dimensional problem. This tranformation shows that for each unstable three-dimensional disturbance of an inviscid flow there is a corresponding two-dimensional mode with a larger growth rate. Hughes and Tobias apply this transformation to a general magnetic case, showing that Squire's theorem applies to a perfectly conducting fluid, and thus they consider the corresponding two-dimensional problem.

They then modify Howard's semicircle theorem, which bounds the wavespeed of unstable modes within a specified semicircle. They find that including a magnetic field both tightens this constraining semicircle and produces a second, non-concentric, semicircle, in which the wave speed must lie. When either of these semicircles does not exist, or when they do not intersect, there can be no unstable modes.

Initially, it may seem that these added constraints will lead to smaller wave speeds for unstable modes than in the non-magnetic case. However, the phase speeds obtained in our previous model were not near the maximum allowed by Howard's semicircle theorem. The addition of a second non-concentric semicircle constraint could also have the effect of increasing the minimum obtainable wave speeds. Thus, it is not implausible to expect higher

phase speeds from a model including magnetic field.

5.4 Numerical Method

We apply a finite difference scheme to our system of first-order differential equations, and obtain a matrix eigenvalue problem in ω, which is then solved using library methods.

As boundary conditions, we use zero vertical velocity at the top and bottom of our layer. We discretize z such that $z_0 = r_0$, where r_0 is our chosen lower boundary, and $z_N = R$, where R is the solar radius. We then have interior points z_j for $j = 1, \ldots, N-1$. We define $v_j \approx v(z_j)$. Then the boundary conditions become $v_0 = 0$ and $v_N = 0$. Because we have no boundary conditions on the other variables, we consider them on a mesh offset from that for v: $p_j \approx p(z_{j-\frac{1}{2}})$, etc. Then we can apply central differencing to obtain derivatives on these two meshes:

$$v'(z_{j-\frac{1}{2}}) \approx \frac{v_j - v_{j-1}}{z_j - z_{j-1}} \quad \text{and} \quad p'(z_j) \approx \frac{p_{j+1} - p_j}{z_{j+\frac{1}{2}} - z_{j-\frac{1}{2}}}.$$

We substitute these into (5.22) – (5.27) and use interpolation to obtain values for the variables on the other offset mesh. Equation (5.24) must be satisfied, in our approximation, at z_j for $j = 1, \ldots, N-1$. The remaining equations must be satisfied at $z_{j-\frac{1}{2}}$ for $j = 1, \ldots, N$. Thus we have a linear system:

$$\begin{aligned}
&(-\imath\omega + \imath k U_0)\,\rho_j + \imath k \rho_0 u_j \\
&\quad + \left[\left(\frac{1}{2}\frac{d\rho_0}{dz} - \frac{\rho_0}{r_j - r_{j-1}}\right) v_{j-1} + \left(\frac{1}{2}\frac{d\rho_0}{dz} + \frac{\rho_0}{r_j - r_{j-1}}\right) v_j\right] = 0, && (5.28)\\
&\rho_0\,(-\imath\omega + \imath k U_0)\,u_j \\
&\quad + \left[\frac{1}{2}\rho_0 \frac{dU_0}{dz} v_{j-1} \frac{1}{2}\rho_0 \frac{dU_0}{dz} v_j\right] + \imath k p_j - \frac{dB_0}{dz} b_{z_j} = 0, && (5.29)\\
&\left[\frac{1}{2} g\rho_j + \frac{1}{2} g\rho_{j+1}\right] + \left[\frac{-1}{r_{j+\frac{1}{2}} - r_{j-\frac{1}{2}}} p_j + \frac{1}{r_{j+\frac{1}{2}} - r_{j-\frac{1}{2}}} p_{j+1}\right] \\
&\quad + \left[\left(\frac{1}{2}\frac{dB_0}{dz} - \frac{B_0}{r_{j+\frac{1}{2}} - r_{j-\frac{1}{2}}}\right) b_{x_j} + \left(\frac{1}{2}\frac{dB_0}{dz} + \frac{B_0}{r_{j+\frac{1}{2}} - r_{j-\frac{1}{2}}}\right) b_{x_{j+1}}\right] \\
&\quad + \left[-\frac{1}{2}\imath k B_0 b_{z_j} - \frac{1}{2}\imath k B_0 b_{z_{j+1}}\right] + \rho_0\,(-\imath\omega + \imath k U_0)\,v_j = 0, && (5.30)\\
&\left[-\frac{1}{2}\left(B_0 \frac{dB_0}{dz} + \rho_0 g c_0^2 \frac{d\rho_0}{dz}\right) v_{j-1} - \frac{1}{2}\left(B_0 \frac{dB_0}{dz} + \rho_0 g + c_0^2 \frac{d\rho_0}{dz}\right) v_j\right] \\
&\quad - c_0^2\,(-\imath\omega + \imath k U_0)\,\rho_j + (-\imath\omega + \imath k U_0)\,p_j = 0, && (5.31)\\
&\left[\left(\frac{1}{2}\frac{dB_0}{dz} - \frac{B_0}{r_j - r_{j-1}}\right) v_{j-1} + \left(\frac{1}{2}\frac{dB_0}{dz} + \frac{B_0}{r_j - r_{j-1}}\right) v_j\right] \\
&\quad + (-\imath\omega + \imath k U_0)\,b_{x_j} - \frac{dU_0}{dz} b_{x_j} = 0, && (5.32)
\end{aligned}$$

$$\left[-\frac{1}{2}\imath k B_0 v_{j-1} - \frac{1}{2}\imath k B_0 v_j\right] + (-\imath\omega + \imath k U_0)\, b_{z_j} = 0. \tag{5.33}$$

As (5.30) must hold at $N-1$ points, and the others hold at N points, we can write these equations in matrix form. We define vectors

$$\vec{\rho} = \begin{bmatrix} \rho_1 \\ \vdots \\ \rho_N \end{bmatrix}, \quad \vec{u} = \begin{bmatrix} u_1 \\ \vdots \\ u_N \end{bmatrix}, \quad \vec{v} = \begin{bmatrix} v_1 \\ \vdots \\ v_{N-1} \end{bmatrix},$$

$$\vec{p} = \begin{bmatrix} p_1 \\ \vdots \\ p_N \end{bmatrix}, \quad \vec{b_x} = \begin{bmatrix} b_{x_1} \\ \vdots \\ b_{x_N} \end{bmatrix}, \quad \vec{b_z} = \begin{bmatrix} b_{z_1} \\ \vdots \\ b_{z_N} \end{bmatrix}.$$

Then, equations 5.28 - 5.33 become

$$A\vec{\rho} + B\vec{u} + C\vec{v} = 0, \tag{5.34}$$

$$D\vec{u} + E\vec{v} + F\vec{p} + G\vec{b_x} = 0, \tag{5.35}$$

$$H\vec{\rho} + I\vec{v} + J\vec{p} + K\vec{b_x} + L\vec{b_z} = 0, \tag{5.36}$$

$$M\vec{\rho} + \mathcal{N}\vec{v} + \mathcal{O}\vec{p} = 0, \tag{5.37}$$

$$P\vec{v} + Q\vec{b_x} + R\vec{b_z} = 0, \tag{5.38}$$

$$S\vec{v} + T\vec{b_z} = 0. \tag{5.39}$$

The frequency ω appears linearly in matrices A, D, I, M, $\mathcal{O}$, Q, and T ($A = \omega A_1 + A_0$, etc.).

These matrix equations can be combined into block matrices, producing an eigenvalue problem:

$$\omega \begin{bmatrix} A_1 & 0 & 0 & 0 & 0 & 0 \\ 0 & D_1 & 0 & 0 & 0 & 0 \\ 0 & 0 & I_1 & 0 & 0 & 0 \\ M_1 & 0 & 0 & \mathcal{O}_1 & 0 & 0 \\ 0 & 0 & 0 & 0 & Q_1 & 0 \\ 0 & 0 & 0 & 0 & 0 & T_1 \end{bmatrix} \vec{\Phi} + \begin{bmatrix} A_0 & B & C & 0 & 0 & 0 \\ 0 & D_0 & E & F & 0 & G \\ H & 0 & I_0 & J & K & L \\ M_0 & 0 & \mathcal{N} & \mathcal{O}_0 & 0 & 0 \\ 0 & 0 & P & 0 & Q_0 & R \\ 0 & 0 & S & 0 & 0 & T_0 \end{bmatrix} \vec{\Phi} = 0,$$

$$\text{where } \vec{\Phi} = \begin{bmatrix} \vec{\rho} \\ \vec{u} \\ \vec{v} \\ \vec{p} \\ \vec{b_x} \\ \vec{b_z} \end{bmatrix}.$$

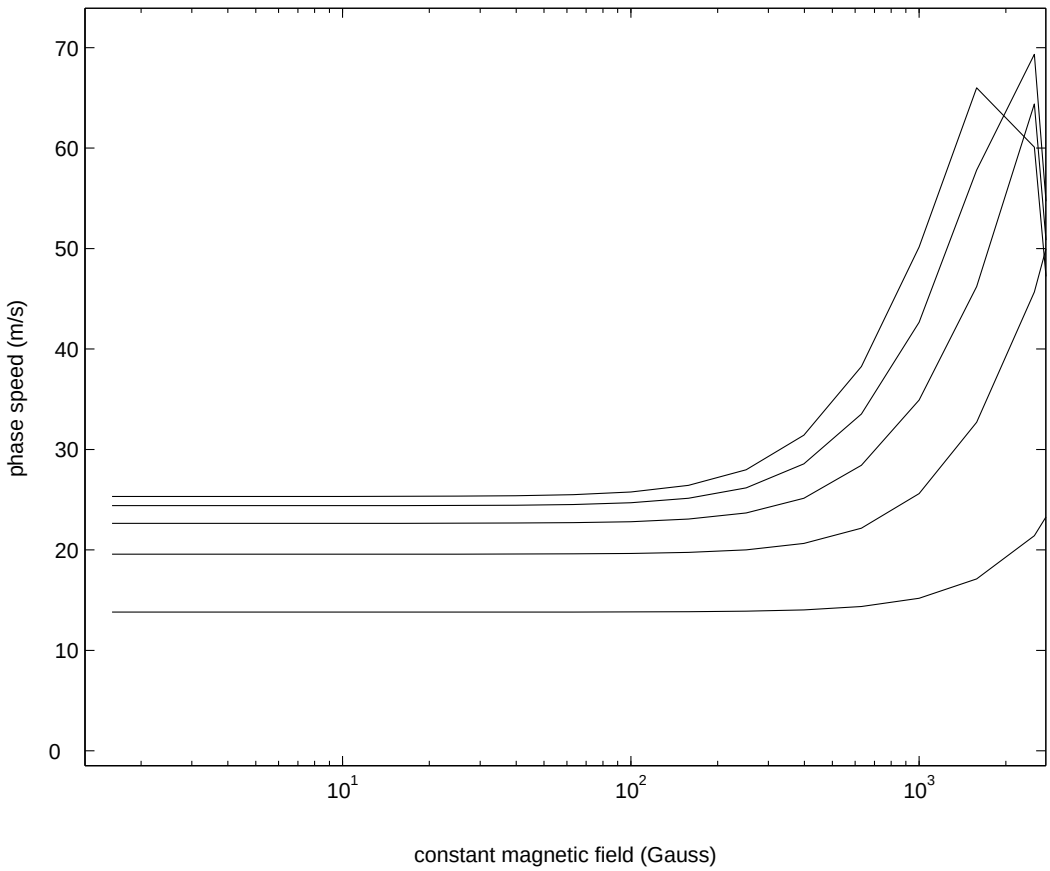

Figure 5.1: Phase speeds of the first five modes, as a function of constant magnetic field.

This matrix eigenvalue problem is then solved using library eigenvalue solvers. We use the matlab eig function, using input matrices of size 1200×1200. Matrices of this size stretch the limits of this eigenvalue solver, and we would need to switch to a sparse-matrix method to consider anything larger. As we are interested in the most convectively unstable modes (i.e. those with the largest imaginary component), it would be more efficient to calculate just these eigenfrequencies.

5.5 Results

We begin by using our model to investigate the effects of a magnetic field that is constant throughout the layer. This relationship is shown in Figure 5.1, at horizontal wavenumber $kR = 50$.

For low magnetic fields, the phase speeds are the same as for the non-magnetic case. Between 10^3 G and 10^4 G, modes peak and disappear. The higher-order modes peak at lower field strengths. Modes achieve a maximum phase speed of 60–70 m/s.

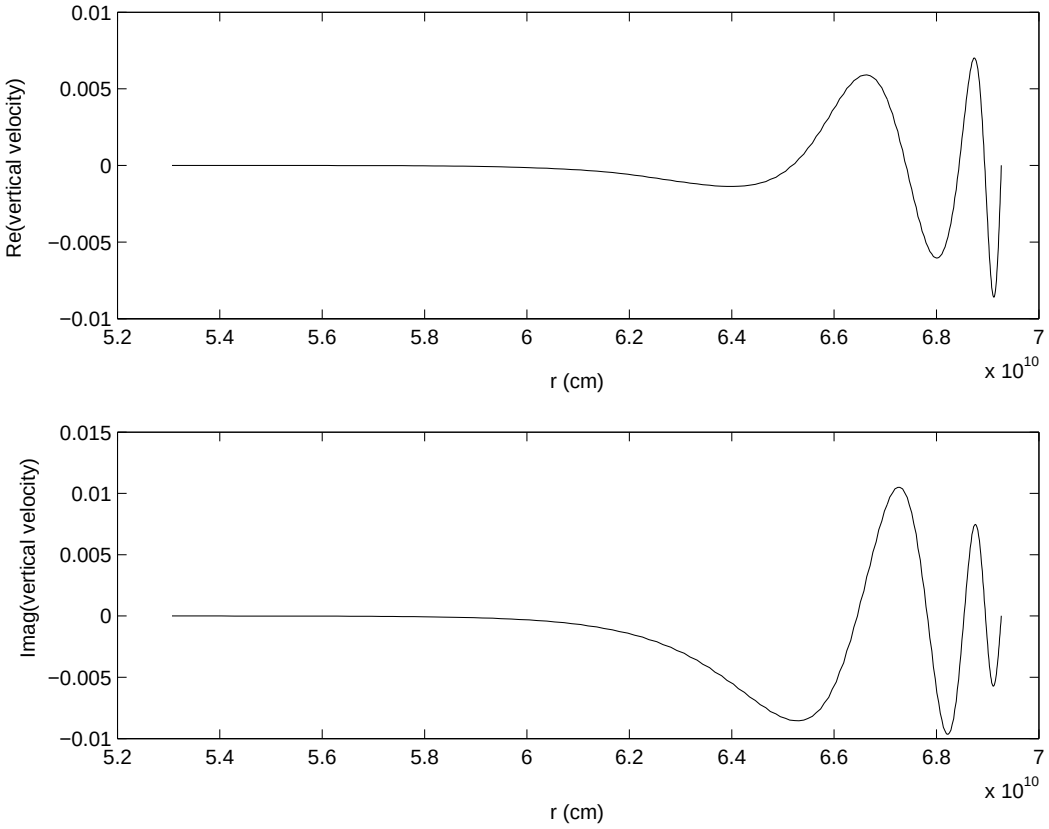

Figure 5.2: Eigenfunction for a convective mode.

The sharp drop in speed at high fields signifies a change in the type of mode. When the field is high enough, we no longer obtain convective modes. This difference can be seen in the eigenfunctions associated with the modes.

As we can see in Figure 5.2, the eigenfunctions for convective modes have big peaks near the surface, and quickly decay to zero deeper in the layer. The non-convective modes obtained at high magnetic fields (Figure 5.3) are small near the surface and have big peaks deeper in the layer.

A field of 10^3 G is in the range where convective modes are obtained, yet they have substantially higher wavespeeds than the non-magnetic case. Figure 5.4 shows the phase speeds for this field, as a function of horizontal wavenumber. Phase speeds near the observed 65 m/s are obtained in this case.

Although 10^3 G is a typical magnetic field strength in sunspots, it is a bit too strong for the solar surface. Thus we also consider the case in which there is a magnetic layer of strength 10^3 G below the surface, at a depth interval of 5–15 Mm, and no magnetic field in the top 2 Mm.

We initially model this case with a simple square wave: the magnetic field is 10^3 G at

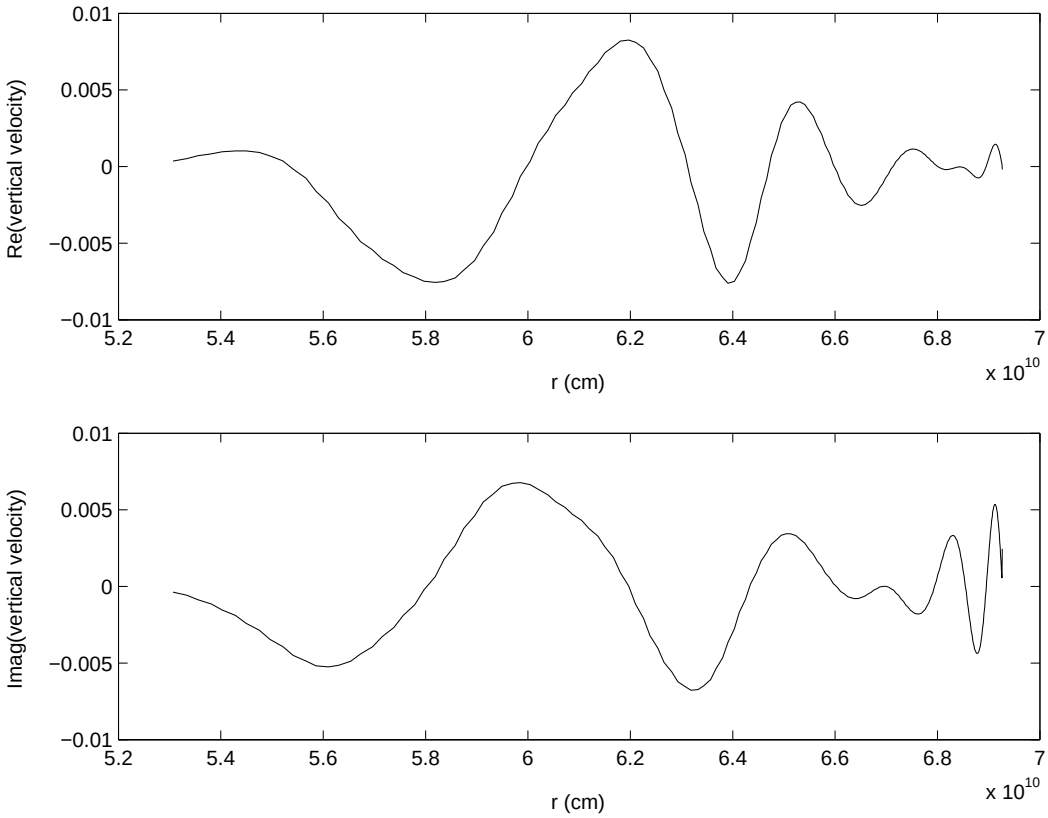

Figure 5.3: Eigenfunction for a non-convective mode obtained with high magnetic field.

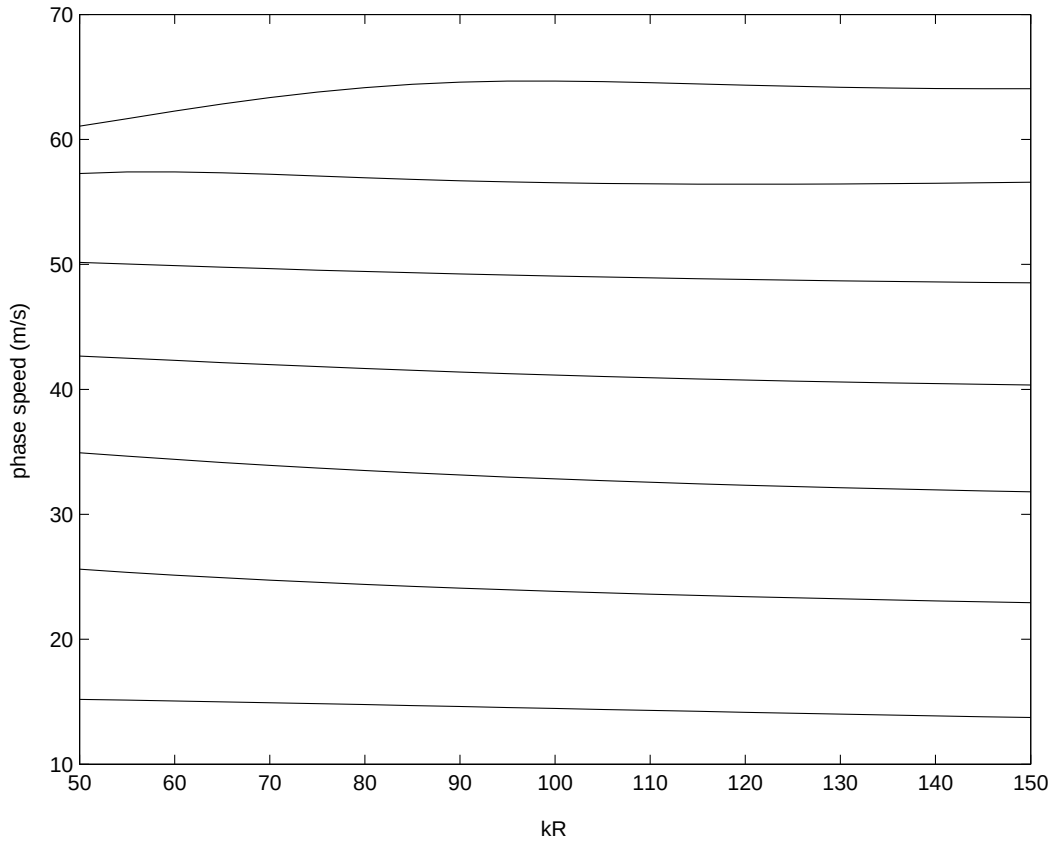

Figure 5.4: Phasespeeds for convective modes with a constant field of 10^3 G.

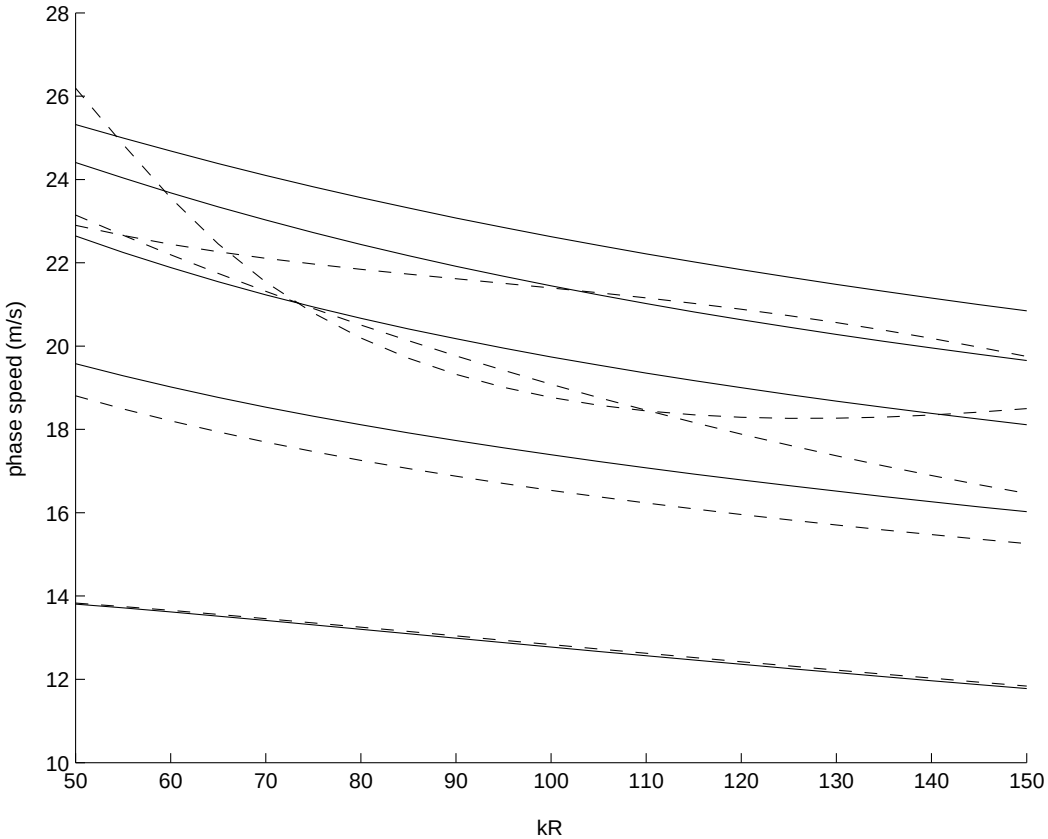

Figure 5.5: Phase speeds for convective modes with a constant magnetic layer of strength 10^3 G at the depth interval 5–15 Mm (dashed), compared to phase speeds in the non-magnetic case (solid).

depths 5–15 Mm and zero everywhere else. As we can see from the results in Figure 5.5, the first mode is virtually unchanged from the non-magnetic case, but the phase speeds of the higher-order modes actually decrease. The modes also start crossing after the third mode. Extending the magnetic layer to the depth interval 2–15 Mm increases the modes slightly except for the first mode, which decreases; however, the speeds are all still lower than in the non-magnetic case.

If we allow the constant magnetic field to extend throughout the region, keeping only the zero field for the top 2 Mm, we obtain modes that have the same shapes as in the case of the magnetic layer. The phase speeds are slightly lower after the second mode. This suggests that we should consider the opposite case: a constant field of 10^3 G until a depth of 2 Mm, and zero field below. In this case we obtain slower modes than in the case of a constant 10^3 G magnetic field throughout the region, but faster than the non-magnetic case. As the mode number increases, so does the gap between the modes and their counterparts in the constant field case.

In order to verify that the behaviour is not due to the discontinuities in our chosen magnetic field, we consider the case where the field is zero above 2 Mm, 10^3 G below 5 Mm and linear between 2 Mm and 5 Mm. This case still produces modes with lower phase speeds than the non-magnetic case.

5.6 Conclusions

While our original linear model produced wave-like convective modes in the presence of a shear gradient, their speed was slower than the observed supergranular waves. This could possibly be due to their being artificially constrained near the surface of the layer by the simplifications of our model. We find that the addition of sufficiently high turbulent viscosity can result in convective modes with phase speeds matching observations. The original model had also neglected the magnetic field, and we use a linear MHD model to investigate its effects.

Similarly to the viscous model, the addition of a sufficiently large magnetic field produces travelling convective modes that penetrate deeper into the layer than in the original model, and thus have higher phase speeds. And, again, if the magnetic field is too large, the unstable convective modes are no longer produced. To obtain an increase in phase speed, we appear to need a magnetic field at the surface of the Sun. The observed speed can be reproduced by a constant magnetic field of the order of 10^3 G throughout the convective zone. This is a bit larger than the fields found at the surface of the Sun. Thus, while the magnetic field contributes substantially to the speed of the convective waves, it most likely does not entirely account for the observations.

Chapter 6

Viscosity and Magnetic Field

6.1 Introduction

We have already considered the effects of viscosity and magnetic field on the convective waves produced in the presence of a shear gradient. Either one of these can reproduce the observed phase speed, for some choice of their value. However, before being confident that the observations can be explained, we should investigate any possible interaction of these two effects. After all, there is no particular reason to believe that only one of these effects would be present. And if their behaviours counteract each other, then we may not have an explanation after all.

6.2 Combined Models

Luckily, it is a pretty easy task to combine our two previous models, into a single model that incorporates the effects of both viscosity and magnetic field.

We begin with a system of two-dimensional linear PDEs:

$$\frac{d\rho_1}{dt} + \rho_0 \nabla \cdot \mathbf{v}_1 + v_{1z}\frac{d\rho_0}{dz} = 0, \tag{6.1}$$

$$\rho_0 \frac{dv_{1x}}{dt} + \rho_0 \frac{dU_0}{dz} v_{1z} = -\frac{\partial p_1}{\partial x} + \frac{dB_0}{dz} b_{1z} + \mu \left(\frac{\partial^2 v_{1x}}{\partial x^2} + \frac{\partial^2 v_{1x}}{\partial z^2} \right), \tag{6.2}$$

$$\rho_0 \frac{dv_{1z}}{dt} = -\frac{\partial p_1}{\partial z} + B_0 \left(\frac{\partial b_{1x}}{\partial x} - \frac{\partial b_{1x}}{\partial z} \right) - \frac{dB_0}{dz} b_{1x} - \rho_1 g + \mu \left(\frac{\partial^2 v_{1z}}{\partial x^2} + \frac{\partial^2 v_{1z}}{\partial z^2} \right), \tag{6.3}$$

$$\frac{dp_1}{dt} + \frac{dB_0}{dz} v_{1z} = c_0^2 \left(\frac{d\rho_1}{dt} + \frac{d\rho_0}{dz} v_{1z} \right), \tag{6.4}$$

$$\frac{db_{1x}}{dt} + \frac{dB_0}{dz} v_{1z} = B_0 \frac{\partial v_{1x}}{\partial x} + \frac{dU_0}{dz} b_{1z} - B_0 \nabla \cdot \mathbf{v}_1, \tag{6.5}$$

$$\frac{db_{1z}}{dt} = B_0 \frac{\partial v_{1z}}{\partial x}. \tag{6.6}$$

These are clearly our MHD equations with added viscous terms. As in both our magnetic and viscous models, we consider wave solutions of the form $\rho_1 = \rho(z)e^{\imath(kx-\omega t)}$, etc. This results in a system of one-dimensional linear equations, depending on wavenumber k and frequency ω:

$$(-\imath\omega + \imath kU_0)\rho(z) + \rho_0[\imath ku(z) + v'(z)] + \frac{d\rho_0}{dz}v(z) = 0, \quad (6.7)$$

$$\rho_0(-\imath\omega + \imath kU_0)u(z) + \rho_0\frac{dU_0}{dz}v(z) = -\imath kp(z) + \frac{dB_0}{dz}b_z(z) + \mu\left[-k^2u(z) + u''(z)\right], \quad (6.8)$$

$$\begin{aligned}\rho_0(-\imath\omega + \imath kU_0)v(z) = -p'(z)+ \\ B_0(\imath kb_z(z) - b_x'(z)) - \frac{dB_0}{dz}b_x(z) - g\rho(z)\mu\left[-k^2v(z) + v''(z)\right],\end{aligned} \quad (6.9)$$

$$\begin{aligned}(-\imath\omega + \imath kU_0)p(z) + \left(-B_0\frac{dB_0}{dz} - \rho_0 g\right)v(z) = \\ c_0^2\left((-\imath\omega + \imath kU_0)\rho(z) + \frac{d\rho_0}{dz}v(z)\right),\end{aligned} \quad (6.10)$$

$$\begin{aligned}(-\imath\omega + \imath kU_0)b_x(z) + \frac{dB_0}{dz}v(z) = B_0\imath ku(z)+ \\ \frac{dU_0}{dz}b_z(z) - B_0(\imath ku(z) + v'(z)),\end{aligned} \quad (6.11)$$

$$(-\imath\omega + \imath kU_0)b_z(z) = \imath kB_0v(z). \quad (6.12)$$

As always, we apply a finite-difference scheme to our system of second-order differential equations, and obtain a matrix eigenvalue problem in ω, which is then solved using library methods.

We discretize z such that $z_0 = r_0$, where r_0 is the chosen lower boundary, and $z_N = R$, where R is the solar radius. We then have interior points z_j for $j = 1 \ldots N-1$. We define $v_j \approx v(z_j)$. Our first boundary condition, zero vertical velocity at the top and bottom of the layer, then becomes $v_0 = 0$ and $v_N = 0$. The viscous terms require additional boundary conditions, which, as in the viscous model, we take to be $u'(z_0) = 0$ and $u'(z_N) = 0$. This can be satisfied by considering u to be on a mesh off-set from that for v, and defining $u_j \approx u(z_{j-\frac{1}{2}})$. Then, by defining a "ghost point" across the boundary, we obtain

$$u'(z_0) \approx \frac{u(z_{\frac{1}{2}}) - u(z_{-\frac{1}{2}})}{r_{\frac{1}{2}} - r_{-\frac{1}{2}}} = 0.$$

This produces a condition on $z_{-\frac{1}{2}}$, our ghost point: $u(z_{-\frac{1}{2}}) = u(z_{\frac{1}{2}})$. Or, for our discretized

variables, $u_0 = u_1$. Similarly, from $u'(R) = 0$ we get $u_{N+1} = u_N$. Because we have no boundary conditions for ρ, p, b_x or b_z we consider them on the same offset grid as u.

We apply central differencing to obtain first derivatives on the two meshes:

$$\begin{aligned} v'(z_{j-\frac{1}{2}}) &\approx \frac{v_j - v_{j-1}}{z_j - z_{j-1}}, \\ p'(z_j) &\approx \frac{p_{j+1} - p_j}{z_{j+\frac{1}{2}} - z_{j-\frac{1}{2}}}, \\ b_x'(z_j) &\approx \frac{b_{x_{j+1}} - b_{x_j}}{z_{j+\frac{1}{2}} - z_{j-\frac{1}{2}}}. \end{aligned}$$

We apply a second central difference to obtain our second-derivative terms:

$$v''(z_j) \approx \frac{1}{z_{j+\frac{1}{2}} - z_{j-\frac{1}{2}}} \left[\frac{v_{j+1} - v_j}{z_{j+1} - z_j} - \frac{v_j - v_{j-1}}{z_j - z_{j-1}} \right],$$

$$u''(z_{j-\frac{1}{2}}) \approx \frac{1}{z_j - z_{j-1}} \left[\frac{u_{j+1} - u_j}{z_{j+\frac{1}{2}} - z_{j-\frac{1}{2}}} - \frac{u_j - u_{j-1}}{z_{j-\frac{1}{2}} - z_{j-\frac{3}{2}}} \right].$$

The boundary conditions on u_0 and $u_N + 1$ only arise in these second-derivative terms. Thus, we write two special cases:

$$u''(z_{\frac{1}{2}}) \approx \frac{1}{z_1 - z_0} \left[\frac{1}{z_{\frac{3}{2}} - z_{\frac{1}{2}}} u_2 + \frac{-1}{z_{\frac{3}{2}} - r_{\frac{1}{2}}} u_1 \right],$$

$$u''(z_{N-\frac{1}{2}}) \approx \frac{1}{z_N - z_{N-1}} \left[\frac{-1}{z_{N-\frac{1}{2}} - z_{N-\frac{3}{2}}} u_N + \frac{1}{z_{N-\frac{1}{2}} - z_{N-\frac{3}{2}}} u_{N-1} \right].$$

We substitute these into (6.7) – (6.12), and use interpolation to obtain values for the variables on the other offset mesh. Equation (6.9) must be satisfied at z_j for $j = 1, \ldots, N-1$. The remaining equations must be satisfied at $z_{j-\frac{1}{2}}$ for $j = 1 \ldots N$. Thus we have a linear system:

$$\begin{aligned} &(-\imath\omega + \imath k U_0)\, \rho_j + \imath k \rho_0 u_j \\ &\quad + \left[\left(\frac{1}{2} \frac{d\rho_0}{dz} - \frac{\rho_0}{r_j - r_{j-1}} \right) v_{j-1} + \left(\frac{1}{2} \frac{d\rho_0}{dz} + \frac{\rho_0}{r_j - r_{j-1}} \right) v_j \right] = 0, \end{aligned} \tag{6.13}$$

$$\begin{aligned} &\frac{-\mu}{(z_j - z_{j-1}) \left(z_{j+\frac{1}{2}} - z_{j-\frac{1}{2}} \right)} u_{j+1} + \frac{-\mu}{(z_j - z_{j-1}) \left(z_{j-\frac{1}{2}} - z_{j-\frac{3}{2}} \right)} u_{j-1} \\ &\quad + \left(\rho_0 (-\imath\omega + \imath k U_0) + \mu k^2 + \frac{\mu}{z_j - z_{j-1}} \left(\frac{1}{z_{j+\frac{1}{2}} - z_{j-\frac{1}{2}}} + \frac{1}{z_{j-\frac{1}{2}} - z_{j-\frac{3}{2}}} \right) \right) u_j \\ &\quad + \left[\frac{1}{2} \rho_0 \frac{dU_0}{dz} v_j + \frac{1}{2} \rho_0 \frac{dU_0}{dz} v_{j-1} \right] + \imath k p_j - \frac{dB_0}{dz} b_{z_j} = 0, \end{aligned} \tag{6.14}$$

$$
\begin{aligned}
&\frac{-\mu}{\left(z_{j+\frac{1}{2}}-z_{j-\frac{1}{2}}\right)(z_j-z_{j-1})}v_{j-1}+\frac{-\mu}{\left(z_{j+\frac{1}{2}}-z_{j-\frac{1}{2}}\right)(z_{j+1}-z_j)}v_{j+1}\\
&\quad+\left(\rho_0\left(-\imath\omega+\imath kU_0\right)+\mu k^2+\frac{\mu}{z_{j+\frac{1}{2}}-z_{j-\frac{1}{2}}}\left(\frac{1}{z_{j+1}-z_j}+\frac{1}{z_j-z_{j-1}}\right)\right)v_j\\
&\quad+\left[\frac{1}{2}g\rho_j+\frac{1}{2}g\rho_{j+1}\right]+\left[\frac{1}{z_{j+\frac{1}{2}}-z_{j-\frac{1}{2}}}p_{j+1}+\frac{-1}{z_{j+\frac{1}{2}}-z_{j-\frac{1}{2}}}p_j\right]\\
&\quad+\left[\left(\frac{1}{2}\frac{dB_0}{dz}-\frac{B_0}{r_{j+\frac{1}{2}}-r_{j-\frac{1}{2}}}\right)b_{x_j}+\left(\frac{1}{2}\frac{dB_0}{dz}+\frac{B_0}{r_{j+\frac{1}{2}}-r_{j-\frac{1}{2}}}\right)b_{x_{j+1}}\right]\\
&\quad+\left[-\frac{1}{2}\imath kB_0b_{z_j}-\frac{1}{2}\imath kB_0b_{z_{j+1}}\right]=0, \qquad (6.15)\\
&\left[-\frac{1}{2}\left(B_0\frac{dB_0}{dz}+\rho_0gc_0^2\frac{d\rho_0}{dz}\right)v_{j-1}-\frac{1}{2}\left(B_0\frac{dB_0}{dz}+\rho_0g+c_0^2\frac{d\rho_0}{dz}\right)v_j\right]\\
&\quad-c_0^2\left(-\imath\omega+\imath kU_0\right)\rho_j+\left(-\imath\omega+\imath kU_0\right)p_j=0, \qquad (6.16)\\
&\left[\left(\frac{1}{2}\frac{dB_0}{dz}-\frac{B_0}{r_j-r_{j-1}}\right)v_{j-1}+\left(\frac{1}{2}\frac{dB_0}{dz}+\frac{B_0}{r_j-r_{j-1}}\right)v_j\right]\\
&\quad+\left(-\imath\omega+\imath kU_0\right)b_{x_j}-\frac{dU_0}{dz}b_{x_j}=0, \qquad (6.17)\\
&\left[-\frac{1}{2}\imath kB_0v_{j-1}-\frac{1}{2}\imath kB_0v_j\right]+\left(-\imath\omega+\imath kU_0\right)b_{z_j}=0. \qquad (6.18)
\end{aligned}
$$

As (6.15) must hold at $N-1$ points, and the others hold at N points, we can write these equations in matrix form. If we define vectors

$$
\vec{\rho}=\begin{bmatrix}\rho_1\\ \vdots\\ \rho_N\end{bmatrix},\quad \vec{u}=\begin{bmatrix}u_1\\ \vdots\\ u_N\end{bmatrix},\quad \vec{v}=\begin{bmatrix}v_1\\ \vdots\\ v_{N-1}\end{bmatrix},
$$

$$
\vec{p}=\begin{bmatrix}p_1\\ \vdots\\ p_N\end{bmatrix},\quad \vec{b_x}=\begin{bmatrix}b_{x_1}\\ \vdots\\ b_{x_N}\end{bmatrix},\quad \vec{b_z}=\begin{bmatrix}b_{z_1}\\ \vdots\\ b_{z_N}\end{bmatrix},
$$

we can write a system of matrix equations that appears identical to those for our magnetic model. In this case, however, the matrices are definied differently, according to (6.13) – (6.18), which become

$$
\begin{aligned}
A\vec{\rho}+B\vec{u}+C\vec{v}&=0, && (6.19)\\
D\vec{u}+E\vec{v}+F\vec{p}+G\vec{b_x}&=0, && (6.20)\\
H\vec{\rho}+I\vec{v}+J\vec{p}+K\vec{b_x}+L\vec{b_z}&=0, && (6.21)\\
M\vec{\rho}+\mathcal{N}\vec{v}+\mathcal{O}\vec{p}&=0, && (6.22)\\
P\vec{v}+Q\vec{b_x}+R\vec{b_z}&=0, && (6.23)
\end{aligned}
$$

$$S\vec{v} + T\vec{b_z} = 0. \tag{6.24}$$

The frequency ω appears linearly in matrices A, D, I, M, $\mathcal{O}$, Q, and T ($A = \omega A_1 + A_0$, etc.).

These matrix equations can be combined into block matrices, producing an eigenvalue problem:

$$\omega \begin{bmatrix} A_1 & 0 & 0 & 0 & 0 & 0 \\ 0 & D_1 & 0 & 0 & 0 & 0 \\ 0 & 0 & I_1 & 0 & 0 & 0 \\ M_1 & 0 & 0 & \mathcal{O}_1 & 0 & 0 \\ 0 & 0 & 0 & 0 & Q_1 & 0 \\ 0 & 0 & 0 & 0 & 0 & T_1 \end{bmatrix} \vec{\Phi} + \begin{bmatrix} A_0 & B & C & 0 & 0 & 0 \\ 0 & D_0 & E & F & 0 & G \\ H & 0 & I_0 & J & K & L \\ M_0 & 0 & \mathcal{N} & \mathcal{O}_0 & 0 & 0 \\ 0 & 0 & P & 0 & Q_0 & R \\ 0 & 0 & S & 0 & 0 & T_0 \end{bmatrix} \vec{\Phi} = 0,$$

$$\text{where } \vec{\Phi} = \begin{bmatrix} \vec{\rho} \\ \vec{u} \\ \vec{v} \\ \vec{p} \\ \vec{b_x} \\ \vec{b_z} \end{bmatrix}.$$

This matrix eigenvalue problem is then solved using library eigenvalue solvers, as in the magnetic model.

6.3 Results

We verify the model by comparing the results to our previous models. When viscosity and magnetic field are set to zero, the results match the original linear model. When viscosity or magnetic field is set to zero and the other is constant, the results match the magnetic and viscosity models respectively.

Once satisfied that the model is correct, we consider the case where both viscosity and magnetic field are constant and non-zero. A coefficient of dynamic viscosity of 10^9 g cm^{-1} s^{-1}, combined with a solar shear profile, reproduced the observed phase speeds, as did a constant toroidal magnetic field of 10^3 G. The phase speeds produced for this case are shown in Figure 6.1.

The maximum phase speed attained is no higher than for the cases with just viscosity or magnetic field; however, this maximum is attained at a lower mode number. As the observations are most likely not of a high mode, this is stronger evidence supporting our proposed explanation of supergranular waves.

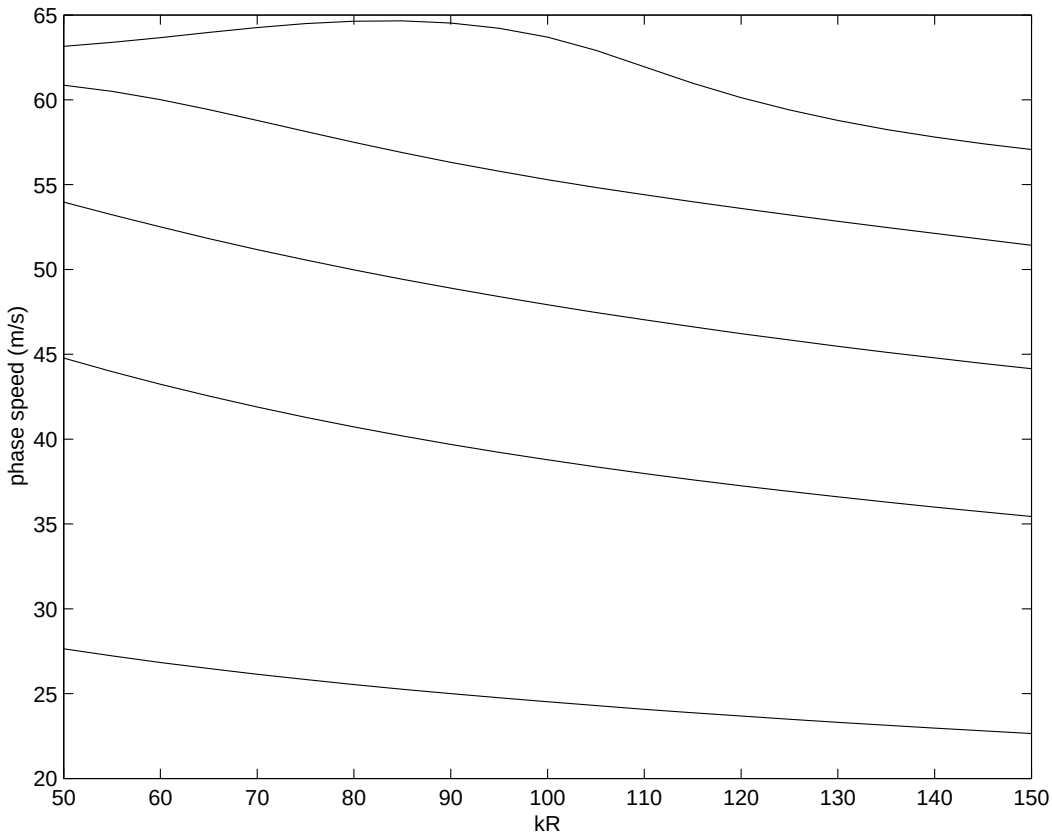

Figure 6.1: Phasespeeds for convective modes with a constant coefficient of dynamic viscosity of 10^9 g cm^{-1} s^{-1} and a constant toroidal magnetic field of 10^3 G.

6.4 Conclusions

Our original model confirmed that the presence of the shear gradient obtained from helioseismology causes unstable convective modes to become running waves; however, the phase speed of these modelled waves is lower than that of the observed supergranular waves. This appears to be due to the modes being constrained near the top of the layer, possibly due to the simplications of the model. We have addressed this with two additional models, which added viscosity and magnetic field respectively to the original. The results from the two cases are similar: the modes extend deeper into the layer and travel faster. In both cases, the observed phase speed can be reproduced for some choice of parameters. A mixing length theory approximation suggests that the required coefficient of dynamic viscosity is reasonable. The required magnetic field is possible in sunspots, but is too large for the quiet Sun.

Although both viscosity and magnetic field modelled independently can reproduce the observed phase speeds, we consider a model that includes both, to be sure that they do not counteract each other. We find that including both effects does not increase the maximum phase speed, but it does cause that maximum to occur at a lower mode number. This strengthens our argument that the observed wavelike behaviour of supergranulation is caused by the shear gradient.

Chapter 7

Three-Dimensional Linear Models

7.1 Introduction

Our previous models were all in two dimensions. We chose this simplification because the shear velocity and the expected travelling waves are both in the x-direction (in our choice of coordinates), while all the parameters vary only with depth (the z-direction). Thus, we neglect the y-direction.

However, this simplification means that essentially we have been considering convective rolls, whereas we wish to model the behaviour of supergranular cells. For non-magnetic cases, the two-dimensional models are equivalent to a three-dimensional model with a wavenumber of zero in the y-direction. The convection rolls can be converted to cells by considering the case in which the x and y wavenumbers are equal.

7.2 Basic Model

We return to our linearized equations of continuity, motion and adiabatic compressibility, (2.1) – (2.6). As in our previous model, we consider wave solutions for all variables; however, we now have three-dimensional waves:

$$\begin{pmatrix} \rho_1 & u_{1x} & u_{1y} & u_{1z} & p_1 \end{pmatrix} = \begin{pmatrix} \rho(z) & u(z) & v(z) & w(z) & p(z) \end{pmatrix} e^{\imath(kx+k_y y-\omega t)}.$$

This reduces our system to the following:

$$(-\imath\omega + \imath k U_0)\,\rho(z) + \rho_0\left[\imath k u(z) + \imath k_y v(z) + w'(z)\right] + \frac{d\rho_0}{dz} w(z) = 0, \tag{7.1}$$

$$\rho_0\,(-\imath\omega + \imath k U_0)\,u(z) + \rho_0 \frac{dU_0}{dz} w(z) = -\imath k p(z), \tag{7.2}$$

$$\rho_0 \left(-\imath\omega + \imath k U_0\right) v(z) = -\imath k_y p(z), \tag{7.3}$$

$$\rho_0 \left(-\imath\omega + \imath k U_0\right) w(z) = -p'(z) - g\rho(z), \tag{7.4}$$

$$\left(-\imath\omega + \imath k U_0\right) p(z) - \rho_0 g w(z) = c_0^2 \left[\left(-\imath\omega + \imath k U_0\right) \rho(z) + \frac{d\rho_0}{dz} w(z)\right]. \tag{7.5}$$

As before, we apply a finite-difference scheme on an offset grid. The boundary condition remains $w(r_0) = 0 = w(R)$. Choosing $N+1$ gridpoints, we consider values of w at the gridpoints and values of ρ, u, v and p at the half gridpoints. We approximate values between the gridpoints using interpolation, and the derivatives with central differences. Substituting these approximations into (7.1) – (7.5):

$$\begin{aligned}\left(-\imath\omega + \imath k U_0\right)\big|_{j-\frac{1}{2}} \rho_{j-\frac{1}{2}} + \rho_0\big|_{j-\frac{1}{2}} \left[\imath k u_{j-\frac{1}{2}} + \imath k_y v_{j-\frac{1}{2}} + \frac{w_j - w_{j-1}}{r_j - r_{j-1}}\right] \\ + \left.\frac{d\rho_0}{dz}\right|_{j-\frac{1}{2}} \frac{w_j + w_{j-1}}{2} = 0,\end{aligned} \tag{7.6}$$

$$\rho_0 \left(-\imath\omega + \imath k U_0\right)\big|_{j-\frac{1}{2}} u_{j-\frac{1}{2}} + \rho_0 \left.\frac{dU_0}{dz}\right|_{j-\frac{1}{2}} \frac{w_j + w_{j-1}}{2} = -\imath k p_{j-\frac{1}{2}}, \tag{7.7}$$

$$\rho_0 \left(-\imath\omega + \imath k U_0\right)\big|_{j-\frac{1}{2}} v_{j-\frac{1}{2}} = -\imath k_y p_{j-\frac{1}{2}}, \tag{7.8}$$

$$\rho_0 \left(-\imath\omega + \imath k U_0\right)\big|_{j} w_j = -\frac{p_{j+\frac{1}{2}} - p_{j-\frac{1}{2}}}{r_{j+\frac{1}{2}} - r_{j-\frac{1}{2}}} - g\big|_j \frac{\rho_{j+\frac{1}{2}} + \rho_{j-\frac{1}{2}}}{2}, \tag{7.9}$$

$$\begin{aligned}\left(-\imath\omega + \imath k U_0\right)\big|_{j-\frac{1}{2}} p_{j-\frac{1}{2}} - \rho_0 g\big|_{j-\frac{1}{2}} \frac{w_j + w_{j-1}}{2} \\ = c_0^2 \left.\left[\left(-\imath\omega + \imath k U_0\right) \rho_{j-\frac{1}{2}} + \frac{d\rho_0}{dz} \frac{w_j + w_{j-1}}{2}\right]\right|_{j-\frac{1}{2}}.\end{aligned} \tag{7.10}$$

These equations can be written in vector form, and ω can be found with a standard matrix eigenvalue algorithm.

We use values for ρ_0, $\frac{d\rho_0}{dz}$, c_0, g and U_0 from helioseismology. When k_y is set to zero, we obtain the same results as in the two-dimensional model, as we would expect. To simulate convective cells, we now consider the case where $k_y = k$.

The phase speed ω/k of the convective cells is shown in Figure 7.1. Switching to convective cells, from rolls, does not substantially change the resulting phase speeds. Some of the modes have slightly reduced speeds; however, more convective modes are obtained, and a maximum phase speed of ~ 26 m/s is still obtained.

7.3 Viscosity

As in the two-dimensional case, we add viscosity by modifying our basic equations (7.1) – (7.5). This is a relatively minor change, consisting of an additional term in each of the three

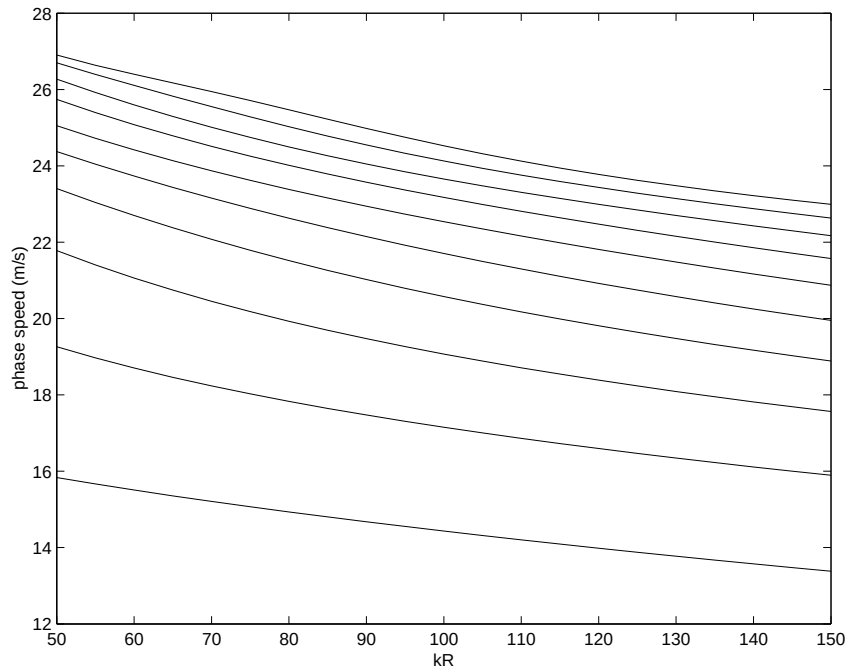

Figure 7.1: The phase speed of the convective cells in the presence of the subsurface shear flow as a function of kR, for the first ten modes.

equations of motion, yielding the following system:

$$(-\imath\omega + \imath kU_0)\,\rho(z) + \rho_0\left[\imath ku(z) + \imath k_y v(z) + w'(z)\right] + \frac{d\rho_0}{dz}w(z) = 0, \tag{7.11}$$

$$\rho_0\,(-\imath\omega + \imath kU_0)\,u(z) + \rho_0\frac{dU_0}{dz}w(z) = -\imath kp(z) + \mu\left[-\left(k^2 + k_y^2\right)u(z) + u''(z)\right], \tag{7.12}$$

$$\rho_0\,(-\imath\omega + \imath kU_0)\,v(z) = -\imath k_y p(z) + \mu\left[-\left(k^2 + k_y^2\right)v(z) + v''(z)\right], \tag{7.13}$$

$$\rho_0\,(-\imath\omega + \imath kU_0)\,w(z) = -p'(z) - g\rho(z) + \mu\left[-\left(k^2 + k_y^2\right)w(z) + w''(z)\right], \tag{7.14}$$

$$(-\imath\omega + \imath kU_0)\,p(z) - \rho_0 g w(z) = c_0^2\left[(-\imath\omega + \imath kU_0)\,\rho(z) + \frac{d\rho_0}{dz}w(z)\right], \tag{7.15}$$

where μ is the coefficient of dynamic viscosity. Because we now have second-order terms, rather than the strictly first-order terms we had before, we now need more boundary conditions. Thus, in addition to $w(r_0) = 0 = w(R)$, we require that $u'(r_0) = 0 = u'(R)$ and $v'(r_0) = 0 = v'(R)$.

We apply the same finite-difference scheme as in the basic model. We apply a second central difference to obtain our new second-derivative terms:

$$u''(z_{j-\frac{1}{2}}) \approx \frac{1}{z_j - z_{j-1}}\left[\frac{u_{j+1} - u_j}{z_{j+\frac{1}{2}} - z_{j-\frac{1}{2}}} - \frac{u_j - u_{j-1}}{z_{j-\frac{1}{2}} - z_{j-\frac{3}{2}}}\right],$$

$$w''(z_j) \approx \frac{1}{z_{j+\frac{1}{2}} - z_{j-\frac{1}{2}}} \left[\frac{w_{j+1} - w_j}{z_{j+1} - z_j} - \frac{w_j - w_{j-1}}{z_j - z_{j-1}} \right].$$

The boundary conditions on u_0 and u_{N+1} only arise in these second-derivative terms. Thus, we write two special cases:

$$u''(z_{\frac{1}{2}}) \approx \frac{1}{z_1 - z_0} \left[\frac{1}{z_{\frac{3}{2}} - z_{\frac{1}{2}}} u_2 + \frac{-1}{z_{\frac{3}{2}} - r_{\frac{1}{2}}} u_1 \right],$$

$$u''(z_{N-\frac{1}{2}}) \approx \frac{1}{z_N - z_{N-1}} \left[\frac{-1}{z_{N-\frac{1}{2}} - z_{N-\frac{3}{2}}} u_N + \frac{1}{z_{N-\frac{1}{2}} - z_{N-\frac{3}{2}}} u_{N-1} \right].$$

The second-derivative approximation for v is defined identically to that for u listed above.

We substitute these into (7.11) – (7.15) and use interpolation to obtain values for the variables on the other offset mesh. Equation 7.14 must be satisfied at z_j for $j = 1 \ldots N-1$. The remaining equations must be satisfied at $z_{j-\frac{1}{2}}$ for $j = 1 \ldots N$. Thus we have a linear system:

$$\begin{aligned}
(-\imath\omega + \imath k U_0)|_{j-\frac{1}{2}} \rho_{j-\frac{1}{2}} + \rho_0|_{j-\frac{1}{2}} \left[\imath k u_{j-\frac{1}{2}} + \imath k_y v_{j-\frac{1}{2}} + \frac{w_j - w_{j-1}}{r_j - r_{j-1}} \right] \\
+ \left. \frac{d\rho_0}{dz} \right|_{j-\frac{1}{2}} \frac{w_j + w_{j-1}}{2} = 0, \quad (7.16)
\end{aligned}$$

$$\begin{aligned}
\rho_0 (-\imath\omega + \imath k U_0)|_{j-\frac{1}{2}} u_{j-\frac{1}{2}} + \rho_0 \left. \frac{dU_0}{dz} \right|_{j-\frac{1}{2}} \frac{w_j + w_{j-1}}{2} = -\imath k p_{j-\frac{1}{2}} - \mu \left(k^2 + k_y^2\right) u_{j-\frac{1}{2}} \\
+ \frac{\mu}{z_j - z_{j-1}} \left[\frac{u_{j+1} - u_j}{z_{j+\frac{1}{2}} - z_{j-\frac{1}{2}}} - \frac{u_j - u_{j-1}}{z_{j-\frac{1}{2}} - z_{j-\frac{3}{2}}} \right], \quad (7.17)
\end{aligned}$$

$$\begin{aligned}
\rho_0 (-\imath\omega + \imath k U_0)|_{j-\frac{1}{2}} v_{j-\frac{1}{2}} = -\imath k_y p_{j-\frac{1}{2}} - \mu \left(k^2 + k_y^2\right) v_{j-\frac{1}{2}} \\
+ \frac{\mu}{z_j - z_{j-1}} \left[\frac{v_{j+1} - v_j}{z_{j+\frac{1}{2}} - z_{j-\frac{1}{2}}} - \frac{v_j - v_{j-1}}{z_{j-\frac{1}{2}} - z_{j-\frac{3}{2}}} \right], \quad (7.18)
\end{aligned}$$

$$\begin{aligned}
\rho_0 (-\imath\omega + \imath k U_0)|_j w_j = -\frac{p_{j+\frac{1}{2}} - p_{j-\frac{1}{2}}}{r_{j+\frac{1}{2}} - r_{j-\frac{1}{2}}} - g|_j \frac{\rho_{j+\frac{1}{2}} + \rho_{j-\frac{1}{2}}}{2} - \mu \left(k^2 + k_y^2\right) w_j \\
+ \frac{1}{z_{j+\frac{1}{2}} - z_{j-\frac{1}{2}}} \left[\frac{w_{j+1} - w_j}{z_{j+1} - z_j} - \frac{w_j - w_{j-1}}{z_j - z_{j-1}} \right], \quad (7.19)
\end{aligned}$$

$$\begin{aligned}
(-\imath\omega + \imath k U_0)|_{j-\frac{1}{2}} p_{j-\frac{1}{2}} - \rho_0 g|_{j-\frac{1}{2}} \frac{w_j + w_{j-1}}{2} \\
= c_0^2 \left. \left[(-\imath\omega + \imath k U_0) \rho_{j-\frac{1}{2}} + \frac{d\rho_0}{dz} \frac{w_j + w_{j-1}}{2} \right] \right|_{j-\frac{1}{2}}. \quad (7.20)
\end{aligned}$$

These equations can be written in vector form, and ω can be found with a standard matrix eigenvalue algorithm.

We use values for ρ_0, $\frac{d\rho_0}{dz}$, c_0, g and U_0 from helioseismology. When k_y is set to zero, we obtain the same results as in the two-dimensional model, as we would expect. To simulate

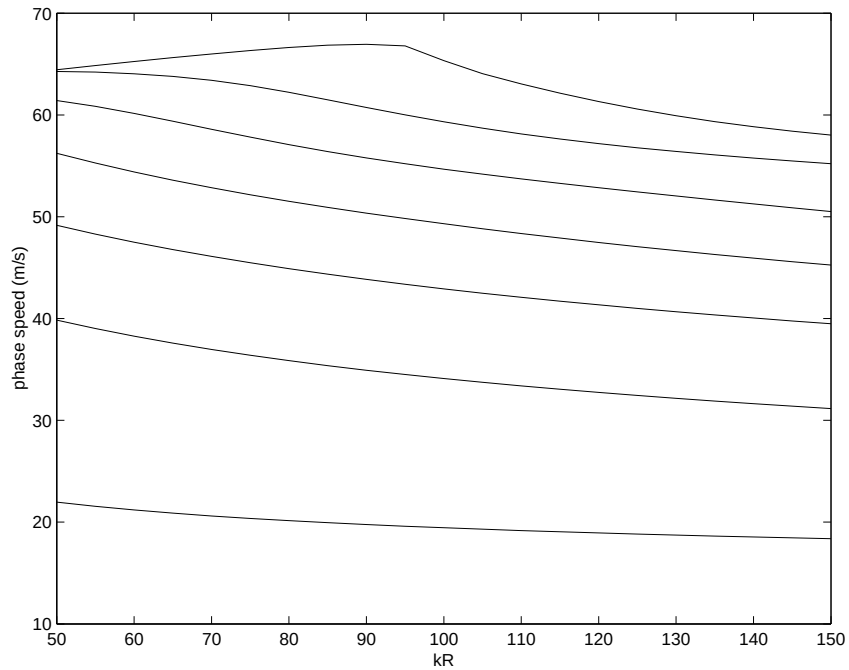

Figure 7.2: The phase speed of the convective cells in the presence of the subsurface shear flow as a function of kR, for the first ten modes, with a constant coefficient of dynamic viscosity of 10^9 g cm^{-1} s^{-1}.

convective cells, we now consider the case where $k_y = k$.

The phase speed ω/k of the convective cells is shown in Figure 7.2. Switching to convective cells, from rolls, does not substantially change the resulting phase speeds. As with the non-viscous case, some of the modes have slightly reduced speeds; however, more convective modes are obtained, and a maximum phase speed of ~ 65 m/s is still obtained.

7.4 Magnetic Field

Unlike the basic and viscosity models, the three-dimensional magnetic field model is more complicated than simply adding variables and equations. We must return to our MHD equations:

$$\frac{\partial \rho}{\partial t} + \nabla \cdot (\rho \mathbf{v}) = 0, \tag{7.21}$$

$$\rho \frac{\partial \mathbf{v}}{\partial t} + \rho(\mathbf{v} \cdot \nabla)\mathbf{v} = -\nabla p - \frac{1}{2}\nabla(\mathbf{B} \cdot \mathbf{B}) + \mathbf{B} \cdot \nabla \mathbf{B} + \rho \mathbf{g}, \tag{7.22}$$

$$\frac{\partial p}{\partial t} + \mathbf{v} \cdot \nabla p = -\gamma p \nabla \cdot \mathbf{v}, \tag{7.23}$$

$$\nabla \cdot \mathbf{B} = 0, \tag{7.24}$$

$$\frac{\partial \mathbf{B}}{\partial t} = (\mathbf{B}\cdot\nabla)\mathbf{v} - (\mathbf{v}\cdot\nabla)\mathbf{B} + \mathbf{v}(\nabla\cdot\mathbf{B}) - \mathbf{B}(\nabla\cdot\mathbf{v}). \tag{7.25}$$

We reconsider our linear perturbations, $\rho = \rho_0(z) + \rho_1(x,y,z,t)$, $\mathbf{v} = \mathbf{v}_0(z) + \mathbf{v}_1(x,y,z,t)$, $p = p_0(z) + p_1(x,y,z,t)$, and $\mathbf{B} = \mathbf{B}_0(z) + \mathbf{B}_1(x,y,z,t)$.

We investigate the effect of shear flow and a toroidal magnetic field by taking unperturbed flows and fields of $\mathbf{v}_0 = (U_0(z), 0, 0)$ and $\mathbf{B}_0 = (0, B_0(z), 0)$. The corresponding perturbations are $\mathbf{v}_1 = (v_{1x}, v_{1y}, v_{1z})$ and $\mathbf{B}_1 = (b_{1x}, b_{1y}, b_{1z})$.

By substituting into the MHD equations and keeping only the first-order terms in the perturbation variables, we obtain a set of linear equations:

$$\frac{d\rho_1}{dt} + \rho_0\nabla\cdot\mathbf{v}_1 + v_{1z}\frac{d\rho_0}{dz} = 0, \tag{7.26}$$

$$\rho_0\frac{dv_{1x}}{dt} + \rho_0\frac{dU_0}{dz}v_{1z} = -\frac{\partial p_1}{\partial x} + B_0\left(\frac{\partial b_{1x}}{\partial y} - \frac{\partial b_{1y}}{\partial x}\right), \tag{7.27}$$

$$\rho_0\frac{dv_{1y}}{dt} = -\frac{\partial p_1}{\partial y} + \frac{dB_0}{dz}b_{1z}, \tag{7.28}$$

$$\rho_0\frac{dv_{1z}}{dt} = -\frac{\partial p_1}{\partial z} + B_0\left(\frac{\partial b_{1z}}{\partial y} - \frac{\partial b_{1y}}{\partial z}\right) - \frac{dB_0}{dz}b_{1y} - g\rho_1, \tag{7.29}$$

$$\frac{dp_1}{dt} + \frac{dp_0}{dz}v_{1z} = c_0^2\left(\frac{d\rho_1}{dt} + \frac{d\rho_0}{dz}v_{1z}\right), \tag{7.30}$$

$$\frac{db_{1x}}{dt} = B_0\frac{\partial v_{1x}}{\partial y} + \frac{dU_0}{dz}b_{1z}, \tag{7.31}$$

$$\frac{db_{1y}}{dt} = -B_0\left(\frac{\partial v_{1x}}{\partial x} + \frac{\partial v_{1z}}{\partial z}\right) - \frac{dB_0}{dz}v_{1z}, \tag{7.32}$$

$$\frac{db_{1z}}{dt} = B_0\frac{\partial v_{1z}}{\partial y}. \tag{7.33}$$

We now consider wave solutions for all variables:

$$\begin{pmatrix} \rho_1 & u_{1x} & u_{1y} & u_{1z} & p_1 & b_{1x} & b_{1y} & b_{1z} \end{pmatrix} =$$
$$\begin{pmatrix} \rho(z) & u(z) & v(z) & w(z) & p(z) & b_x(z) & b_y(z) & b_z(z) \end{pmatrix} e^{\imath(kx+k_y y-\omega t)}.$$

This reduces our system to the following:

$$(-\imath\omega + \imath kU_0)\,\rho(z) + \rho_0\left[\imath ku(z) + \imath k_y v(z) + w'(z)\right] + \frac{d\rho_0}{dz}w(z) = 0, \tag{7.34}$$

$$\rho_0\left(-\imath\omega + \imath kU_0\right)u(z) + \rho_0\frac{dU_0}{dz}w(z) = -\imath kp(z) + B_0\left(\imath k_y b_x(z) - \imath k b_y(z)\right), \tag{7.35}$$

$$\rho_0\left(-\imath\omega + \imath kU_0\right)v(z) = -\imath k_y p(z) + \frac{dB_0}{dz}b_z(z), \tag{7.36}$$

$$\rho_0\left(-\imath\omega + \imath kU_0\right)w(z) = -p'(z) + B_0\left(\imath k_y b_z(z) - b_y'(z)\right) - \frac{dB_0}{dz}b_y(z) - g\rho(z), \tag{7.37}$$

$$(-\imath\omega + \imath kU_0)\,p(z) + \left(-B_0\frac{dB_0}{dz} - \rho_0 g\right)w(z) =$$

$$c_0^2\left((-\imath\omega+\imath kU_0)\,\rho(z)+\frac{d\rho_0}{dz}w(z)\right), \tag{7.38}$$

$$(-\imath\omega+\imath kU_0)\,b_x(z)=\imath k_yB_0u(z)+\frac{dU_0}{dz}b_z(z), \tag{7.39}$$

$$(-\imath\omega+\imath kU_0)\,b_y(z)=-B_0\left(\imath ku(z)+w'(z)\right)-\frac{dB_0}{dz}w(z), \tag{7.40}$$

$$(-\imath\omega+\imath kU_0)\,b_z(z)=\imath k_yB_0w(z). \tag{7.41}$$

Again, we apply a finite-difference scheme on an offset grid. The boundary condition remains $w(r_0)=0=w(R)$. Choosing $N+1$ gridpoints, we consider values of w at the gridpoints and values of ρ, u, v, p, b_x, b_y and b_z at the half gridpoints. We approximate values between the gridpoints using interpolation, and the derivatives with central differences. Substituting these approximations into (7.34) – (7.41) gives

$$(-\imath\omega+\imath kU_0)|_{j-\frac{1}{2}}\,\rho_{j-\frac{1}{2}}+\rho_0|_{j-\frac{1}{2}}\left[\imath ku_{j-\frac{1}{2}}+\imath k_yv_{j-\frac{1}{2}}+\frac{w_j-w_{j-1}}{r_j-r_{j-1}}\right]+ \frac{d\rho_0}{dz}\bigg|_{j-\frac{1}{2}}\frac{w_j+w_{j-1}}{2}=0, \tag{7.42}$$

$$\rho_0\,(-\imath\omega+\imath kU_0)|_{j-\frac{1}{2}}\,u_{j-\frac{1}{2}}+\rho_0\frac{dU_0}{dz}\bigg|_{j-\frac{1}{2}}\frac{w_j+w_{j-1}}{2}=-\imath kp_{j-\frac{1}{2}}+ B_0|_{j-\frac{1}{2}}\left(\imath k_yb_{x_{j-\frac{1}{2}}}-\imath kb_{y_{j-\frac{1}{2}}}\right), \tag{7.43}$$

$$\rho_0\,(-\imath\omega+\imath kU_0)|_{j-\frac{1}{2}}\,v_{j-\frac{1}{2}}=-\imath k_yp_{j-\frac{1}{2}}+\frac{dB_0}{dz}\bigg|_{j-\frac{1}{2}}b_{z_{j-\frac{1}{2}}}, \tag{7.44}$$

$$\rho_0\,(-\imath\omega+\imath kU_0)|_j\,w_j=\frac{p_{j+\frac{1}{2}}-p_{j-\frac{1}{2}}}{r_{j+\frac{1}{2}}-r_{j-\frac{1}{2}}}+ B_0|_j\left(\imath k_y\frac{b_{z_{j+\frac{1}{2}}}+b_{z_{j-\frac{1}{2}}}}{2}-\frac{b_{y_{j+\frac{1}{2}}}-b_{y_{j-\frac{1}{2}}}}{r_{j+\frac{1}{2}}-r_{j-\frac{1}{2}}}\right)- \frac{dB_0}{dz}\bigg|_j\frac{b_{y_{j+\frac{1}{2}}}+b_{y_{j-\frac{1}{2}}}}{2}-g|_j\,\frac{\rho_{j+\frac{1}{2}}+\rho_{j-\frac{1}{2}}}{2}, \tag{7.45}$$

$$(-\imath\omega+\imath kU_0)|_{j-\frac{1}{2}}\,p_{j-\frac{1}{2}}+\left(-B_0\frac{dB_0}{dz}-\rho_0\right)\bigg|_{j-\frac{1}{2}}\frac{w_j+w_{j-1}}{2}= c_0^2\left[(-\imath\omega+\imath kU_0)\,\rho_{j-\frac{1}{2}}+\frac{d\rho_0}{dz}\frac{w_j+w_{j-1}}{2}\right]\bigg|_{j-\frac{1}{2}}, \tag{7.46}$$

$$(-\imath\omega+\imath kU_0)|_{j-\frac{1}{2}}\,b_{x_{j-\frac{1}{2}}}=\imath k_y\;B_0|_{j-\frac{1}{2}}\,u_{j-\frac{1}{2}}+\frac{dU_0}{dz}\bigg|_{j-\frac{1}{2}}b_{z_{j-\frac{1}{2}}}, \tag{7.47}$$

$$(-\imath\omega+\imath kU_0)|_{j-\frac{1}{2}}\,b_{y_{j-\frac{1}{2}}}=-\,B_0|_{j-\frac{1}{2}}\left(\imath ku_{j-\frac{1}{2}}+\frac{w_j-w_{j-1}}{r_j-r_{j-1}}\right)- \frac{dB_0}{dz}\bigg|_{j-\frac{1}{2}}\frac{w_j+w_{j-1}}{2}, \tag{7.48}$$

$$(-\imath\omega+\imath kU_0)|_{j-\frac{1}{2}}\,b_{z_{j-\frac{1}{2}}}=\imath k_y\;B_0|_{j-\frac{1}{2}}\,\frac{w_j+w_{j-1}}{2}. \tag{7.49}$$

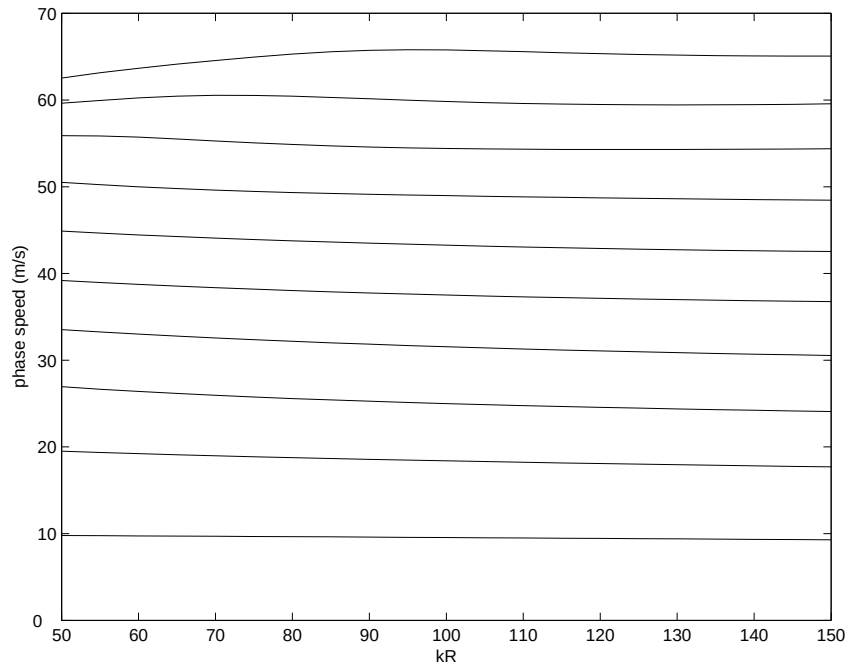

Figure 7.3: The phase speed of the convective cells in the presence of the subsurface shear flow as a function of kR, for the first ten modes, with a constant toroidal magnetic field of 300 G.

As before, these equations can be written in vector form, and ω can be found with a standard matrix eigenvalue algorithm.

We use values for ρ_0, $\frac{d\rho_0}{dz}$, c_0, g and U_0 from helioseismology. When k_y is set to zero, we obtain the same results as in the two-dimensional model, as we would expect. To simulate convective cells, we now consider the case where $k_y = k$.

The phase speed ω/k of the convective cells, is shown in Figure 7.3. Switching to convective cells, from rolls, does not substantially change the resulting phase speeds. As with the non-viscous case, some of the modes have slightly reduced speeds; however, more convective modes are obtained, and a maximum phase speed of ~ 65 m/s is still obtained.

7.5 Conclusions

For simplicity, we had considered only two dimensions for our previous models. In order to determine the phase speed of convective modes in the presence of a shear gradient, we considered a velocity profile oriented in the x-direction and assumed wave solutions in terms of a frequency ω and a single horizontal wavenumber k_x. This is the equivalent of considering solutions for a three-dimensional model with a wavenumber of zero in the y-direction. Despite the fact that we choose a range of k_x equivalent to supergranulation, with $k_y = 0$, we are actually considering convective rolls rather than cells.

In order to better represent supergranulation, we implement three-dimensional versions of our previous models to produce convective cells. Some variation in results is apparent between the two- and three-dimensional models. In all cases, the phase speed of the convective models is slightly reduced; however, more convective modes are obtained. Overall, the same maximum phase speed occurs as for the corresponding two-dimensional models. Thus we find that the observed wavelike behaviour can be reproduced for convective cells as well as convective rolls.

Chapter 8

Rotation

8.1 Introduction

Thus far, we have been considering only one of the proposed explanations for the wave-like behaviour of solar supergranulation: the steep shear gradient at the surface of the Sun. Although our models have reproduced the observations under these conditions, we now also consider another possible explanation. Busse (2004) has suggested that wavelike drift of hexagonal convection cells along with a mean flow can be produced by the effects of the Coriolis force.

Busse considers a horizontal fluid layer heated from below that is rotating about a fixed vertical axis. A weakly nonlinear analysis of the system shows that the rotation causes a loss of reflection symmetry about the vertical plane, which, for large enough rotation, changes the dynamics of convection and produces a wavelike drift of the hexagonal cells and a mean flow. The drift is prograde with rotation when the convection cells have a descending motion at the centre, and retrograde for cells with rising motion in the centre.

Supergranulation consists of horizontal outflows and strong descending flows at the cell boundaries. This suggests that it would fall into the category of a convective cell with a rising motion in the centre, and thus lead to a retrograde drift. However, Busse suggests that it is more important to consider the asymmetry in strength between the regions of rising and descending velocity, and that, given the indications from helioseismology that strong downward plumes can occur in the interior of supergranular cells, supergranulation dynamics might be better associated with a convection cell with a descending motion at the centre.

8.2 ASH Code

Clune et al. (1999) developed the Anelastic Spherical Harmonic (ASH) code, which uses a pseudospectral method with Chebyshev and spherical harmonic basis functions, to solve

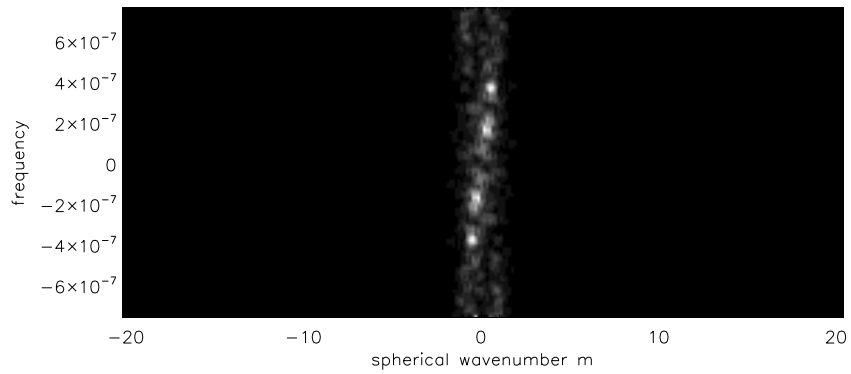

Figure 8.1: Power spectrum of simulated data including solar rotation.

three-dimensional anelastic equations. The anelastic approximation is used because the timescale for large-scale convection is expected to be so much longer than acoustic timescales, making the timesteps for a fully compressible model infeasibly small in comparison to the behaviour they attempt to model.

The anelastic approximation involves separating each of the thermodynamic variables into a spherically symmetric mean and a small perturbation, and neglecting the time derivative in the continuity equation. These approximations are valid when the following conditions hold:

1. The stratification is nearly adiabatic and thus the variations in the thermodynamic quantities due to convection are always small compared to the steady state.

2. The horizontal pressure gradients are the same order of magnitude as the horizontal Reynolds stresses, causing the convective velocities to scale of $\epsilon^{\frac{1}{2}}$, which allows the time derivative to be neglected in the continuity equation. This also implies that the convective motions remain subsonic.

The details of the model can be found in Miesch (1998). Miesch provided some results from an ASH code simulation that included rotation, which we analyze for possible evidence of wave-like behaviour.

8.3 Data Analysis

We constructed time series from the data, and then computed power spectrums. Because of the sampling interval in longitude of the simulation data, we have only spherical wavenumbers in the range $m \in [-20, 20]$. This is smaller than our range of interest for supergranulation, but we can look for trends at the highest available wavenumbers.

The power spectrum (Figure 8.1) seems to include only a ridge around $m = 0$. However, this is because the ridge is so strong as to make the others invisible when plotted together.

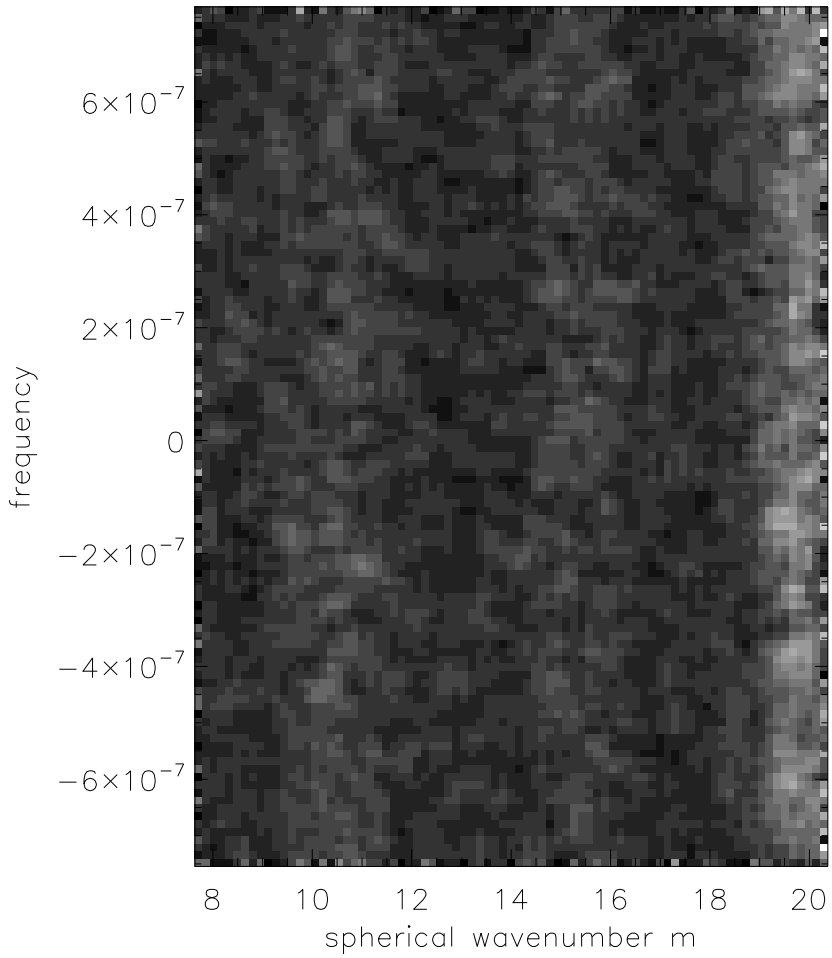

Figure 8.2: Power spectrum of simulated data including solar rotation, with dominant mode removed.

The ridges at higher wavenumbers can be seen in a separate plot (Figure 8.2).

The dominant mode appears to have a finite positive slope, indicating wave behaviour, while the others appear to be vertical, suggesting that they're due to advection.

Of course this could all be due to the resolution of the simulation data. Or, as the power spectrums stop below the wavenumber of supergranulation, the modes in that range may behave differently. So, we cannot claim that the nonlinear effects of the Coriolis force do not play a role in the wave-like behaviour of supergranulation, and thus we investigate further with a linear model including rotation.

8.4 Linear Model

The addition of rotation effects requires only two added terms to the original linearized equations:

$$\frac{d\rho_0}{dt} + \rho_0 \nabla \cdot \mathbf{u} + u_{1z}\frac{d\rho_0}{dz} = 0, \tag{8.1}$$

$$\rho_0 \frac{du_{1x}}{dt} + \rho_0 u_{1z}\frac{dU_0}{dz} = -\frac{\partial p_1}{\partial x}\boxed{-2\Omega\rho_0 u_{1z}}\,, \tag{8.2}$$

$$\rho_0 \frac{du_{1z}}{dt} = -\frac{\partial p_1}{\partial z} - \rho_1 g\boxed{+2\Omega\rho_0 u_{1x}}\,, \tag{8.3}$$

$$\frac{dp_1}{dt} + u_{1z}\frac{dp_0}{dz} = c_0^2\left(\frac{d\rho_1}{dt} + u_{1z}\frac{d\rho_0}{dz}\right), \tag{8.4}$$

where Ω is the rotation rate. The boxed terms add the effect of the Coriolis force. As they include no derivatives, they are easily added to the discretized equations (2.19) – (2.22), which can then be solved as before.

The phase speed of the convective modes obtained with a constant rotation rate of 450 nHz is compared to the original results in Figure 8.3. The addition of rotation effects does cause an increase in phase speed; however, this increase is small. While the phase speed previously had a maximum of 26 m/s, the addition of rotation produces a maximum phase speed of less than 29 m/s. The contribution of the Coriolis force is too small to explain the discrepancy between our model results and observations.

8.5 Conclusions

The subsurface shear gradient is not the only proposed explanation for the observed wave-like behaviour of supergranulation. Busse has suggested the Coriolis force as an alternative explanation. Despite having reproduced the observations in models including the solar shear gradient, we also investigate the effect of the Coriolis force.

Analyzing results from Miesch's three-dimensional nonlinear simulation including the Coriolis force, we find no evidence of wavelike behaviour. As this could possibly be due to the limitations of the simulation data, we also add a Coriolis force term to our original linear model. The addition of the Coriolis force produced by a constant rotation rate of 450 nHz produces only a slight increase in the phase speed. A model including the Coriolis force but no shear gradient produces almost insignificant phase speeds. Thus, we conclude that the Coriolis force is not a significant factor in producing supergranular waves.

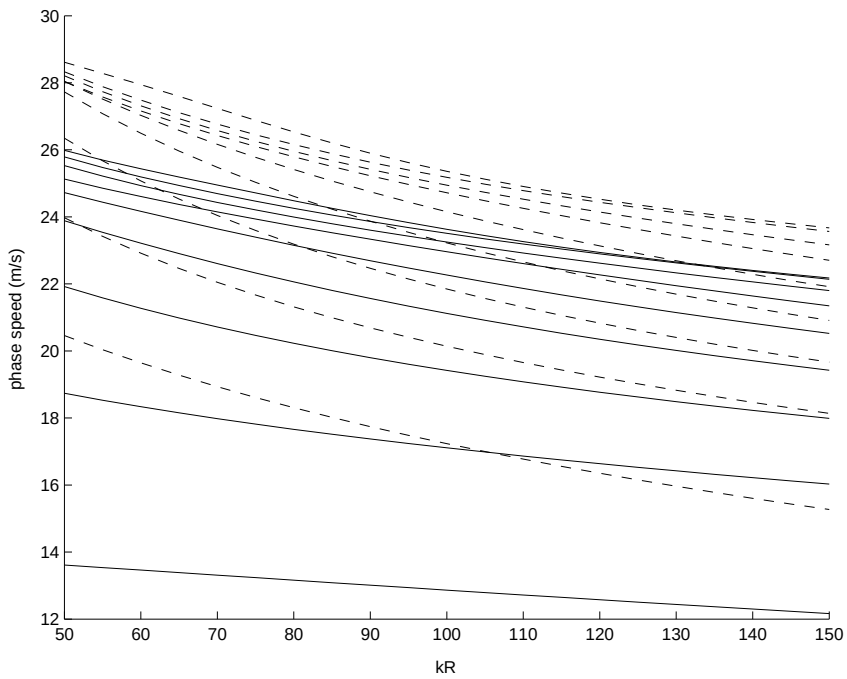

Figure 8.3: The phase speed of the convective modes with rotation (dashed lines) compared to the phase speed of the convective modes without rotation (solid lines) in the presence of the subsurface shear flow as a function of kR.

Chapter 9

Nonlinear Effects

9.1 Introduction

Though we have considered a variety of models so far, they all have one thing in common: they are all based on linearized hydrodynamic or magnetohydronamic equations. However, fluids are not limited to linear behaviour, and by restricting ourselves to these models, we may be neglecting the contribution of nonlinear effects.

Obviously a nonlinear model is harder to work with, or there would be no need for linear models. Specifically, for our problem, we are no longer able to separate out the frequencies to calculate them directly. Furthermore, as we are no longer considering perturbations to a steady-state, it will not be possible simply to input data obtained from helioseismology to describe the solar model. We have to consider an analytical model, such as a polytrope, and compute a time evolution, from which we should be able to observe travelling waves once convective instability sets in.

There are various possible approaches to modelling astrophysical hydrodynamics. Some codes use artificial viscosity for stability and shock capturing. An example of this approach is the ZEUS code, which is based on an operator-split method with second-order finite differences on a staggered mesh. Turbulence research often uses spectral methods, which have high accuracy and are well suited to modelling incompressible flows. Compressible flows can also be modelled with spectral methods, or high-order finite-difference methods. A particular variety of these, called compact methods, have a smaller truncation error than for explicit schemes of the same order. Compact methods have been used to simulate solar convection (Stein & Norlund 1989, 1998) and convective dynamos (Norlund *et al.* 1996b), among other things.

We choose to use the Pencil Code for our problem. It uses sixth-order explicit finite differences and third-order Runge-Kutta timestepping. It applies a non-conservative scheme, allowing the uses of logarithmic variables: this allows a much larger dynamical range in

density and temperature, as required in astrophysical simulations. When solving a non-conservative scheme, we can use the conservation properties to verify the accuracy of the solution.

9.2 Pencil Code

The Pencil Code solves the non-conservative Navier-Stokes equations (or the MHD equations, when applied to magnetic problems). The equations are rewritten in terms of entropy and either logarithmic density or potential enthalpy.

The continuity equation

$$\frac{\partial \rho}{\partial t} = -\nabla \cdot (\rho u)$$

can be written in terms of $\ln \rho$:

$$\frac{D \ln \rho}{Dt} = -\nabla \cdot \mathbf{u}, \tag{9.1}$$

where $D/Dt \equiv \partial/\partial t + \mathbf{u} \cdot \nabla$ is the advective derivative.

The equation of motion can be written as

$$\rho \frac{Du}{Dt} = -\nabla p - \rho \nabla \Phi + F + \nabla \cdot \tau,$$

where p is the pressure, Φ is the gravitational potential, F is a body force, and τ is the stress tensor. The pressure term can be expressed through the relation

$$-\rho^{-1} \nabla p = -c_s^2 \left(\nabla s / c_p + \nabla \ln \rho \right),$$

where the adiabatic sound speed c_s is given by

$$c_s^2 = \gamma \frac{p}{\rho} = c_{s0}^2 \exp \left[\gamma \frac{s}{c_p} + (\gamma - 1) \ln \frac{\rho}{\rho_0} \right],$$

where $c_{s0}^2 = \gamma p_0 / \rho_0$ and the adiabatic index is $\gamma = c_p / c_v$, where c_p and c_v are the specific heats.

The equation of motion is then

$$\frac{Du}{Dt} = -c_s^2 \left(\nabla \frac{s}{c_p} + \nabla \ln \rho \right) - \nabla \Phi + f + \frac{1}{\rho} \nabla \cdot (2 \nu \rho \mathbf{S}), \tag{9.2}$$

where $f = F/\rho$ is the body force per unit mass, ν is the kinematic viscosity, and $\mathbf{S}$ is the strain tensor with components

$$S_{ij} = \frac{1}{2} \left(\frac{\partial u_i}{\partial x_j} + \frac{\partial u_j}{\partial x_i} - \frac{2}{3} \delta_{ij} \nabla \cdot \mathbf{u} \right).$$

The third of the three main equations solved by the Pencil Code is the entropy equation:

$$T\frac{Ds}{Dt} = 2\nu\mathbf{S}^2 + \Gamma - \rho\Lambda, \tag{9.3}$$

where Γ and Λ are heating and cooling functions.

The Pencil Code is set up in terms of "modules", which can be easily added and removed: the addition of modules can add new equations to be solved, and also add new terms to the existing equations. For our problem, the basic modules are sufficient.

9.3 Model

Our problem can almost be modelled with a simple convective slab with gravity. However, for a nonlinear model, we can no longer simply input the shear velocity as a coefficient. We need to make a slight modification to our equation of motion:

$$\frac{Du}{Dt} = -c_s^2\left(\nabla\frac{s}{c_p} + \nabla\ln\rho\right) - \nabla\Phi + f + \frac{1}{\rho}\nabla\cdot(2\nu\rho\mathbf{S})\boxed{-\tfrac{1}{\tau}\left(u - u_{ref}\right)}. \tag{9.4}$$

The added term provides a force that will act to produce a velocity gradient specified by u_{ref}. τ is the timescale on which it acts. It must be chosen so that the shear gradient will build up slowly, to avoid interference with the oscillations we hope to observe. The force term has no physical meaning; it is only a mathematical condition we have imposed in order to specify the shear profile. This allows us to observe the effects of different shear gradients without being forced to adjust the other parameters.

The initial density is specified by a polytropic model. We chose the length scale of our variables by setting the height of the computational domain to correspond to the size of supergranules. The only parameters are then chosen to approximate the solar model. In order to observe the dependence of the phase speed on wavenumber, we begin with the velocity displaying convective rolls, the number of which (and thus the horizontal wavenumber) can be specified. We consider horizontal wavenumbers corresponding to one, two, three and four convective rolls. Under our scaling, these produce wavenumbers kR in the range of supergranulation. We measure the speed of the waves resulting from running the model at each of these wavenumbers and at various magnitudes of shear velocity.

9.4 Results

The nonlinear simulation was run for a number of shear velocities of the form $U_x(z) = U_0\left[1 + \cos(k_z(z - z_0))\right]$. The choice of vertical wavenumber, k_z, specifies the number of rolls in our layer. We choose to consider a single roll in depth. The layer is three times as wide as it is deep, so we consider horizontal wavenumbers corresponding to one, two, three or four rolls.

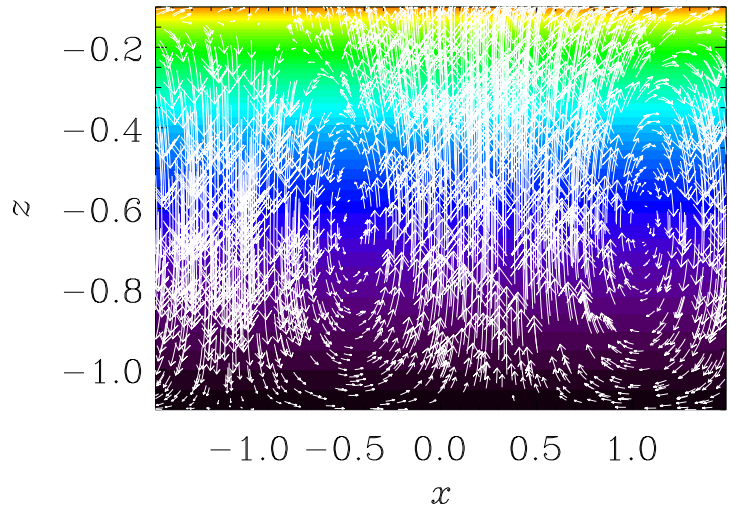

Figure 9.1: Initial velocity and entropy as functions of x and z for a horizontal wavenumber corresponding to one roll.

In each case, the velocity vectors in the two-dimensional layer can be plotted at any point in time. Initially, the number of convective cells corresponding to the horizontal wave number can be observed, as shown in Figures 9.1–9.4. As time progresses, the convective cells change shape. For lower wavenumbers, they disappear and reform. After a number of such cycles, they disappear altogether and are replaced by higher-wavenumber modes. At higher wavenumbers, the modes vary in shape over time, but they persist for the entire length of the simulation. In both cases, we measure the speed of the initial modes, as these are at the wavenumbers that interest us.

To determine the phase speed of these modes, we consider a slice at the surface of the layer. In this slice, the entropy can be plotted as a function of x and times, as shown in Figures 9.5–9.8. Plotting velocity in the layer at a series of times revealed that for wavenumbers corresponding to fewer than four modes, the rolls eventually disappeared. The plots of entropy at the top of the layer are consistent with these results. For one mode, the cells deform, disappearing and reappearing, before disintegrating permanently. Wavenumbers corresponding to two and three modes produce initial strong modes that grow weaker before disappearing altogether. For four or more initial rolls, the modes undergo deformations in time, but both the number and the strength of the modes remain constant.

In all cases, these entropy plots allow the speed of the travelling waves to be measured. The density stratification can be extracted from the model and used as coefficients for the linear model, and thus the phase speeds for the linear and nonlinear models can be compared directly. This comparison, for different values of U_0 and horizontal wavenumber, is in Table

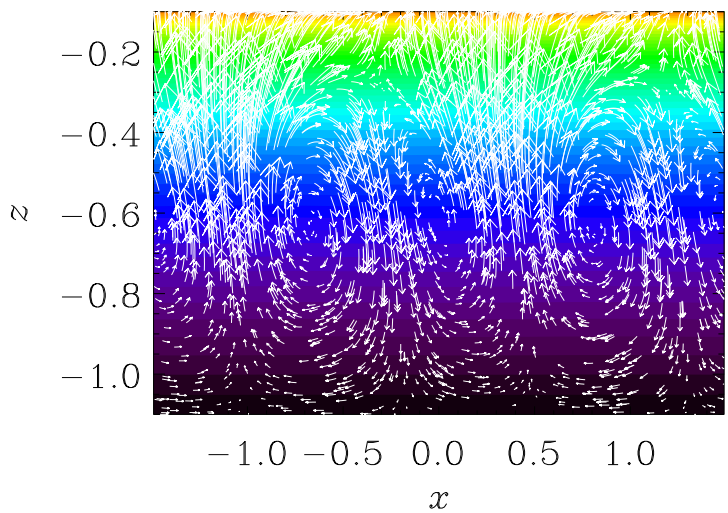

Figure 9.2: Initial velocity and entropy as functions of x and z for a horizontal wavenumber corresponding to two rolls.

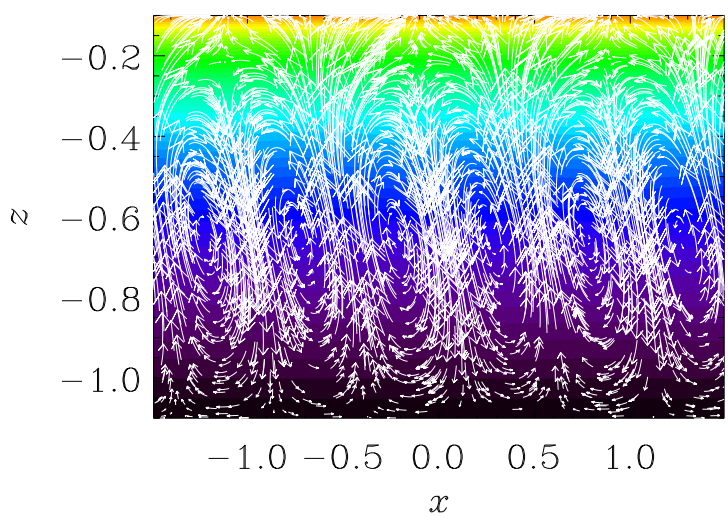

Figure 9.3: Initial velocity and entropy as functions of x and z for a horizontal wavenumber corresponding to three rolls.

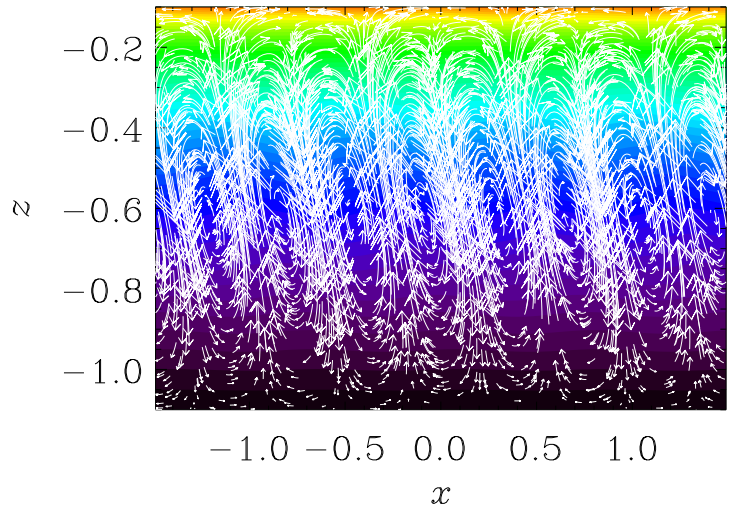

Figure 9.4: Initial velocity and entropy as functions of x and z for a horizontal wavenumber corresponding to four rolls.

9.1.

For all input shear velocities, the nonlinear model produced travelling waves. Though they seem to travel slower than the shear, this is not actually the case: the phase speed is measured at the surface of the layer, where the shear velocity is zero. These phase speeds are of the same order as those produced by the linear model, for the same stratification; however, the nonlinear phase speed is always larger than the linear speed. This suggests that nonlinear effects may contribute to the observed wavelike behaviour of supergranulation.

9.5 Conclusions

The previous models demonstrated that a shear gradient can produce the observed wavelike behaviour of supergranulation; however, they did not account for any nonlinear effects. To investigate these effects, we consider a nonlinear model including a shear gradient. The behaviour in time of the initial convective rolls in this model depends on their wavenumber. For lower wavenumbers, the modes eventually disappear. The modes with wavenumbers at the high end of the range corresponding to supergranulation persist for the duration of the simulation.

During the period in which the convective modes persist, they travel faster than the surface velocity. These nonlinear modes are also faster than those produced by the linear model for the same stratification and shear velocity. Despite the fact that not all wavenumbers produce lasting convective modes, these results suggest that the nonlinear effects provide a

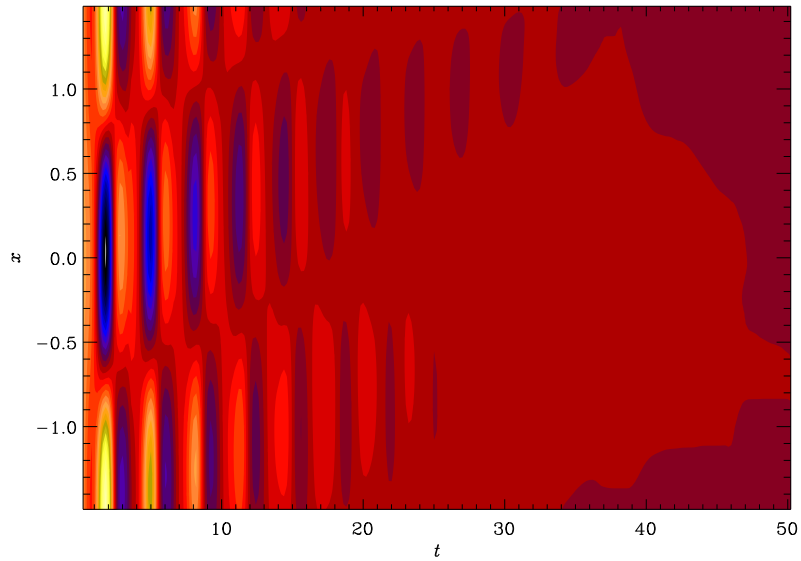

Figure 9.5: Density as a function of x and time, in a slice at the top of the layer, for a horizontal wavenumber corresponding to one roll.

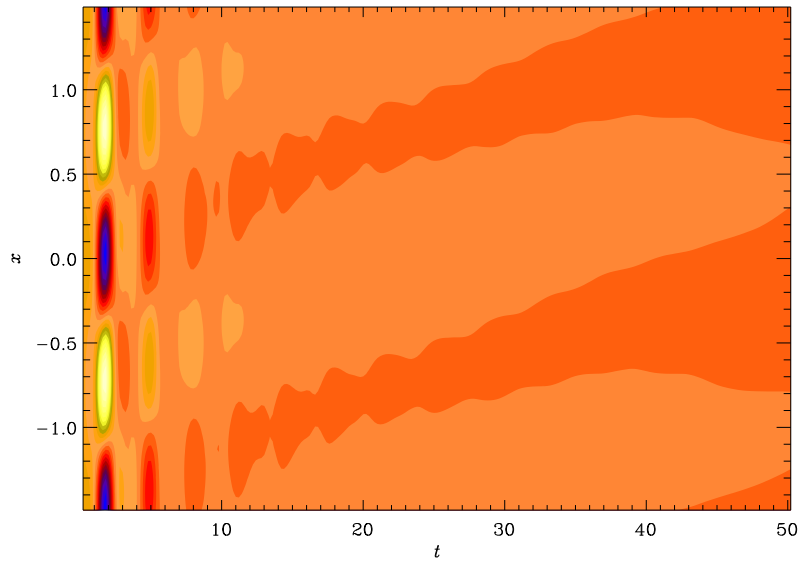

Figure 9.6: Density as a function of x and time, in a slice at the top of the layer, for a horizontal wavenumber corresponding to two rolls.

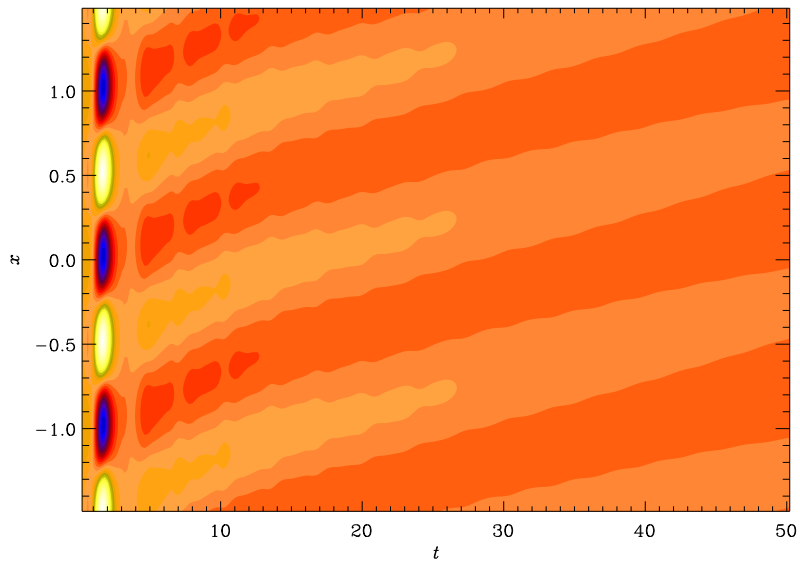

Figure 9.7: Density as a function of x and time, in a slice at the top of the layer, for a horizontal wavenumber corresponding to three rolls.

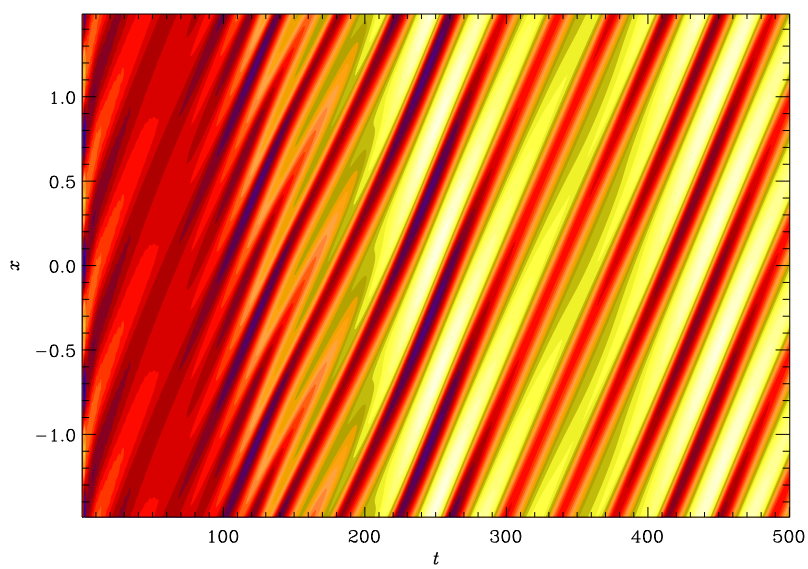

Figure 9.8: Density as a function of x and time, in a slice at the top of the layer, for a horizontal wavenumber corresponding to four rolls.

Table 9.1: Phase speeds obtained from the nonlinear model for different shear velocities and horizontal wavenumbers, compared to those from the linear model.

U_0	$\frac{K_x L_x}{2\pi}$	Nonlinear Phase Speed	Linear Phase Speed
0.05	1	0.04	0.0302
	2	0.03	0.0243
	3	0.023	0.0172
	4	0.0197	0.0127
0.02	1	0.0123	0.0059
	2	0.0114	0.0048
	3	0.0103	0.0037
	4	0.0135	0.0058
0.1	1	0.06	0.0481
	2	0.058	0.0344
	3	0.035	0.0252
	4	0.028	0.0200

not insubstantial contribution to the speed of supergranular waves.

Chapter 10

Conclusions

The goal of this work was to explain observations from Gizon, Duvall and Schou (2003) that solar supergranulation demonstrates wave-like behaviour, with a non-advective phase speed of ~ 65 m/s. The explanation for this has been the subject of some debate. Busse (2004) suggests that the Coriolis force could produce wave-like behaviour of convective cells in rotation fluids. Rast *et al.* (2004) question the result altogether, claiming that, rather than waves, the observed spectrum could be consistent with two components of non-oscillatory bulk motions having different rotation rates and being somewhat asymmetrically distributed in space. Our proposed explanation is that the steep shear gradient at the surface of the Sun causes unstable convective modes to become running waves, and that these modes form the supergranular waves.

We initially consider a linearized nonviscous compressible hydrodynamic model. This model reproduces the observed wave-like behaviour; however, in the range of wavenumbers corresponding to supergranulation, it produces a maximum phase speed of ~ 26 m/s above the surface speed. While this qualitatively supports our proposed explanation, this speed is substantially smaller than the observed phase speed. The convective modes obtained in this case are constrained very near the surface when compared to the corresponding polytropic model. The major difference between the two models is the Brunt-Väisälä frequency: the profile obtained from helioseismology drops abruptly at the surface and then immediately shoots upward. For the polytrope, the Brunt-Väisälä frequency also drops near the surface, but not as much, and there is no sudden increase. The top boundary had to be carefully chosen, as the sharp increase in Brunt-Väisälä frequency trapped modes at the surface. These shallow modes were of the scale of granulation rather than supergranulation. This evident sensitivity to the Brunt-Väisälä frequency could be the reason the modelled phase speeds are lower than observations. This behaviour might dominate because of the simplications made in our model. Thus, we consider less simplified models, to check for the contributions of other factors.

Proceeding to consider the effects of viscosity and a toroidal magnetic field, in conjunction with the shear gradient, we find that either of these can reproduce the observations, for a reasonable choice of parameters. An approximation based on mixing-length theory suggests that the necessary viscosity is attained in the Sun. The necessary magnetic field occurs in sunspots, but it is a bit high for the quiet Sun. In both cases, the observed phase speed occurs only at higher order modes. A linear model including both viscosity and magnetic field also reproduces the observed phase speed, and the order of the modes at which it occurs is reduced. Even so, it seems more likely that we are observing modes of lower orders than those that reproduce the observed phase speed, so we also consider a nonlinear model. In this case, we find that a nonlinear version of our original model produces higher phase speeds for the same parameters. Thus, we conclude that nonlinear effects may also have a role in producing the observed phase speeds.

We also consider the alternative explanation for the observations: the Coriolis force. Data produced by a nonlinear model by Miesch *et al.* shows no evidence of supergranular waves. Due to the limitations of the simulation data, we also consider a linear model including the Coriolis force. For the solar rotation rate, the addition of the Coriolis force causes only a very small increase in the phase speeds obtained by the original model. A model including the Coriolis force and no shear gradient does produce wave-like behaviour; however, their phase speeds are very low. Thus, we find no evidence that the Coriolis force makes a significant contribution to the observed supergranular waves.

We conclude that there is strong evidence that the observed wave-like behaviour of supergranulation is caused by the steep shear gradient at the solar surface.

Bibliography

[1] J. A. Adam. Hydrodynamic instability of convectively unstable atmospheres in shear flow. *Astrophysics and Space Science*, 50:493–514, 1977.

[2] H. M. Antia, S. M. Chitre, and S. K. Pandey. Granulation and supergranulation as convective modes in the solar envelope. *Solar Physics*, 70:67–91, Mar. 1981.

[3] A. Brandenburg. *Computational aspects of astrophysical MHD and turbulence*, page 269. Advances in Nonlinear Dynamics, 2003.

[4] A. Brandenburg. Near-surface shear layer dynamics. In F. Kupka, I. Roxburgh, and K. Chan, editors, *IAU Symposium*, volume 239, pages 457–466, May 2007.

[5] F. H. Busse. On thermal convection in slowly rotating systems. *Chaos*, 14(3):803–808, 2004.

[6] J. Christensen-Dalsgaard. Lecture Notes on Stellar Oscillations.

[7] P. Giles. *Time-Distance Measurements of Large-Scale Flows in the Solar Convection Zone*. PhD thesis, Stanford University, 1999.

[8] L. Gizon, T. L. Duvall, and J. Schou. Wave-like properties of solar supergranulation. *Nature*, 421:43–44, 2003.

[9] C. A. Green and A. G. Kosovichev. Traveling convective modes in the Sun's subsurface shear layer. *Astrophysical Journal*, 641:L77–L80, Apr. 2006.

[10] C. A. Green and A. G. Kosovichev. Magnetic effect on wave-like properties of solar supergranulation. *Astrophysical Journal*, 665:L75–L78, Aug. 2007.

[11] C. A. Green, A. G. Kosovichev, and M. S. Miesch. Effect of the subsurface shear layer on solar supergranulation. In *Proceedings of SOHO 18/GONG 2006/HELAS I, Beyond the spherical Sun*, volume 624 of *ESA Special Publication*, Oct. 2006.

[12] M. S. Miesch, A. S. Brun, and J. Toomre. Solar differential rotation influenced by latitudinal entropy variations in the tachocline. *Astrophysical Journal*, 641:618–625, Apr. 2006.

[13] M. S. Miesch, J. R. Elliott, J. Toomre, T. L. Clune, G. A. Glatzmaier, and P. A. Gilman. Three-dimensional spherical simulations of solar convection. I. Differential rotation and pattern evolution achieved with laminar and turbulent states. *Astrophysical Journal*, 532:593–615, Mar. 2000.

[14] M. Stix. *The Sun: An Introduction*. Springer, 1989.

[15] S. M. Tobias and D. W. Hughes. On the instability of magnetohydrodynamic shear flows. *Proceedings of the Royal Society of London A*, 457:1365–1384, 2001.

[16] S. M. Tobias and D. W. Hughes. The influence of velocity shear on magnetic buoyancy instability in the solar tachocline. *Astrophysical Journal*, 603:785–802, Mar. 2004.